Electromagnetic control of oscillating flows in a cavity

Electromagnetic control of oscillating flows in a cavity

PROEFSCHRIFT

ter verkrijging van de graad van doctor
aan de Technische Universiteit Delft,
op gezag van de Rector Magnificus prof. ir. K.C.A.M. Luyben,
voorzitter van het College voor Promoties,
in het openbaar te verdedigen op vrijdag 16 januari 2015 om 10 uur
door

Rudi KALTER

natuurkundig ingenieur
geboren te Kampen.

Dit proefschrift is goedgekeurd door de promotor:

Prof. dr. ir. C. R. Kleijn

Copromotor: Dr. ir. M. J. Tummers

Samenstelling promotiecommissie:

Rector Magnificus	voorzitter
Prof. dr. ir. C. R. Kleijn	Technische Universiteit Delft, promotor
Dr. ir. M. J. Tummers	Technische Universiteit Delft, copromotor
Prof. dr. F. Scarano	Technische Universiteit Delft
Prof. dr. ir. A. A. van Steenhoven	Technische Universiteit Eindhoven
Prof. dr. A. Thess	Universität Stuttgart
Ir. D. van der Plas	Tata Steel IJmuiden
Prof. dr. R. F. Mudde	Technische Universiteit Delft

This work was supported by the Dutch Technology Foundation STW, Tata Steel and ABB.

printed by: GVO drukkers & vormgevers B.V.

ISBN: 978-90-6464-837-3

Author email: rudikalter@gmail.com

Summary

In continuous steel casting, liquid steel flows turbulently through a submerged nozzle into a thin, vertical mould. In the mould the liquid steel is cooled, such that it solidifies and plate steel is formed. On top of the liquid steel in the mould, a slag layer is present and due to the turbulent behavior of the flow, particles and droplets from the slag layer can get entrained into the bulk flow. This leads to inclusions in the final product, which is unwanted. The flow in the mould needs to be stabilized, such that entrainment effects no longer play a role. For this, electromagnets are generally installed next to the mould. The flow of the electrically conductive liquid steel through the magnetic field induces an electrical current, from which an induced Lorentz force emerges, which acts as a so-called electromagnetic brake.

This dissertation presents an experimental study on flow dynamics, heat transfer, and electromagnetic interaction in a thin slab continuous casting mould. To mimic the continuous casting process, a glass model of the mould was fabricated and (salt) water was used as modeling fluid, such that particle image velocimetry measurements could be performed.

The flow of both single and bifurcated jets is studied. The jets issuing into the thin cavity and the induced flow in the cavity exhibit a self-sustained oscillating behavior with a frequency that grows linearly with the jet velocity. It was found that the self-sustained oscillations exist due to an imbalance between the inertial forces in the recirculation zones alongside the jets and the pressure force due to a low pressure zone in these recirculation zones. The low pressure zone in the center of the recirculation zones can exist due to the (semi) two dimensionality of the flow. When a thicker cavity is employed, the self-sustained jet oscillations vanish due to a less structured, and more three dimensional, flow pattern.

Next, the influence of the self sustained jet oscillations on heat transfer at the wall is studied for flow from a bifurcated nozzle. A constant high inlet flow temperature is applied, in combination with cooling of one of the broad walls. Measurements of the temperature at the cooled wall are performed

using thermochromic liquid crystals (TLC's) attached to the cooled wall. The self-sustained jet oscillations show an imprint on the TLC's. At the point where the shear layers of the jet reach the wall a hot spot is formed, and in the center of the recirculation zone alongside the jet a cold spot is found. The cold spot moves with the jet oscillation, leading to a non-uniform and time-dependent temperature distribution at the cooled wall. Measurements of the temperature drop of the liquid over the cavity have been performed and the average heat transfer coefficient h was found to scale as $h \propto \mathrm{Re}^{0.8}$.

Subsequently, the self-sustained jet oscillations are influenced by means of an applied electromagnetic force. This is done by applying an electrical current through a saline solution across the width of the cavity, in conjunction with a permanent magnetic field perpendicular to the electrical current. The combination of the electrical and magnetic field with a liquid with high electrical conductivity (as compared to tap water) leads to a permanent and local Lorentz force. This Lorentz force can be applied such that the jet oscillations are either suppressed or enhanced. In the oscillation suppressing configuration, the flow due to the Lorentz force prohibits the recirculation zones from forming, and so no low pressure zones emerge alongside the jet. Above a critical forcing strength, this suppresses the self-sustained jet oscillations completely. In the opposite, oscillation enhancing, configuration, the flow due to the Lorentz force increases the formation of the recirculation zones and hence the oscillation frequency increases.

We finalize this thesis by discussing how the experimental results from this work can be used in the design and optimization of actual steel casters, and in the validation of numerical models to be used for that same purpose. Shortcomings of the experimental methods are discussed, as well as the appropriate scaling of physical parameters.

Samenvatting

Tijdens het continu gieten van staal stroomt vloeibaar staal door een ondergedompelde uitstroommond in een dunne verticale gietvorm. In de gietvorm wordt het vloeibare staal gekoeld zodat het stolt, hierbij wordt een stolhuid gevormd. Bovenop het vloeibare staal in de mal is een slaklaag aanwezig en vanwege het turbulente gedrag van de stroming kunnen deeltjes en druppels vanuit de slaklaag in de bulkstroming worden ingevangen. Dit leidt tot ongewenste inclusies in het uiteindelijke product. De stroming in de mal dient gestabiliseerd te worden zodat inclusie-effecten niet langer een rol spelen. Om de stroming te stabiliseren worden doorgaans elektromagneten geïnstalleerd naast de mal. De stroming van het elektrisch geleidende staal door het magneetveld induceert een elektrische stroom, die op zijn beurt weer een Lorentzkracht induceert. Deze Lorentzkracht fungeert als een elecromagnetische rem.

Dit proefschrift presenteert een experimentele studie naar de vloeistofdynamica, warmte-overdracht en elektromagnetische interactie in een gietvorm van een dungietmachine voor staal. Om het continue staalgietproces na te bootsen is een glazen model van de mal vervaardigd en is (zout) water gebruikt als een modelvloeistof. In dit model kunnen particle image velocimetry metingen worden uitgevoerd.

De stromingen van zowel een enkele als een vertakte jet zijn bestudeerd. De instromende jet en de daardoor opgewekte stroming in de mal vertonen een zichzelf instandhoudend oscillerend gedrag met een frequentie die lineair toeneemt met de instroomsnelheid. De zichzelf instandhoudende oscillaties bestaan vanwege een onbalans tussen de traagheidskrachten in de recirculatiezones langs de jet en de drukkracht vanwege een lagedrukgebied in deze recirculatie zones. Het lagedrukgebied in het centrum van de recirculatiezones kan bestaan vanwege het (semi)tweedimensionale gedrag van de stroming. Wanneer een dikkere mal wordt gebruikt verdwijnen de zichzelf instandhoudende jetoscillaties vanwege een minder gestructureerd en meer driedimensionaal stromingspatroon.

Vervolgens is de invloed van de zichzelf instandhoudende jetoscillaties op de warmte-overdracht aan de wand bestudeerd voor de stroming vanuit een gesplitste uitstroommond. Een constante hoge instroomtemperatuur is opgelegd in combinatie met een koeling van één van de brede wanden. Metingen van de temperatuur aan de gekoelde wand zijn uitgevoerd gebruikmakend van thermochrome vloeibare kristallen (TLC's) die op de gekoelde wand zijn aangebracht. De zichzelf onderhoudende oscillaties vertonen een thermische afdruk op de TLC's. Op het punt waar de randen van de jet de gekoelde wand bereiken vormt zich een gebied met een hoge temperatuur en in het centrum van de recirculatiezone langs de jet is een gebied met lage temperatuur aanwezig. De koude plek beweegt met de jetoscillatie wat leidt tot een niet-uniforme en tijdsafhankelijke temperatuurverdeling aan de gekoelde wand. Metingen van de temperatuurval van de vloeistof in de mal zijn uitgevoerd en de warmteoverdrachtscoefficient h schaalt als $h \propto \mathrm{Re}^{0.8}$.

De zichzelf onderhoudende jet oscillaties worden beïnvloed door een elektromagnetische kracht. Dit wordt gedaan door een elektrische stroom the laten lopen, in combinatie met een permanent magnetisch veld loodrecht op de elektrische stroom. De elektrische stroom loopt over de wijdte van de mal door een zoutoplossing. De combinatie van het elektrische en het magnetische veld in een vloeistof met een hoge elektrische geleidbaarheid (vergeleken met kraanwater) leidt tot een permanente, lokale Lorentzkracht. Deze Lorentzkracht kan worden gebruikt om de jetoscillaties ofwel te onderdrukken, ofwel te versterken. In de oscillatie-onderdrukkende configuratie verhindert de Lorentzkracht de vorming van de recirculatiezones, zodat er geen lagedrukgebied ontstaat langs de zijkant van de jet. Boven een kritische sterkte van de forcering worden de jetoscillaties volledig onderdrukt. In de tegengestelde, oscillatieversterkende, configuratie, versnelt de Lorentzkracht de vorming van de recirculatiezones, waardoor de oscillatie frequentie toeneemt.

Dit proefschrift wordt afgesloten met een discussie over hoe de experimentele resultaten kunnen worden gebruikt voor het ontwerpen en optimaliseren van daadwerkelijke staalgieters en voor het valideren van numerieke modellen voor hetzelfde doel. Tekortkomingen van de experimentele resultaten worden beschouwd alsmede een passende schaling van fysische parameters.

List of symbols

Roman Symbols

Symbol	Description	Units
a_n	Time coefficients of the POD	[-]
a_1	First time coefficient of the POD	[-]
a_2	Second time coefficient of the POD	[-]
A	Mean wave amplitude	[m]
A	Surface area	[m^2]
b	Blue value	[-]
$\mathbf{B}$	Magnetic field field strength	[T]
B_{ref}	Reference magnetic field strength	[T]
B_z	z-component of magnetic field	[T]
c_p	Heat capacity	[J/kgK]
d	Nozzle hydraulic diameter	[m]
d_c	Critical nozzle depth	[m]
d_{gap}	Distance between stainless steel plates	[m]
d_n	Nozzle depth	[m]
d_{LC}	Liquid crystal sheet thickness	[m]
d_{ss}	Stainless steel thickness	[m]
D	Distance between magnets	[m]
$\mathbf{E}$	Electrical field strength	[V/m]
E_{ref}	Reference electrical field strength	[V/m]
f	Frequency	[Hz]
f_{POD}	Frequency determind from POD	[Hz]
f_{TS}	Frequency determind from time series	[Hz]
$f^{\#}$	f-stop number	[-]
$\mathbf{F}_L$	Lorentz force	[N]
g	Gravitational acceleration	[m/s^2]
g	Green value	[-]
h	Water level height	[m]
h	Heat transfer coefficient	[W/m^2K]
h_{conv}	Convective heat transfer coefficient	[W/m^2K]

h_{cool}	Heat transfer coefficient of cooling water to steel	[W/m^{2}K]
h_{LC}	Heat transfer coefficient of the LC sheets	[W/m^{2}K]
h_{ss}	Heat transfer coefficient of stainless steel	[W/m^{2}K]
H	Height of the cavity	[m]
H	Hue value	[°]
I	Electrical current	[A]
$\mathbf{j}$	Electrical current density	[A/m^2]
k	Turbulence kinetic energy	[m^2/s^2]
k_{osc}	Kinetic energy related to slow oscillation	[m^2/s^2]
k_{turb}	Turbulence kinetic energy	[m^2/s^2]
L	Nozzle to magnet distance	[m]
n	Mode number of the POD	[-]
N	Number of modes of the POD	[-]
p	Pressure	[N/m^2]
r	Radial coordinate	[m]
r	Red value	[-]
R_c	Radial recirculation zone center position	[m]
t	Time	[s]
T	Thickness of the cavity	[m]
T	Temperature	[°C]
T_{in}	Inlet temperature	[°C]
T_{out}	Outlet temperature	[°C]
T_W	Cooling wall temperature	[°C]
$\mathbf{u}$	Velocity	[m/s]
u_x	Horizontal component of the velocity	[m/s]
u_y	Vertical component of the velocity	[m/s]
$\bar{u_i}$	Mean velocity	[m/s]
u_i'	Fluctuating component of the velocity	[m/s]
$\tilde{u_i}$	Long term oscillation component of the velocity	[m/s]
v_{in}	Inlet velocity	[m/s]
v_{max}	Maximum induced velocity	[m/s]
w	Tangential velocity	[m/s]
W	Width of the cavity	[m]
x	Horizontal coordinate parallel to front wall	[m]
x_c	x-coordinate of the recirculation zone center	[m]
y	Horizontal coordinate perpendicular to front wall	[m]
y_c	y-coordinate of the recirculation zone center	[m]
z	Vertical coordinate parallel to front wall	[m]

Greek Symbols

Symbol	Description	Units
ΔT	Temperature difference	[°C]
$\Delta\phi$	Potential difference	[V]
η	Free surface elevation	[m]
θ	Jet angle	[°]
λ	Wave length	[m]
λ_{LC}	Thermal conductivity of LC sheets	[W/mK]
λ_{ss}	Thermal conductivity of stainless steel	[W/mK]
λ_{water}	Thermal conductivity of water	[W/mK]
ϕ_1	Electrical potential	[V]
ϕ_2	Electrical potential	[V]
ϕ_n	Base functions of the POD	[m/s]
ϕ_v	Flow rate	[m^3/s]
ν	Kinematic viscosity	[m^2/s]
ρ	Density	[kg/m^3]
σ	Electrical conductivity	[S/m]

Abbreviations

Abbreviation	Description
CCD	Charged coupled device
CFD	Computational fluid dynamics
CIFT	Contactless induced flow tomography
CMOS	Complementary metal oxide semiconductor
EMHD	Electro-magneto hydrodynamics
LCT	Liquid crystal thermography
LDA	Laser Doppler anemometry
LED	Light emitting diode
MHD	Magneto hydrodynamics
PIV	Particle image velocimetry
PTV	Particle tracking velocimetry
POD	Proper orthogonal decomposition
TLC	Thermochromic liquid crystal
UDV	Ultrasonic Doppler velocimetry

Dimensionless groups

Symbol	Description
Re	Reynolds number
N	Stuart number
N_c	Critical Stuart number
Nu	Nusselt number
Pr	Prandtl number
St	Strouhal number

Contents

Chapter 1

Introduction

1.1 Background of the investigation

1.1.1 Development of the continuous casting process

Continuous casting of liquid metals with a low melting temperature was successfully put into business in 1843 (Laing, US patent number 3023). Since then, lots of effort have been put into adjusting the casting process for the casting of metals with a high melting temperature, such as steel. A breakthrough in the steel casting world was the invention of the oscillating mould in the 1940's. The oscillation of the mould prevented sticking of the solidifying steel to the mould, reducing the breakout frequency (outflow of molten steel through a rupture in the solidified shell). In 1950, the first commercial continuous steel caster was put into operation, by Mannesmann in West-Germany.

The first continuous steel casters were of the vertical type, and were used for blooms and billets of small sections. This resulted in a low production rate since the steel had to solidify completely in the mould. In 1963 the circular-arc-type or Model S machine was introduced, which has a vertical section, followed by a bend and an extensive horizontal section. With this circular-arc-type machine, larger sections could be produced, reducing the production costs (Mizoguchi et al. 1981).

Figure 1.1a illustrates the continuous casting process in the circular-arc-type machine. Liquid steel is poured from a ladle into a tundish from which it flows into the mould (illustrated schematically in figure 1.1b). The flow from the tundish into the mould is through a submerged entry nozzle. Cooling is applied in the mould, such that the steel solidifies and

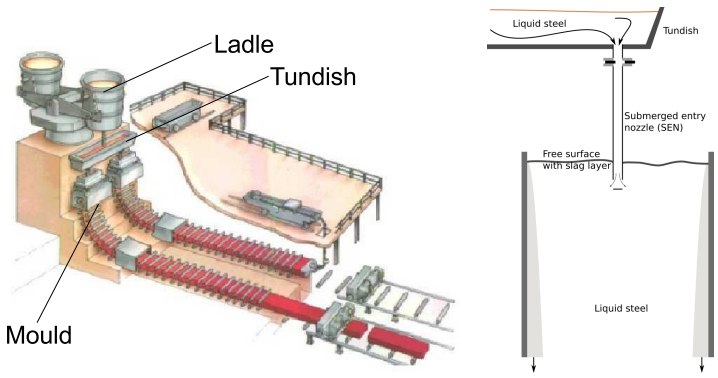

Figure 1.1: Schematics of the continuous steel casting process. **a** Liquid steel is poured from a ladle into a tundish. From the tundish the liquid steel flows into two moulds where it is cooled. The solidified steel enters a bend, redirecting the motion of the steel slab from vertical to horizontal. Further down stream the solidified steel is cut to be processed further. **b** Schematics of the tundish and the mould. Liquid steel flows from the tundish into the mould with a continuous head pressure and the flow rate is regulated using a slide gate. The steel is injected into the mould through a submerged entry nozzle. At the walls the steel solidifies due to cooling from the wall. On top of the liquid steel, a slag layer is present to insulate the steel and to prevent oxidation.

a strand of solidified steel is formed at the walls. Lower in the caster, the solidified steel enters a bend, switching its direction of motion from vertical to horizontal. The steel is cooled until the strand is fully solidified. At the end of the caster the strand is cut into slabs that are subsequently hot and cold rolled to produce coils with a sheet thickness between 0.1 and 3 mm. At the top of the mould, the liquid steel is covered with a slag layer for thermal insulation, and to prevent oxidation.

In the past decades, a shift in steel production from western countries to low-wage countries like China and India is observed. In order to stay competitive, the steel producing companies in western countries have to increase the production rate and steel quality, while reducing the costs. To reduce post-processing costs, the emphasis in continuous steel casting has shifted from the casting of thick slabs with a thickness of 20 to 25 cm to thinner slabs with a thickness of 5 to 10 cm. The slabs have a width of approximately 1.5 m. The process of thin slab casting exhibits flow instabilities in the mould, which can lead to a decrease in the quality of the final product. To maintain the same production rate and steel quality as before, flow stabilizing measures have to be incorporated. Investigation of these stabilizing measures is a

costly process, but it is necessary for a strong competitive position of the steel producing companies in western countries.

1.1.2 Experimental investigation of the continuous casting process

To investigate the flow dynamics in continuous casting, researchers would like to perform measurements using liquid metals, to mimic the steel properties as closely as possible. However, flows of liquid metals are hard to study for several reasons. First of all, liquid metal is opaque, this means that no optical measurement techniques can be used to visualize the inner flow structures. Furthermore, liquid metals usually have a high melting temperature and fumes from low melting temperature metals may be toxic, such that extensive safety measures are needed when working with these metals. Possible experimental techniques to study flow dynamics in liquid metals are ultrasonic Doppler velocimetry (UDV, e.g. Timmel et al. (2010)) and contactless inductive flow tomography (CIFT, e.g. Stefani et al. (2004)), but these techniques are less well developed as compared to optical flow measurement techniques such as particle image velocimetry (PIV, e.g. Adrian and Westerweel (2011)) and laser Doppler anemometry (LDA, e.g. Durst et al. (1976)).

To overcome the difficulties of using liquid metal, many experimental studies to investigate the fluid flow pattern in the mould have been performed using water as a working fluid (e.g. Gupta et al. (1997), Gupta and Lahiri (1994), Honeyands and Herbertson (1995), Szekely and Yadoya (1972), Torres-Alonso et al. (2010a;b), Yuan et al. (2004)). The experiments are usually performed in (plexi)glass models of the casting mould. In these studies, simplifications compared to the actual casting process are unavoidable, neglecting for instance the solidifying steel strand, and the slag layer on top of the liquid steel and by using simplified nozzle designs. This means that the focus is on the flow dynamics only, not addressing heat transfer and solidification.

The use of water models for predictions of the flow dynamics in the actual casting process is under debate. According to Chaudhary et al. (2009), Reynolds and Froude number similarity can be reached only when a near full scale model of the mould is employed. This is due to the fact that the kinematic viscosities of liquid steel and water are more or less equal. When the flow is fully turbulent, however, the influence of the Reynolds number is small and a smaller scale model can be employed (Gupta and Lahiri (1996)).

For a balance of inertia and surface tension forces, also Weber similarity is required. A combined Froude and Weber similarity is achieved for a 0.6:1

scaled model Zhang et al. (2007). However, the phenomena involving surface tension for a slag layer on top of a liquid steel bath are very complex and can not properly be incorporated in a simple water model, thus it is likely not helpful to take Weber similarity into account without matching many other physical phenomena as well Chaudhary et al. (2009).

The main difference in thermal properties of water compared to liquid steel is captured in the Prandtl number. For water at 20°C $Pr \approx 7$, while for liquid steel $Pr \approx 0.1$, which means that thermal diffusivity plays a much larger role in liquid steel, as compared to water.

1.1.3 Self sustained oscillations

When a jet flows into a thin cavity, such as in thin slab casting, self-sustained jet oscillations are known to occur due to a hydrodynamic feedback mechanism (Maurel et al. 1996). In general, self-sustained oscillations are known to occur when a shear layer is bounded by recirculation zones that are present in confined geometries (Rockwell 1983, Rockwell and Naudascher 1979). The self-sustained oscillation of a single jet issuing into a thin cavity has been studied extensively (e.g. Lawson and Davidson (2001), Mataoui and Schiestel (2009), Maurel et al. (1996), Molloy and Taylor (1969), Villermaux and Hopfinger (1994)).

In continuous casting the liquid steel flows into the mould through a submerged bifurcated nozzle. From the nozzle, two jets issue more or less horizontally in opposite directions towards the narrow side walls of the cavity (see figure 1.1b). This configuration has been studied by amongst others Honeyands and Herbertson (1995), Lawson and Davidson (2002) and Torres-Alonso et al. (2010b). These studies reported that self-sustained jet oscillations are also present in the flow from a bifurcated nozzle into a thin slab casting mould.

The observed self-sustained jet oscillations are of a low frequency (as compared to gravity waves that may occur in this geometry (Honeyands and Herbertson (1995))), but they contain a significant amount of kinetic energy, such that they can have a significant impact on the dynamics of the steel/slag interface. The interaction of the self-sustained oscillating structures with the steel/slag interface leads to the inclusion of slag particles and droplets into the bulk steel flow. Most of these particles and bubbles float back to the steel/slag interface, but some may get entrapped in the steel layer and cause a decrease in the steel quality.

Improved understanding of the self-sustained oscillations may lead to strategies to prevent these oscillations, and hence this may lead to an increased production rate and steel quality.

1.1.4 Heat transfer

A physical mechanism which is strongly coupled to the flow dynamics in the mould, is heat transfer. The walls of the mould are cooled, such that a solidified strand of steel forms near the wall. To study heat transfer in the mould, numerical models have been developed (e.g. Zhao et al. (2005)), but these need to be validated using measurement results, which can be extracted from plant measurements (e.g. Mahmoudi (2006), Wang et al. (2012)). These measurements can be performed using thermocouples in the cooling wall in the mould, but they are usually difficult to perform and open to interpretation.

Temperature measurements in transparent liquids on the other hand, can be performed using thermochromic liquid crystals (TLC's, e.g. Dabiri (2009)), which have the property that the colour of the TLC's change when the temperature changes. The colour of the TLC's gives an indication of the heat transfer towards the wall, and by using the TLC's accurate measurement results of the temperature near the cooled wall, numerical models can be validated.

1.1.5 Electromagnetic braking

Nowadays, strong external magnets are widely used to stabilize the flow in the casting mould, based on the principles of magnetohydrodynamics (MHD, e.g. Davidson (2001)). When a liquid with a high electrical conductivity, like liquid steel, flows through a magnetic field, induced electrical currents cause a Lorentz force according to the magnetic force, $\mathbf{F}_M = \sigma \mathbf{u} \times \mathbf{B} \times \mathbf{B}$, where σ is the electrical conductivity of the liquid metal, $\mathbf{u}$ is the local flow velocity, and $\mathbf{B}$ is the magnetic field strength. The magnetic force acts only in the vicinity of the magnetic field and is directed opposite to the local flow direction. Thus, the magnetic field acts like an obstacle in the flow, altering the flow pattern without actual intrusion of the flow with a physical obstacle.

The application of magnets to alter the flow pattern in the mould is referred to as electromagnetic braking. The electromagnetic brake has been studied both experimentally in casting mould models using liquid metal as a working fluid (e.g. Timmel et al. (2010)) and numerically (e.g. Garcia-Hernandez et al. (2010), Haiqi et al. (2008)).

The application of electromagnetic braking in water models is not as straightforward as in liquid metal models, due to the relatively low electrical conductivity of the water. To introduce electromagnetic forcing in liquids with low electrical conductivity (for instance salt water), a combination of a magnetic field with an imposed electrical field can be employed. This concept is used in several flow situations, for instance to increase laminar mixing (Rossi et al. 2012a;b) and to increase heat transfer (Kenjereš 2008, Kenjereš

et al. 2009). Now, the acting Lorentz force is the electrical force, $\mathbf{F}_E = \sigma \mathbf{E} \times \mathbf{B}$, where $\mathbf{E}$ is the electrical field strength. The electrical force is constant and independent of the local flow direction. Applying a Lorentz force on a low conductivity liquid based on the electrical force may lead to an increased understanding of the effect of external forcing on the flow while the benefits of a transparent liquid at room temperature are still present.

1.1.6 Discussion

As discussed above, flow and heat transfer in transparent liquids in scale models of the casting mould do not fully reflect the mechanisms of the continuous casting process, so measurement results cannot be used directly for the improvement of the actual casting processes. However, if the relevant physical mechanisms in the continuous casting process are captured in the scale model, the results can be used for validation of numerical methods.

Figure 1.2 shows the relationship between the experimental results and the improvement of the continuous casting process, via computational models that are validated and improved using the scale model experiments.

1.2 Objectives

In the present work, the flow of water jets issuing from submerged nozzles into thin water filled cavities with a free upper liquid surface has been studied experimentally. This was done to mimic the flow in configurations similar to the flow in a continuous casting mould.

The research questions addressed in this thesis are threefold. The first research question is "*What is the mechanism leading to self-sustained oscillations of jets issuing into thin cavities?"*. The self-sustained jet oscillations may or may not be desired and a better understanding of the physical mechanism leading to the oscillations may lead to a better understanding of how to influence the oscillations.

The second research question is " *What is the effect of the self-sustained jet oscillations on the heat transfer and temperature distribution in a thin cavity with flow from a bifurcated nozzle?*".

The third research question is "*What is the effect of electromagnetic forcing on the self-sustained oscillations of jets issuing into thin cavities*". We study the effect of electromagnetic forcing on the frequency and amplitude of the jet oscillations to verify if it is possible to enhance or suppress the jet oscillations.

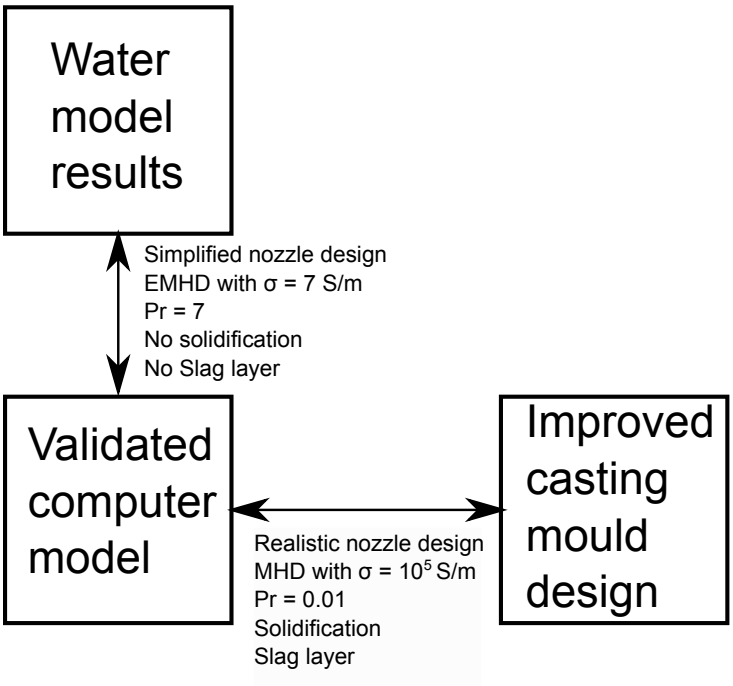

Figure 1.2: Schedule of how to use the results from the performed experimental work. The results from the water model can be used as validation data for computational models, which then can be used to improve the continuous casting process.

1.3 Outline

This thesis consists for the largest part of articles, published in various journals. The details of the experimental setup and the applied experimental techniques vary from chapter to chapter, and are therefore described in each chapter separately.

Chapters 2 and 3 describe the fluid flow regimes in thin cavities with flow from a submerged bifurcated nozzle, as a function of the nozzle depth, inlet velocity and width-to-thickness ratio of the cavity. Reynolds numbers encountered, based on the inlet velocity and on the nozzle dimensions, are between $5\times10^3 < \mathrm{Re} < 3.5 \times 10^4$. Furthermore, in chapter 2 also a discussion of the mechanism leading to self-sustained jet oscillations in a configuration with two jets issuing into a thin cavity is presented.

Chapter 4 describes the temperature distribution and heat transfer in a thin

cavity with flow from a submerged bifurcated nozzle, when one of the broad walls of the cavity is cooled. The (time-dependent) temperature distribution at the cooled wall is measured using thermochromic liquid crystals.

In chapters 5 and 6, the effect of electromagnetic forcing on self sustained jet oscillations is studied. In chapter 5 this is done for a single jet issuing downward into a thin cavity, while in chapter 6 this was done for the flow from a bifurcated nozzle into a thin cavity. The electromagnetic forcing is applied to investigate if it is possible suppress or enhance the self-sustained jet oscillations. To ensure a significant electromagnetic forcing, as compared to inertial forces, Reynolds numbers encountered in chapters 5 and 6 are between $0 < \mathrm{Re} < 7.1 \times 10^3$, which is much lower than the Reynolds numbers encountered in chapters 2 and 3.

Chapter 7 presents the main conclusions of this work, and it presents a discussion of the main findings and their usability for the continuous casting problem. This puts the experimental results in a broader perspective with a clear indication of the practical relevance. This chapter also presents a possible outlook for further possibilities in experimental studies of the flow in the mould of a continuous casting machine.

Chapter 2

Oscillations of the fluid flow and the free surface in a thin cavity with a submerged bifurcated nozzle[1]

The free surface dynamics and sub-surface flow behavior in a thin (height and width much larger than thickness), liquid filled, rectangular cavity with a submerged bifurcated nozzle were investigated using free surface visualization and particle image velocimetry (PIV). Three regimes in the free surface behavior were identified, depending on nozzle depth and inlet velocity. For small nozzle depths, an irregular free surface is observed without clear periodicities. For intermediate nozzle depths and sufficiently high inlet velocities, natural mode oscillations consistent with gravity waves are present, while at large nozzle depths long term self-sustained asymmetric oscillations occur.

For the latter case, time-resolved PIV measurements of the flow below the free surface indicated a strong oscillation of the direction with which each of the two jets issue from the nozzle. The frequency of the jet oscillation is identical to the free surface oscillation frequency. The two jets oscillate in anti-phase, causing the asymmetric free surface oscillation. The jets interact through a cross-flow in the gaps between the inlet channel and the front and back walls of the cavity.

[1]Published in International Journal of Heat and Fluid Flow 44: 365-374, 2013

2.1 Introduction

Flow instabilities in liquid filled cavities with submerged single and bifurcated nozzles and a free liquid surface are of great practical importance in the field of continuous casting. Configurations encountered, based on the width-to-thickness ratio (W/T), are billet casting ($W/T \approx 1$), thick slab casting ($4 < W/T < 10$) and thin slab casting ($W/T > 15$). Flow instabilities and resulting instabilities of the free surface have a large influence on the heat transfer to the mould and to the free surface and have detrimental impact on the steel quality. These instabilities may be suppressed, and production rate increased, by modifying the configuration of the continuous caster mold and the shape of the injection nozzle.

In the present paper, as in many earlier publications, these instabilities are studied in a scaled cold water model. The suitability of scaled cold water models in the study of continuous casting was discussed by Chaudhary et al. (2009).

Honeyands and Herbertson (1995) present a mechanistic study on the origin of flow instabilities in liquid filled cavities with submerged nozzles and a free liquid surface. They observed self-sustained asymmetric oscillations of the free surface in a $W/T = 25$ cavity with a submerged bifurcated nozzle. To explain the oscillations they set up a simple numerical model for a vertically downward directed jet from a submerged single nozzle into a cavity. They argue that the surface oscillations are due to self-sustained jet-oscillations, and qualitatively apply the results for the single jet case to the case with jets from a bifurcated nozzle. Such self-sustained oscillations are known to occur when the jet shear layer is bounded by recirculation zones that are present in confined geometries (Rockwell 1983, Rockwell and Naudascher 1979). Examples include the case of a jet flowing into a blind cavity (Gebert et al. 1998, Honeyands and Herbertson 1995, Lawson and Davidson 2001, Maurel et al. 1996, Molloy 1970, Molloy and Taylor 1969), flows over cavities (Farkas et al. 2012, Rockwell and Naudascher 1978, Rowley et al. 2002, Rowley and Williams 2006, Tam and Block 1978) and flows over backward facing steps (Wee et al. 2004, Yokoyama et al. 2007). Self-sustained oscillations are of a much lower frequency than oscillations driven by the shear layer of the jet.

Flow regime maps, indicating the boundaries between regions with, and without flow and free surface instabilities, for vertically downward directed submerged single jets in cavities with width-to-thickness ratios W/T varying from 1 to 10 have been published (Lawson and Davidson 2001, Mataoui and Schiestel 2009, Maurel et al. 1996). The nozzle-exit to bottom distance and the inlet velocity are used as independent parameters. Flow regime maps have also been reported for self-sustained sloshing of the free surface in a cavity due

to oscillations of a vertically upward directed submerged single jet impinging on the free surface. These flow maps are given for $W/T = 1$ (Madarame and Iida 2001) and $5 < W/T < 35$ (Bouchet et al. 2002). Here the nozzle-exit to surface distance and the inlet velocity are the independent parameters. Saeki et al. (2001) report a flow regime map for self-sustained sloshing of the free surface in a cavity with $W/T = 10$ due to a horizontally directed submerged single jet with the nozzle submergence depth and the inlet velocity as the independent variables.

Configurations with two jets, emerging in opposite horizontal directions from a bifurcated vertical nozzle submerged in a cavity, as commonly applied in continuous casting, are distinctly different from the configurations described above. Unlike single vertical jet configurations, the jets from a bifurcated nozzle have a velocity component towards the cavity sidewalls and perpendicular to the direction of gravity. Unlike single horizontal jet configurations, bifurcated nozzle configurations are geometrically symmetrical in the horizontal direction. In the experimental investigation of flows in thin-slab continuous casting, water models employing replicas of industrial (often bifurcated) nozzles have been used together with funnel shaped cavities to mimic the industrial process as close as possible. This has resulted in an incomplete, and somehow inconsistent, picture of the nature of flow instabilities in these configurations. Honeyands and Herbertson (1995) report the self-sustained oscillations (as mentioned above) with a frequency of 0.2 Hz, but on top of that they find a suppressed oscillation in a natural mode of 0.7 Hz. Miranda-Tello et al. (2012) report an oscillation in a natural mode of 2.5 Hz with a less pronounced self-sustained oscillation with a frequency of 0.08 Hz. Gupta and Lahiri (1994) also report low frequency oscillations below 0.1 Hz, but they report a time dependent variation of frequency. Torres-Alonso et al. (2007) report a stable free surface profile with a periodic distortion of this stable profile with a frequency of 0.01 Hz. Jeon et al. (2010) report oscillations in a natural mode of gravity waves in the width of the caster mold with a frequency of 0.8 Hz.

The flow in a thin cavity from a submerged bifurcated nozzle can be seen as a simplified representation of the flow in a continuous casting mould. Dauby (2011) reports single roll, double roll and an unstable flow patterns in thin slab continuous casting from a bifurcated nozzle. The importance of the mould width, nozzle submergence depth and inlet velocity are indicated as the parameters that determine the flow pattern.

The present paper presents a flow regime map for the flow in a cavity with width-to-thickness ratio $W/T = 18$ and a submerged bifurcated nozzle. The nozzle emits equal amounts of liquid towards the side walls and the jets are directed parallel to the broad walls of the cavity. The inlet velocity and

the nozzle submergence depth are the independent parameters. In order to quantitatively study the mechanism behind the oscillations, the sub-surface flow is correlated to the free surface behavior for the different regimes, using time-resolved PIV measurements of the sub-surface flow and high-speed visualization of the free surface.

2.2 Physical modeling

2.2.1 Experimental set up

The experiment is conducted in a rectangular glass cavity, schematically shown in figure 2.1. The inner dimensions of the cavity are 0.8 × 0.65 × 0.035 m^3 (= H × W × T = height × width × thickness) and it is filled with water to a height h = 0.7 m.

Water is fed into the cavity through a square cross section nozzle of 0.6 m length with outer dimensions of 0.02 × 0.02 m^2 and inner bore dimensions of $d \times d$ = 0.01× 0.01 m^2. The average flow velocity in the nozzle is $2 \times v_{in}$. The nozzle is closed at the end, but has two square outflow openings of $d \times d$ = 0.01 × 0.01 m^2 in opposite sidewalls near the end of the nozzle, perpendicular to the nozzle cross section, as shown in the insert image in figure 2.1. Note that the average inlet velocity v_{in} is defined as the volumetric flow rate of liquid emerging into the cavity devided by the nozzle outflow area. It is known that due to a low dynamic pressure in the upper part of the nozzle opening the liquid flow may be unevenly distributed over the outflow area. The end of the nozzle is at a depth d_n below the equilibrium free surface level. Water emerges in the direction of the sidewalls of the cavity from each of these two openings, with an average velocity v_{in}. The nozzle submergence depth is varied between 0.05 m and 0.35 m, or $0.08W$ – $0.54W$ which is a broader range than the $\sim 0.09W$– $0.11W$ commonly applied in continuous casting (Dauby (2011)).

Through two 0.04 × 0.035 m^2 rectangular holes near the center of the bottom of the cavity, water is pumped out of the cavity into an external flow circuit and back into the nozzle, maintaining a constant volume of water in the cavity. The water is kept at a constant temperature (within 0.5°C) by means of an immersion cooler in the external circuit, this is done to guarantee a constant viscosity of the liquid. The inlet flow rate is varied between 0.1 l/s and 0.6 l/s, corresponding to Reynolds numbers, based on d and v_{in} of 5.0×10^3 to 3.0×10^4. This range of Reynolds numbers is in the low range of Reynolds numbers encountered in the continuous casting process Najjar et al. (1995).

For further reference, an orthogonal coordinate system is defined with its origin located at the equilibrium position of the free liquid surface in the center

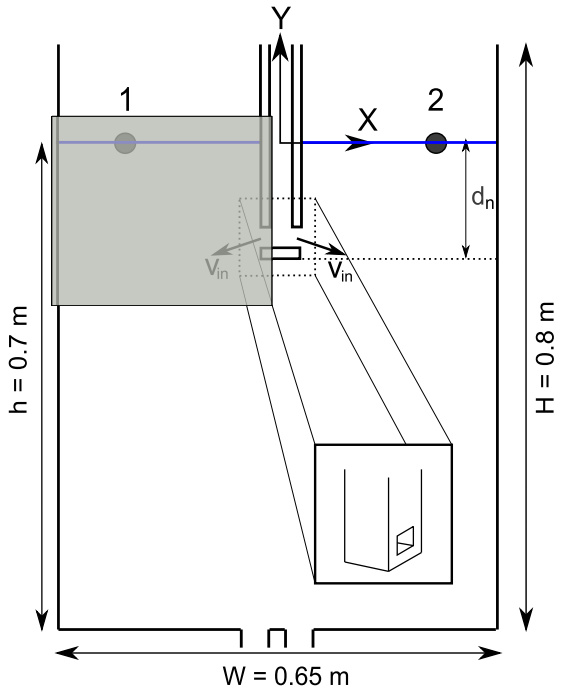

Figure 2.1: Schematic of the experimental flow configuration. The inner dimensions of the cavity are H $\times$ W $\times$ T = 0.8 $\times$ 0.65 $\times$ 0.035 m^3. Water is fed into the cavity through a square cross section nozzle of 0.6 m in length with outer dimensions of 0.02 $\times$ 0.02 m^2 and inner bore dimensions of $d \times d$ = 0.01$\times$ 0.01 m^2. The nozzle is submerged to a depth d_n, which is varied between 0.05 m and 0.35 m. Water exits the nozzle through two square exit ports $d \times d$ = 0.01 $\times$ 0.01 m^2 in opposite side walls of the nozzle, as schematically shown in the inserted image. The cavity is filled up to $h = 0.7$ m with water and the outflow is through two holes of 0.04 $\times$ 0.035 m^2 near the center of the bottom of the cavity. The grey region in the top left corner is the field of view for the PIV measurements. The light sheet is located exactly in the center plane between the two broad walls at $z = 0$. The two black dots at $x = \pm$ 0.175 m are monitoring points for measurements of the free surface elevation.

of the cavity. The x-axis is parallel to the equilibrium free liquid surface and to the front wall of the cavity, and the y-axis is in the upward vertical direction. The free surface elevation, relative to $y = 0$, is denoted by η.

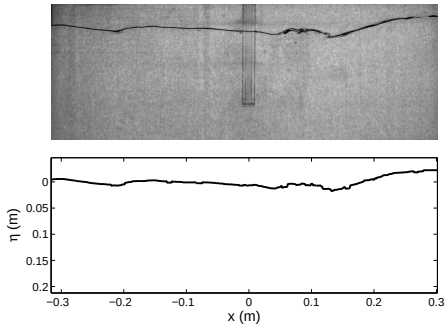

Figure 2.2: *Top*: Image of the instantaneous free surface with v_{in} = 2 m/s and d_n = 0.15 m. *Bottom*: Detected free surface position.

2.2.2 Measurement methods

Free surface tracking

Images of the capillary line at the front wall of the cavity are used for the tracking of the free surface. Since the thickness T of the cavity is small compared to the width W, it is assumed that the position of the capillary line gives a good representation of the location of the free surface. A Photron SA1 high-speed camera, equipped with an extended 32 GB internal memory, is used to take 1.1 $\times$ 10^4 images of the free surface at a frame rate of 50 Hz and with a resolution of 1024 $\times$ 512 pixels. Figure 2.2 (top) shows an original image of the instantaneous free surface and the detected free surface elevation is given in figure 2.2 (bottom). The spatial resolution is 0.63 mm/pixel and the image of the capillary line is about three pixels thick over the entire width of the cavity. The analysis of the images is carried out in Matlab, using a steepest gradient detection method that determines the upper and lower edge of the free surface. The mean of the upper and lower position of the maximum gradient is used as the position of the free surface.

PIV system

A Quantronix Darwin DUO 527-80-M laser and light sheet optics are used to produce a laser light sheet that enters the cavity through the bottom wall. The laser produces 50 mJ pulses at a wavelength of 527 nm and a repetition rate of 500 Hz. Neutrally buoyant silver coated hollow glass spheres with a nominal diameter of 25 μm are used as seeding particles. The field of view has size 0.35 $\times$ 0.35 m^2 and is located in the top left corner of the cavity in the z = 0

mid plane between the broad walls, as shown in figure 2.1. The light sheet thickness in the region of measurements is less than 1 mm. Particle images are recorded with an Imager pro HS 4M camera with a Nikon 55 mm Nikkor 1:2.8 lens with an f-stop of 16. The camera is equipped with a 2016 $\times$ 2016 pixel CMOS-chip with a pixel size of 11 μm. This results in a spatial resolution of 0.17 mm/pixel. Velocity vectors are calculated based on cross correlation of interrogation areas of 32 $\times$ 32 pixels with 50 % overlap using Davis 8.1 PIV software. Invalid vectors were discarded by applying a window velocity filter and data smoothing was based on 3 $\times$ 3 matrix interpolation. The entire flow field can be resolved, except for two regions. The first is in the jet region close to the nozzle outlet openings, where no correlation can be made to a previous position of the seeding particles in the flow. The jet is well resolved at a distance of 3 to 5 cm from the nozzle. The second region is near the free surface where reflections disturb the particle images. However, the global behavior of the jet can be resolved properly.

2.3 Time-averaged free surface profiles

Time-averaged free surface profiles are calculated from the instantaneous free surface profiles by calculating the average value at every x-position during the time of the measurement. Figure 2.3 shows the time-averaged free surface profiles for a fixed inlet velocity v_{in} of 2 m/s while the nozzle depths d_n vary between 0.06 and 0.25 m. It is seen that the mean surface profiles are symmetric around the nozzle position. For different nozzle depths there are both qualitative and quantitative differences between the mean free-surface profiles. In the case of d_n = 0.06 m, two local minima are present in each half of the mean free surface profile. At d_n = 0.08 m the outer minimum has disappeared and the minimum closest to the nozzle has shifted toward the side wall. In the case of d_n = 0.09 m the local minimum in the free surface is closer to the side walls of the cavity and the surface elevation at the position of the nozzle has increased. For a d_n = 0.1 m, the minima in the free surface profile are located at x = $\pm$0.2 m. Figure 2.3 (bottom) shows the mean free surface profiles for larger nozzle depths and it is seen that the profiles are qualitatively the same. The minima are located at x = $\pm$ 0.15 to 0.19 m and the mean wave amplitudes, defined as $A = \eta_{max} - \eta_{min}$, are 0.015 m $\pm$ 0.002 m.

Figure 2.4 shows the mean free surface profiles in the cavity for varying inlet velocities and a constant nozzle depth. The mean wave height grows with increasing inlet velocity as expected from an energy balance. A Froude similarity was proposed by Anagnostopoulos and Bergeles (1999) as

$$\frac{v_{in}^2}{gA} = \alpha, \tag{2.1}$$

where v_{in} is the inlet velocity, g is the gravitational acceleration, A is the mean wave amplitude and α is a similarity constant. From the mean profiles shown in figure 2.4 it follows that $\alpha = 30 \pm 5$.

2.4 Transient free surface profiles

The results of the measurements of the time averaged free surface profiles for different nozzle depths suggest that there are three flow regimes in the cavity, depending on the nozzle depth. This section focuses on the transient behavior of the free surface for these three regimes. Figure 2.5 summarizes the transient free surface profiles for flows with nozzle depths d_n of 0.06, 0.08 and 0.09 m at a fixed inlet velocity v_{in} of 2 m/s. Time is on the horizontal axis, the x-coordinate along the width of the cavity is on the vertical axis. At every time instant, the instantaneous free surface elevation profile along the width of the cavity is depicted by a vertical line of varying colour, where a dark tone represents a low surface elevation, and a light tone represents a high surface elevation. At d_n = 0.06 m, the transient surface elevation profile shows no distinct periodicity. Local minima in the free surface elevation are fixed in place at x = $\pm$ 0.05 m and at x = $\pm$ 0.2 m. In the case of d_n = 0.08 m, a clear repetitive pattern is seen with a frequency of approximately 1 Hz, which is the natural frequency for gravity waves in the cavity (Lamb 1932). When the nozzle is placed at a depth of 0.09 m, a repetitive pattern with a frequency of approximately 0.2 Hz is seen.

2.5 Flow regimes

The qualitative differences in the mean and transient free surface profiles suggest the existence of three different flow regimes inside the cavity. These flow regimes will be discussed in this section. The nozzle depth d_n is varied between 0.05 m and 0.35 m and the inlet velocity v_{in} is kept constant at 2 m/s unless stated otherwise. The different flow regimes are labelled according to their free surface behavior. In regime I there is an irregular free surface pattern without distinct periodicities. Such a flow pattern has also been observed in actual continuous casters and is referred to as the single-roll regime by Dauby (2011). Regime II is characterized by free surface movement

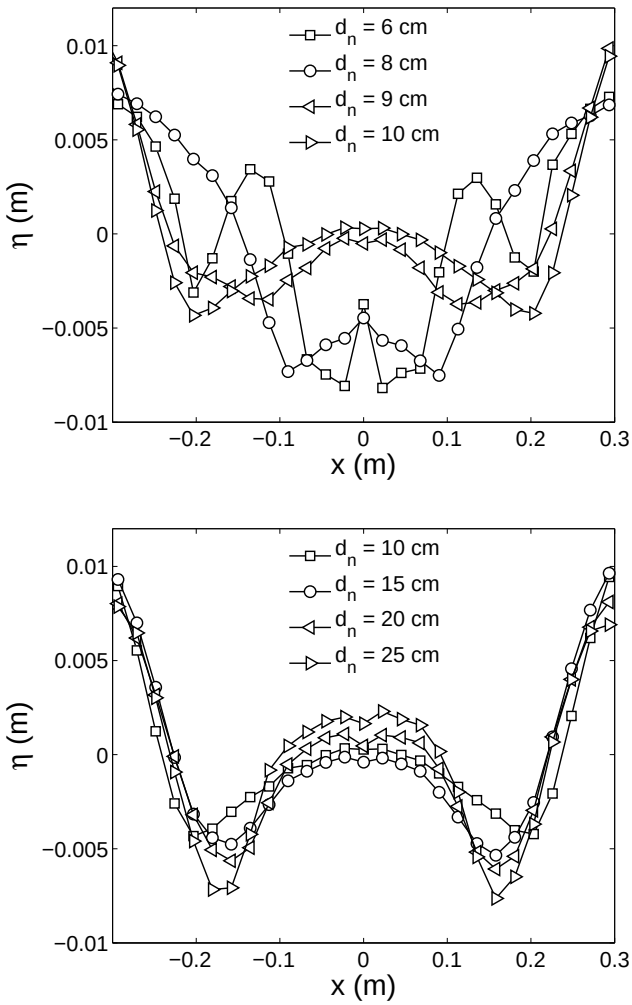

Figure 2.3: Time averaged free surface profiles for v_{in} = 2 m/s. *Top*: nozzle depths d_n of 0.06 m to 0.1 m. Qualitatively, three different profiles are found. *Bottom*: nozzle depths d_n of 0.1 to 0.25 m. Qualitatively, the time averaged free surface profiles do not change.

with oscillations in a natural mode for gravity waves in the cavity. This regime might relate to the unstable regime as indicated by Dauby (2011). In

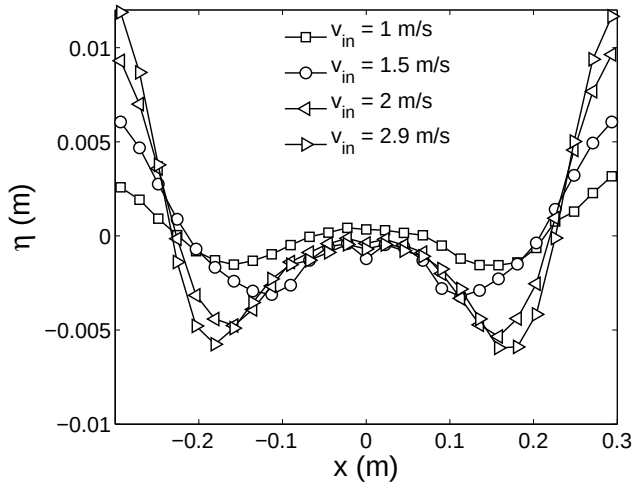

Figure 2.4: Time averaged free surface profiles for d_n = 0.15 m and varying inlet velocity.

regime III free surface movement with self-sustained long term oscillations occurs. This regime is referred to as the double-roll regime by Dauby (2011). Regime I is divided in a pattern with bubble entrainment, regime Ia, and a regime without bubble entrainment, regime I b. Regime II is divided in a first mode asymmetrically oscillating free surface, regime IIa, and a second mode symmetrically oscillating free surface, regime IIb. Regime III is divided in three sub-regimes, regime IIIa with free surface disturbances without bubble entrainment, regime IIIb with free surface disturbances with bubble entrainment and regime IIIc with sub-surface oscillations without noticeable free-surface elevation

2.5.1 Regime I: Irregular free surface elevation

For nozzle depths d_n less than 0.06 m, the upper shear layers of the jets from the nozzle reach the free surface before impinging on the side walls of the cavity as schematically shown in figure 2.6a. In regime I a, this causes direct bubble entrainment at the free surface for d_n <0.04 m. The air entrainment is caused by turbulent eddies close to the free surface. The mechanism of entrainment closely resembles that of by self-aerated flows (Chanson 1996). In regime I b, 0.04 m $< d_n <$ 0.06 m, bubble entrainment does not take place and

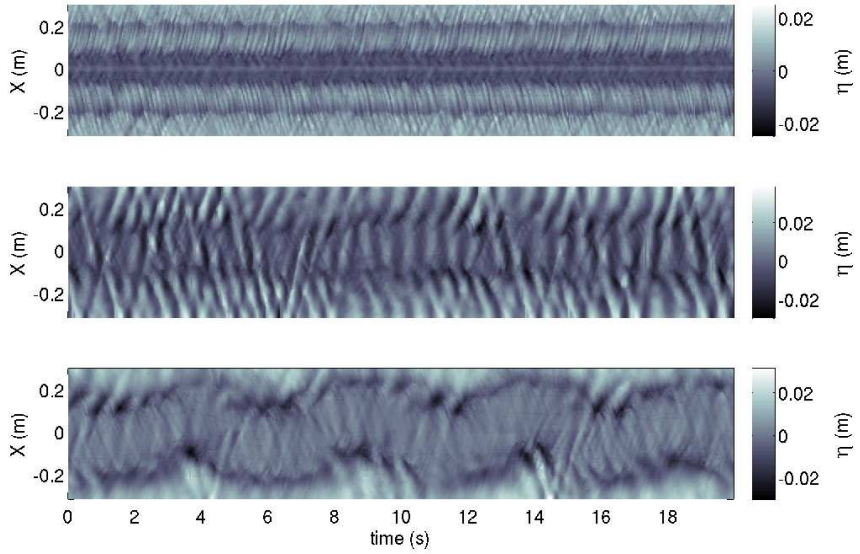

Figure 2.5: Transient surface elevation profiles for v_{in} = 2 m/s and nozzle depths d_n of 0.06, 0.08 and 0.09 m. Time is on the horizontal axis and the x-coordinate is on the vertical axis. A vertical line in the plot exists of varying tone value, where a dark tone represents a low surface elevation and a light tone represents a high surface elevation. For d_n = 0.06 m a steady surface elevation pattern without distinct periodicities is observed. At d_n = 0.08 m an oscillating pattern with a frequency of roughly 1 Hz is seen and for d_n = 0.09 m a frequency of 0.2 Hz occurs.

an irregular pattern of surface disturbances occurs as illustrated in figure 2.5 (top). To study the irregular behavior of the free surface in more detail, a time trace of the free surface elevation at monitoring point 1 is used to calculate a power spectrum. The result is shown in figure 2.7a. The power spectrum is essentially flat, without a distinct spectral peak, thus characteristic for white noise. Figure 2.8 shows four sequential snapshots of the velocity field below the free surface. It is shown that the overall flow pattern does not change in time, resulting in a relatively stable free-surface profile.

2.5.2 Regime II: Oscillations at a natural frequency for gravity waves in the cavity

At nozzle depths d_n around 0.1 m and inlet velocities v_{in} of 2 m/s or higher, oscillations occur with frequencies corresponding to the natural frequency of

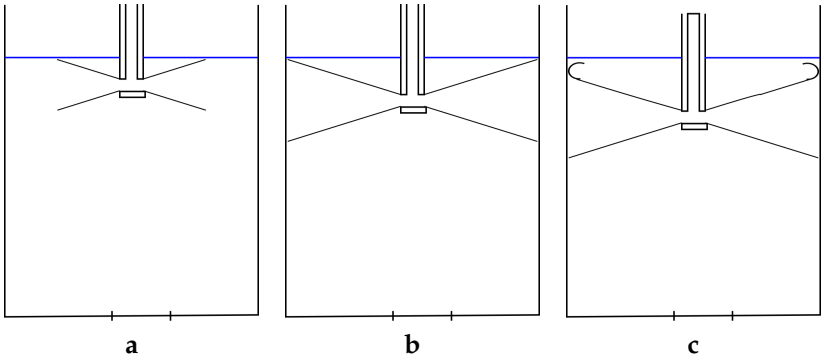

Figure 2.6: Schematic jet configurations in the cavity with a bifurcated nozzle. **a.** Regime I: The jet shear layer reaches the free surface before it impinges the side wall, causing an irregular pattern of surface disturbances when the nozzle depth d_n is smaller than the critical nozzle depth d_c. **b.** Regime II: The upper shear layer of the jet reaches the free surface at the same moment it reaches the side wall causing oscillations with the natural frequency of gravity waves in the cavity ($d_n = d_c$). **c.** Regime III: The jet impinges on the side wall below the free surface with the possibility of a recirculating flow between the jet and the free surface causing long term self-sustained free surface oscillations ($d_n > d_c$).

gravity waves in the cavity. The natural frequency for gravity waves in a rectangular cavity is given by Lamb (1932) as

$$f = \sqrt{\frac{g}{2\pi\lambda} \tanh\left(\frac{2\pi h}{\lambda}\right)}, \tag{2.2}$$

where g is the gravitational acceleration, h is the water height and λ is the wave length which is equal to $2W$ in case of the first mode (asymmetric) oscillation in regime IIa or equal to W in case of the second mode (symmetric) oscillation in regime IIb. For large water heights h equation (2.2) reduces to

$$f = \sqrt{\frac{g}{2\pi\lambda}}. \tag{2.3}$$

In the cavity considered in this research, the first mode oscillation corresponds to a frequency of 1.09 Hz and the second mode oscillation corresponds to a frequency of 1.56 Hz. For d_n = 0.08 m and v_{in}= 2 m/s the surface elevation at monitoring point 1 was registered as a function of time. The power spectrum determined from this time trace is shown in figure 2.7b. A clear peak is visible at a frequency of 1.0 Hz with a power density value which is much higher

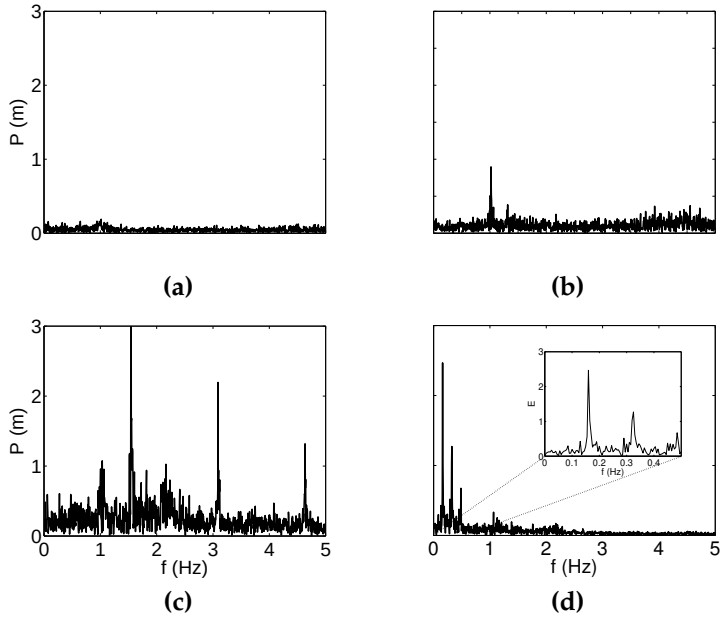

Figure 2.7: Power spectra of the free surface elevation measured at monitoring point 1. **a.** Regime I: $v_{in} = 2$ m/s and $d_n = 0.06$ m. **b.** Regime IIa: $v_{in} = 2.5$ m/s and $d_n = 0.08$ m. **c.** Regime IIb: $v_{in} = 2.9$ m/s and $d_n = 0.1$ m. **d.** Regime IIIa: $v_{in} = 1.5$ m/s and $d_n = 0.1$ m, the inserted image shows the spectrum for $f < 0.5$ Hz.

than the power density values for the irregular pattern (figure 2.7a). The frequency of 1.0 Hz is in good agreement with the first natural oscillation mode. Figure 2.7c shows the power spectrum of a time trace at monitoring point 1 for d_n = 0.1 m and v_{in} = 2.9 m/s. In addition to the peak at 1.0 Hz, a clear peak at f = 1.55 Hz is seen, in close agreement with the second natural mode. Second and third harmonics are found at f = 3.1 Hz and at f = 4.65 Hz.

Figure 2.9(top) shows the transient free surface profile for the asymmetric natural mode, regime IIa and figure 2.9 (bottom) shows the transient free surface profile for the symmetric natural mode, regime IIb. The tilted profiles in the asymmetric natural mode indicate traveling waves over the free surface, while the straight profiles in the symmetric mode indicate standing waves at the free surface. From the graphs it is also seen that the wave amplitude in the symmetric mode is almost twice as large as the wave amplitude in the asymmetric mode.

Natural mode oscillations occur when the inlet velocity v_{in} is 2 m/s or

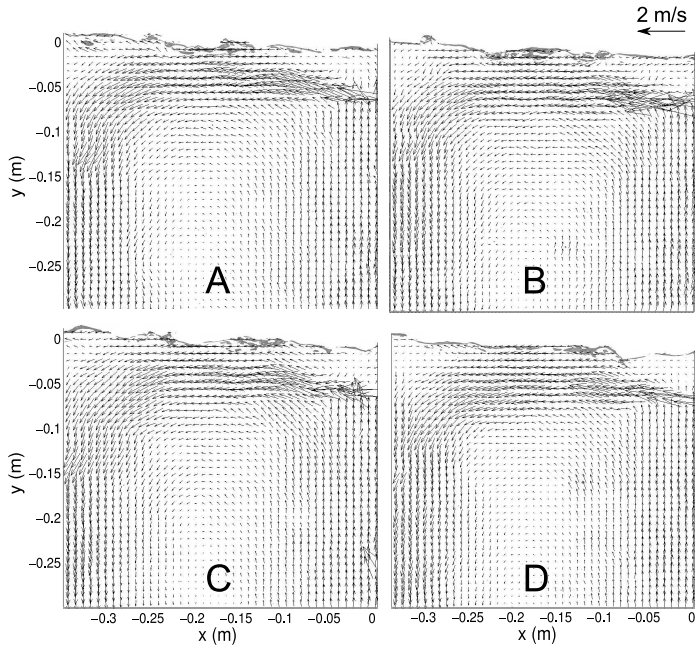

Figure 2.8: Four sequential snapshots of the velocity field with v_{in} = 2 m/s and d_n = 0.06 m (regime Ib). The time between the snapshots is 1 second. It is seen that the overall flow pattern does not change significantly over time. The field of view is 0.35 × 0.35 m^2 and the nozzle is located in the top right corner, as depicted in figure 2.1. The PIV plane is located at the z = 0 mid plane of the cavity. The dark irregular line is the position of the free surface.

higher and when the upper shear layer of the jet reaches the free surface at the same moment it reaches the side wall. This is schematically shown in figure 2.6b. The spreading half-angle of a free turbulent round jet is approximately 12° (Pope 2000). For this spreading half-angle and a half width of the cavity of 0.325 m, the shear layer of the jet would reach the side wall and the free surface at the same time when $d_n = 0.065$m. However, the jet is confined between the front and back wall , so the jet angle in the vertical direction needs to be increased to accommodate for the same amount of fluid to pass through. This results in a critical nozzle depth d_n which is larger than 0.065 m, consistent with the measurement results.

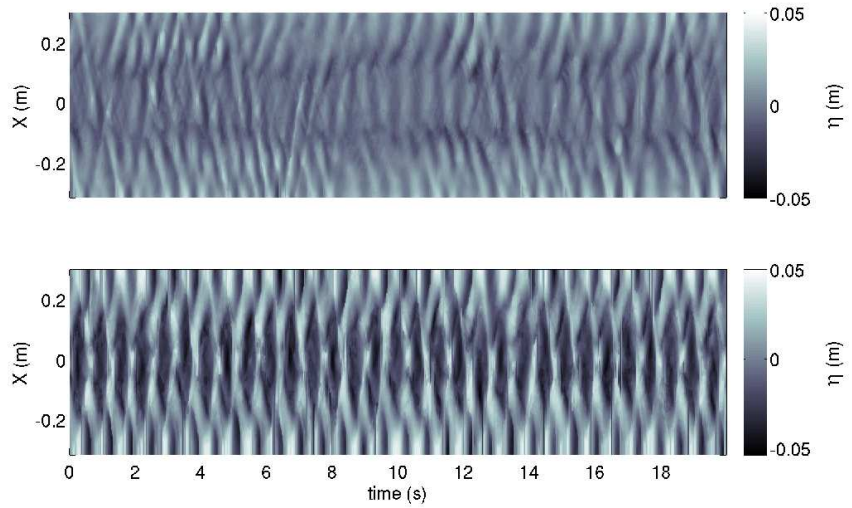

Figure 2.9: *Top*: Transient surface elevation profiles for v_{in} = 2 m/s and d_n = 0.08 m. This is the (asymmetric) first mode oscillation in regime IIa. *Bottom*: Transient surface elevation profiles for v_{in} = 2.9 m/s and d_n = 0.1 m. This is the (symmetric) second mode oscillation in regime IIb. In the symmetric natural mode a much larger wave amplitude is observed.

2.5.3 Regime III: Asymmetric self-sustained oscillations

At nozzle depths $d_n \geq 0.1$ m and all inlet velocities, the free surface oscillates with frequencies that are different from the natural frequencies for gravity waves in the cavity. Typical asymmetric oscillations with frequencies between 0.1 and 0.3 Hz are found in a wide range of inlet velocities and nozzle depths $d_n > 0.1$ m. Regime III is divided in three sub-regimes, regime IIIa, with self-sustained asymmetric free surface oscillations without bubble entrainment, regime IIIb with self-sustained asymmetric free surface oscillations with bubble entrainment and regime IIIc with self-sustained jet oscillations without noticeable free surface movement.

Figure 2.10 shows time traces of the free surface elevation in regime IIIa, measured in both monitoring points for v_{in} = 1 m/s and d_n = 0.1 m. The time traces show anti-phase oscillating behavior. Figure 2.7d shows the power spectrum that was determined from one of the time traces. The largest spectral peak occurs at 0.16 Hz. Second and third harmonics are found at f = 0.32 Hz and at f = 0.48 Hz.

The presence of a clear single frequency in the present $W/T = 18$ cavity

deviates from the findings of Lawson and Davidson (2002), who carried out LDA measurements in a $W/T = 6$ cavity with a bifurcated nozzle. It is speculated that the differences between the results of Lawson & Davidson and the present work are caused by the differences in width-to-thickness ratios of the cavities. A small width-to-thickness ratio results in a more three dimensional flow behavior as was shown in a numerical study by Real-Ramirez and Gonzalez-Trejo (2011) who compared the flows in a W/T = 10 cavity with the flow in a W/T = 3 cavity. There is less coherence between the jet motion and the free surface motion, and less coherence between the two jets. This view is supported by the results of experiments in a $W/T = 25$ cavity with a bifurcated nozzle, reported by Honeyands and Herbertson (1995), who indeed observed the presence of a single frequency as well.

For inlet velocities $v_{in} \geq 1.5$ m/s bubble entrainment may occur in regime IIIb, as illustrated in figure 2.11. This sequence of images captures a bubble entrainment event in the left half of the cavity for v_{in} = 2.5 m/s and d_n = 0.15 m. The first image shows the free surface just before break up. High velocity fluid comes from the wall on the left and plunges into the more or less stagnant fluid near the nozzle on the right. In the second image an air pocket is formed below the local minimum in the free surface. In the third image the air pocket is transported to the bulk of the cavity and a second air pocket is formed. In the bottom image the second air pocket is also transported to the bulk of the cavity. The air pockets break up due to turbulent stresses. Part of the entrained air will flow back to the free surface due to buoyancy, but some bubbles may be transported to the jet region, where they break up into smaller bubbles that get trapped in the bulk flow below the nozzle. Bubble entrainment events occur at the same frequency as that of the asymmetric oscillation. The mechanism of bubble entrainment described above is similar to the mechanism with which air is entrained by plunging jets or hydraulic jumps (Chanson 1996, Kiger and Duncan 2012).

For the low frequency free surface oscillation to exist, the inlet velocity v_{in} needs to be higher than 0.5 m/s. When the jet velocity is too low, jet oscillations occur, but the flow is too weak to influence the free surface elevation, this is regime IIIc. From the Froude criterion formulated earlier it follows that for inlet velocities less than 0.5 m/s, the mean free surface amplitude is less than 1 mm. These small amplitudes cannot be captured in the measurements and the free surface is essentially flat.

Self-sustained oscillation mechanism

The flow field below the free surface in regime IIIa was measured with time-resolved PIV with the aim to unravel the origin of the free surface

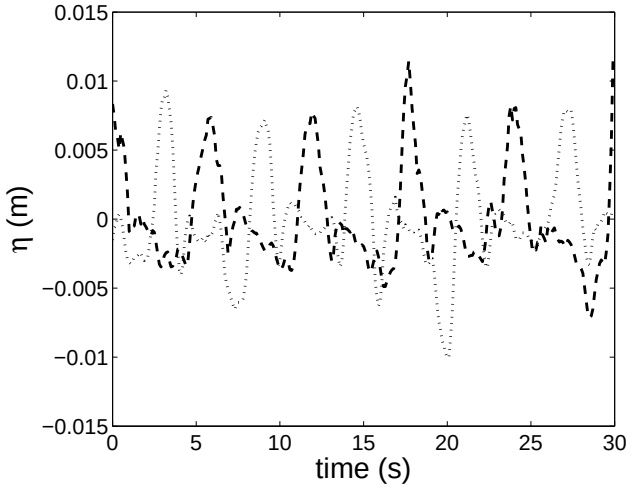

Figure 2.10: Time traces of the free surface elevation at monitoring points 1 and 2 with v_{in} = 1.5 m/s and d_n = 0.1 m (regime IIIa).

oscillations. Results are shown in figure 2.12. Each image shows an instantaneous velocity field in the left half of the cavity as illustrated in figure 2.1. The left one of the two jets from the bifurcated nozzle issues leftward from the nozzle on the right, and subsequently impinges on the side wall on the left. There, the jet splits into two parts, one part moving upward to the free surface and one part moving downward to the bottom of the cavity. The fluid moving upward forms a recirculation zone in between the free surface and the horizontal plane through the nozzle exit, while the downward moving fluid feeds a (large) recirculation zone below the horizontal plane through the nozzle exit, as illustrated in figure 2.14(top). The jet angle θ is defined as the angle between the jet and the horizontal plane through the nozzle exit, with θ positive for upward jet direction. Figure 2.13a shows a time trace of the jet angle. It is seen that the jet angle oscillates with a frequency of 0.09 Hz, consistent with the free surface oscillation frequency of 0.1 Hz observed in this regime.

If we approximate the upper recirculation zone as circular with radius R_c and center (x_c, y_c), the radial pressure gradient between the center of this recirculation zone and its edge follows from the simplified momentum

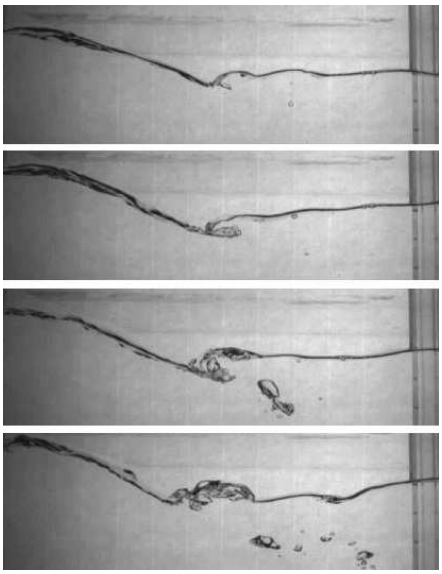

Figure 2.11: Bubble entrainment in the left half of the cavity for a flow with v_{in} = 2.5 m/s and d_n = 0.15 m, the time between the frames is 0.2 s. The nozzle is located at the right and the side wall is located on the left. The top image shows the free surface just before break up. In the second image an air pocket is entrained. In the third image a second air pocket is entrained, while the first air pocket is transported to the bulk of the cavity. In the fourth image the second air pocket is also transported to the bulk (regime IIIb).

equation for the radial direction (Heeger et al. 2010)

$$\frac{\partial p}{\partial r} = \frac{\rho w^2}{r}, \tag{2.4}$$

where p is the pressure, ρ is the density of the fluid, w is the tangential velocity and r is the radial coordinate measured from the center of the recirculation zone.

If we integrate this equation along a vertical line between the center of the recirculation zone at (x_c, y_c) and the point (x_c, y_s) at the free surface (see figure 2.14(top)), we find the mean radial pressure gradient $\Delta p/R_c$ between the center of the recirculation zone and its edge as

$$\frac{\Delta p}{R_c} = \frac{1}{y_s - y_c} \cdot \int_{y_c}^{y_s} \frac{\rho {v_x}^2}{y - y_c} dy. \tag{2.5}$$

Figure 2.13b shows a time trace of the thus obtained $\Delta p/R_c$.

It is seen in figure 2.13 that the jet angle, the mean pressure gradient, and the x- and y-coordinates of the center of the recirculation zone (x_c and y_c) have a minimum at $t \approx 27$ s mod 11 s. For $t > 27$ s the jet angle starts to increase, and when it is about zero, the pressure gradient sharply increases. The jet fluid tends to feed the (upper) recirculation zone, thus maintaining (or even strengthening) the pressure gradient.

When the momentum in the recirculation zone becomes too high, the fluid shoots through the gaps between the inlet nozzle and the front and back walls of the cavity. This induces a collapse of the recirculation zone, such that the pressure gradient rapidly decreases. This occurs just after t = 32 s, when the jet angle θ and the x-coordinate of the recirculation zone x_c center reach a maximum. The y-coordinate y_c of the recirculation zone center (figure 2.13d) keeps on growing for another 1.5 s, the time in which the jet overshoots. This is also clear from figure 2.14(bottom) where the averaged position of the recirculation center during three oscillation periods is shown. At t = 36 s the jet angle is zero degrees again and the pressure gradient now rapidly decreases. At the same time the pressure gradient in the recirculation zone below the jet axis starts to grow, drawing the jet towards the region of low pressure below the jet axis. The jet angle reaches a minimum at t = 38 s. In the right half of the cavity the same behavior is present, but in anti-phase.

When the fluid shoots through the gaps between the inlet channel and the front and back walls, it feeds the relatively weak recirculation zone in the other half of the cavity, making it stronger and thus creating the possibility to draw the jet upwards. Since the motion of the recirculation zones in the cavity is in anti-phase, it follows that there are always two strong recirculation zones and two weak recirculation zones. When the recirculation zone in the left top of the cavity is strong, also the recirculation zone in the right bottom is strong, leaving the recirculation zones in the right top and left bottom weak. Half a period later, the recirculation zones in the right top and left bottom are strong and the recirculation zones in the right bottom and left top are weak.

The interplay of jet angle, pressure gradient and momentum is in good agreement with the findings of Honeyands and Herbertson (1995) for a single jet in a cavity. They state that the driving mechanism behind the self-sustained jet oscillation is the imbalance between momentum and pressure difference.

The possibility of fluid flowing through the gap between the nozzle and the front and back walls is a requisite for the self-sustained oscillation to exist. It is observed that when this cross-flow is prevented by blocking the regions between the inlet channel and the front and back walls of the cavity, the self-sustained oscillations seize to exist, and also the onset of entrainment is delayed to a higher inlet velocity. This is in close agreement with results

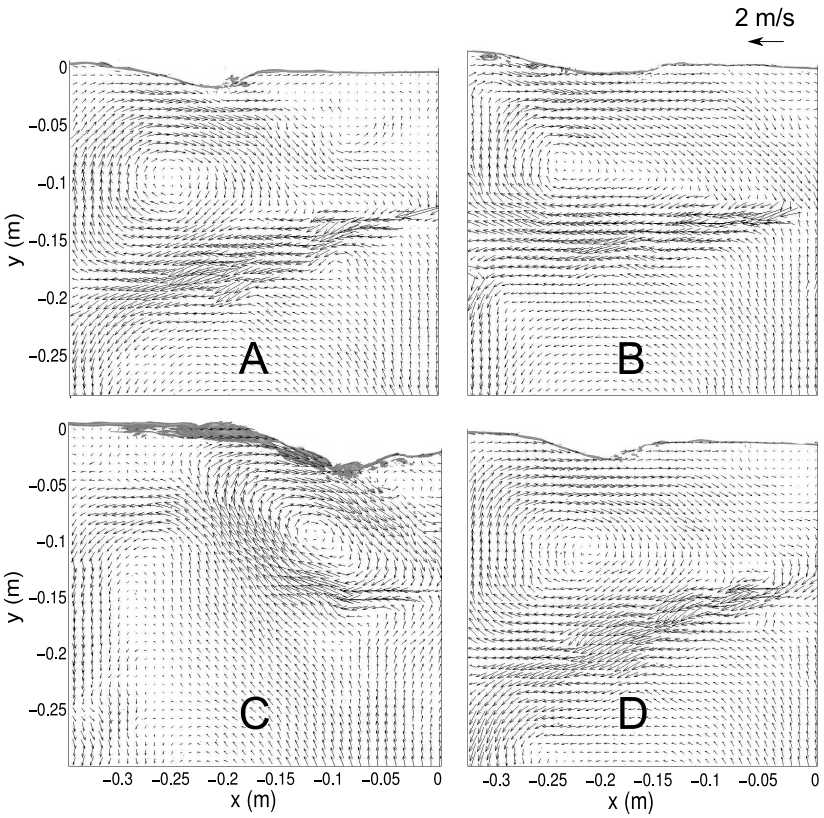

Figure 2.12: Four snapshots of half a period of the velocity field with a self-sustained oscillation of the jet, v_{in} = 2 m/s and d_n = 0.12 m (regime IIIa). The field of view is shown in figure 2.1. The PIV plane is located at the z = 0 mid plane of the cavity. The time between the images is 1.1 s resulting in a period of 6.6 s and a frequency of 0.15 Hz. It is seen that the flow pattern changes significantly. The dark line is the position of the free surface, its shape changes with the sub-surface flow pattern. The minimum in the free surface moves from a location close to the wall to a location close to the nozzle in images A to C. In image D the local minimum has returned to the position close to the wall.

from Gebert et al. (1998), who report results from a 2-dimensional model of a single jet in a cavity with a cross-flow resistance between the nozzle and the front and back walls.

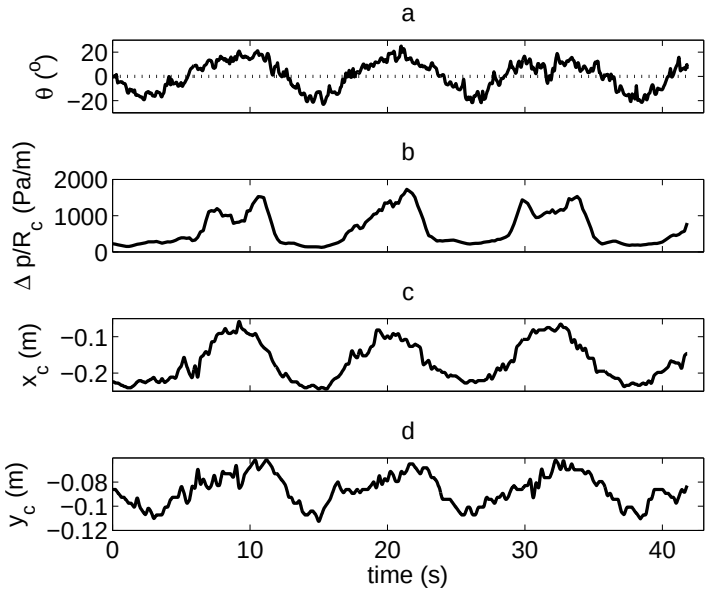

Figure 2.13: Temporal behavior of the sub-surface flow in regime IIIa with v_{in} = 1.5 m/s and d_n = 0.15 m. **a.** Time trace of the jet angle θ, the dotted line represents an angle of zero degrees. **b.** Time trace of the pressure gradient Δ_P/R_c between the recirculation center and the surroundings, calculated from equation 2.5. **c.** Time trace of the x-position x_c of the recirculation center. **d.** Time trace of the y-position y_c of the recirculation center.

2.6 Flow regime map

From the previous paragraphs it is concluded that different flow regimes exist in the cavity depending on the nozzle depth and the inlet velocity. Figure 2.15 summarises these findings in the form of a flow regime map. The flow regime map is constructed from left to right. For a range of fixed inlet velocities $0.4m/s \leq v_{in} \leq 2.8m/s$, the nozzle depth d_n is increased over a certain range. After each measurement, the pump is turned off and d_n is increased. The waiting time is sufficiently long for the fluid in the cavity and the liquid surface to become fully quiescent. Then the pump is turned on again. Once the free surface measurements at all the nozzle depths are completed, a new inlet velocity is set. In figure 2.15, going from left to right along a line of constant velocity, e.g. v_{in} = 2.5 m/s, the following regimes are identified: at

d_n <0.05 m irregular free surface behavior without distinct periodicity occurs since the shear layers of the jets reach the free surface before they impinge on the side walls. When the nozzle depth is increased to d_n = 0.08 m, the first natural mode of gravity waves in the cavity is seen. This mode is an asymmetric oscillation at a natural frequency of 1.09 Hz. At d_n = 0.09 m the second natural mode is seen, this is a symmetric oscillation at a natural frequency of 1.56 Hz. When $d_n > 0.1$ m, the natural frequencies seize to exist and the self-sustained oscillation comes into play. At an inlet velocity v_{in} = 2.5 m/s, bubble entrainment occurs, but at lower inlet velocities this is not always the case. At inlet velocities $v_{in} < 0.5$ m/s no free surface elevation is observed.

2.7 Conclusions

Experiments have been performed in a thin ($W/T = 18$), liquid filled, rectangular cavity with a submerged bifurcated nozzle and a free liquid surface. Three different regimes in the free surface behavior have been identified, depending on the nozzle depth d_n and the inlet velocity v_{in}. At nozzle depths less than a critical nozzle depth of 0.07 m, an irregular free surface pattern with no distinct oscillation frequency is observed. At nozzle depths around a critical nozzle depth of 0.09 m and inlet velocities larger than 2.5 m/s, natural mode behavior consistent with gravity waves in the cavity is observed. Both symmetrical and asymmetrical natural mode oscillations of the free surface are observed. At nozzle depths larger than 0.1 m, long-term self-sustained asymmetric jet oscillations are present in the cavity. Depending on the inlet velocity, the free surface can be essentially flat or oscillating, with or without bubble entrainment. The different free surface patterns have been summarized in a flow regime map.

The free surface dynamics have been linked to the sub-surface flow field through time-resolved PIV measurements. In the case of self-sustained free surface oscillations, the jets from the bifurcated nozzle oscillate in anti-phase with the same oscillation frequency as the free surface. The oscillations are caused by an interplay of the four recirculation cells in the cavity. At any given time, two strong and two weak recirculation cells are present. The cells interact through an imbalance between momentum and pressure gradient. A cross flow through the gaps between the nozzle and the front and back walls is a requisite for the self-sustained oscillations to exist.

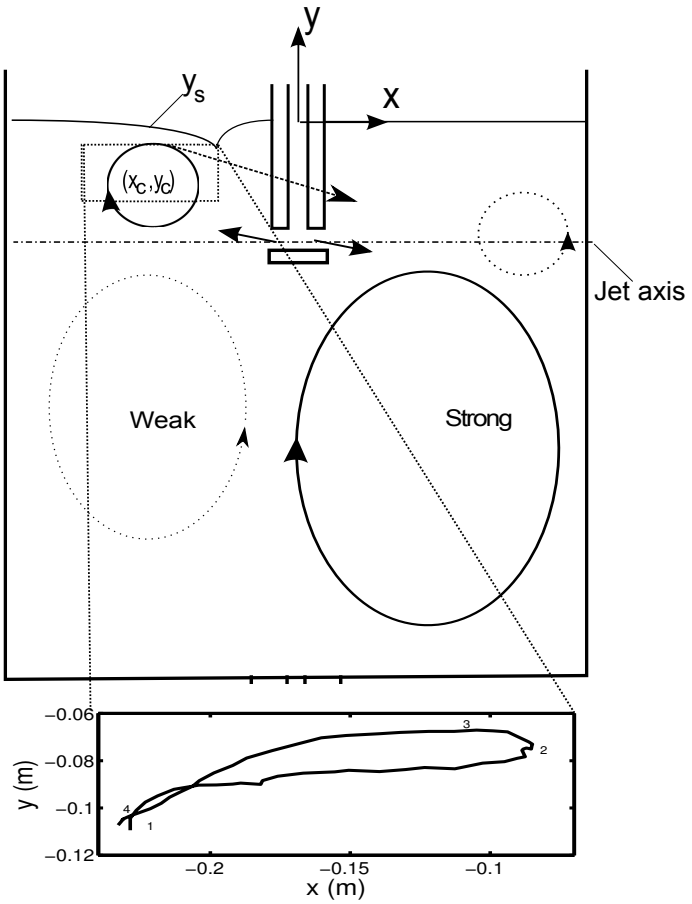

Figure 2.14: *Top*: Schematic representation of the recirculation zones in the cavity. Strong recirculation zones are depicted in the left top and in the right bottom, weak recirculation zones are depicted in the right top and in the left bottom. The position of the center of the recirculation zone in the left top is denoted by (x_c, y_c). High momentum fluid can shoot through the gaps between the inlet channel and the front and back walls, as indicated by the arrow from the recirculation zone over the inlet channel. *Bottom*: Position of the center of the recirculation zone, averaged over three oscillation periods. The recirculation zone center starts at 1, where the jet angle θ has a minimum. It grows to 2, where x_c and θ have a maximum. y_c grows until point 3. Between point 2 and 3 high momentum fluid shoots through the gaps between the inlet channel and the front and back walls. Then θ decreases to a minimum in point 4, where also x_c and y_c have a minimum.

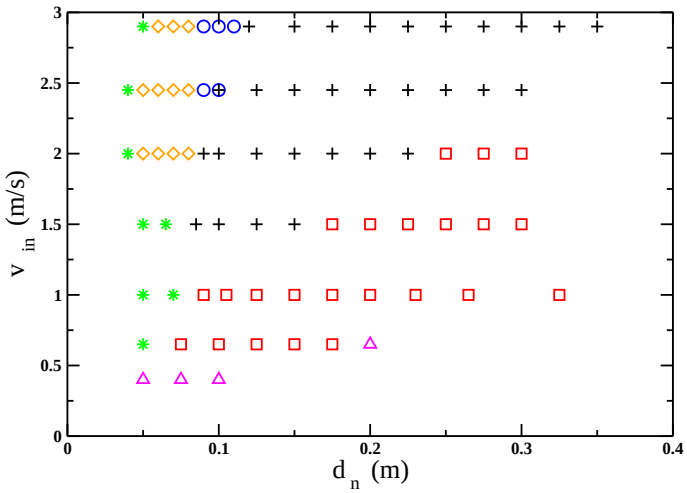

Figure 2.15: Flow regime map for the cavity with a bifurcated nozzle. * Regime I: Irregular pattern. ◇ Regime IIa: First natural mode. ◯ Regime IIb: Second natural mode. □ Regime IIIa: Self-sustained jet oscillations without bubble entrainment. + Regime IIIb: Self-sustained jet oscillations with bubble entrainment. △ Regime IIIc: Self-sustained jet oscillations without free surface elevation. The map is constructed by choosing a certain inlet velocity and changing the nozzle depth. The time between each measurement is such that the free surface is free of movement at the start of each subsequent measurement.

Chapter 3

Aspect ratio effects on fluid flow fluctuations in thin rectangular cavities[1]

The flow from a submerged bifurcated nozzle into rectangular liquid filled cavities with width-to-thickness ratios W/T = 6.5, 11 and 18 has been studied using free surface visualization and particle tracking. When $W/T = 11$ and when W/T = 18, self-sustained oscillations of the submerged jets and the free surface are present. When $W/T = 6.5$ the self-sustained oscillations are no longer present, but oscillations with the frequency of gravity waves occur.

We propose a critical value of W/T above which self-sustained jet oscillations occur, based on the spreading angle of turbulent jets. When W/T is larger than this critical value, the shear layers of the jet reach the front and back wall of the cavity before the jet can impinge the side wall, resulting in semi two-dimensional flow in the plane between the front and the back wall. Two dimensional recirculation zones form alongside the jet leading to the jet oscillations. When W/T is smaller than this critical value, the jet can develop like a free turbulent jet up to an impingement point at the narrow side wall. When the jet impinges the side wall, flow in the directions parallel and perpendicular to the front and back walls is possible, resulting in complex three dimensional flow patterns. The critical value for W/T, based on the known 12° spreading angle of turbulent jets is W/T = 10, which is in good agreement with the experimental results.

[1]Published in Metallurgical and Materials Transactions B, 2014

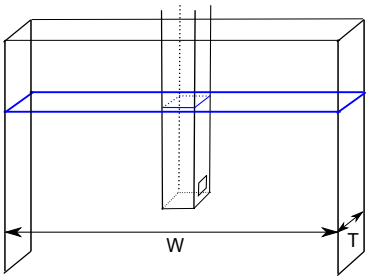

Figure 3.1: Schematics of the top of the continuous casting mould with width W and thickness T. In the middle a submerged bifurcated nozzle is depicted from which liquid flows into the mould.

3.1 Introduction

In continuous steel casting, liquid steel flows through a submerged nozzle into a mold. Figure 3.1 shows schematics of the top of the continuous casting mold. In the center a submerged nozzle is present, and W and T indicate the width and the thickness of the mold, respectively. The submerged nozzle is of the bifurcated type, expelling two (nearly) horizontal jets in opposite directions. Configurations encountered in continuous casting, based on the width-to-thickness ratio (W/T) of the cavity, are billet casting ($W/T \approx 1$), slab casting ($4 < W/T < 10$) and thin slab casting ($W/T > 15$). A slag layer is present on top of the liquid steel to prevent oxidation of the steel and to provide thermal insulation. Flow instabilities and resulting instabilities of the steel/slag interface can have a large influence on the entrainment of slag, which has a detrimental impact on the steel quality.

In lab experiments, the continuous casting process is often modeled using water, with a free air/water interface, as a working fluid (e.g. Honeyands and Herbertson (1995), Torres-Alonso et al. (2010b), Torres-Alonso et al. (2007)). The suitability of using scaled cold water models in the study of continuous casting was discussed by Chaudhary et al. (2009). The main advantage of using water is that it is transparent, so optical experimental techniques like laser Doppler anemometry (LDA), particle image velocimetry (PIV) and particle tracking velocimetry (PTV) can be used. The kinematic viscosity of water and liquid steel are approximately the same (within 20 %, Yuan et al. (2004)), so Reynolds similarity is achieved when a near full scale replica of a caster mold is employed in the experiments.

From studies of water flowing from submerged bifurcated nozzles into rectangular cavities, different kinds of instabilities of the free surface have

been recognized, resulting in an incomplete picture of the nature of flow instabilities in these configurations:

Honeyands and Herbertson (1995) reported self-sustained oscillations with a frequency of 0.2 Hz in a cavity with $W/T = 25$. On top of that they found a less pronounced natural mode oscillation of 0.7 Hz. Torres-Alonso et al. (2007) report a stable free surface profile with a periodic distortion of this stable profile with a frequency of 0.01 Hz in a cavity with $W/T = 25$. Jeon et al. (2010) report 0.8 Hz oscillations in the natural mode for a cavity with $W/T = 13.5$. In our previous study of flow from a bifurcated nozzle into a rectangular cavity with $W/T = 18$, a flow regime map was reported with three different flow regimes depending on the nozzle depth and the inlet velocity (Kalter et al. 2013). One of the flow regimes was a self-sustained oscillation of the two jets emerging from the bifurcated nozzle. The self-sustained jet oscillation frequency is reflected in a specific frequency of the free surface fluctuations around 0.1 Hz. Such self-sustained oscillations are known to occur when the jet shear layer is bounded by recirculation zones that are present in confined geometries (Rockwell 1983, Rockwell and Naudascher 1979).

In contrast to the above studies, Lawson and Davidson (2002) reported no specific frequency of the jet oscillation or the free surface fluctuation in a cavity with $W/T = 6.2$.

In Kalter et al. (2013) we suggested that the difference in flow behavior observed in various studies was due to a difference in configuration of the cavities. The flow behavior in thin ($W/T > 15$) cavities is more or less two-dimensional, leading to a structured oscillatory flow pattern, whereas the flow behavior in thick ($W/T < 10$) cavities is more three dimensional, leading to a more unstructured and complex flow pattern in the cavity. These conclusions seem to be supported by results from Real-Ramirez and Gonzalez-Trejo (2011) who reported results from numerical simulations of cavities with width-to-thickness ratios W/T = 3 and W/T = 10.

In the present work, we present a model (based on the spreading angle of turbulent jets) to predict a critical value for W/T, above which self-sustained jet oscillations are present. The model is validated with results from measurements performed in liquid filled cavities with inflow from a bifurcated nozzle and with a free air/water interface. The width-to-thickness ratios of the cavities used in this study are $W/T = 6.5$, $W/T = 11$ and $W/T = 18$. The free surface dynamics have been studied using high speed imaging of the capillary line of the free surface at the front wall of the cavity. In the case of $W/T = 6.5$ and $W/T = 18$ the sub surface flow behavior was investigated using particle tracking.

3.2 Physical modeling

3.2.1 Experimental set up

The experiments are conducted in two rectangular glass cavities, schematically shown in figure 3.2. The inner dimensions of the cavities are $H \times W \times T$ = water level height $\times$ cavity width $\times$ cavity thickness = 0.7 $\times$ 0.65 $\times$ 0.035 m^3 (W/T = 18) and 0.7 $\times$ 0.65 $\times$ 0.1 m^3 (W/T = 6.5), respectively. The thickness of the latter cavity can be reduced to T = 0.06 m by means of a perspex insert of 0.04 m in thickness, leading to W/T = 11.

Water is injected into the cavities through a vertical, submerged nozzle of 0.4 m length, located at the center of the cavity. The inner cross sectional dimensions of the nozzle are $d \times d$ = 0.014 $\times$ 0.014 m^2 and the outer dimensions are 0.02 $\times$ 0.02 m^2. The average flow velocity in the nozzle is $2 \times v_{in}$. The nozzle is closed at the end, but has two square outflow openings of $d \times d$ = 0.014 $\times$ 0.014 m^2 in opposite sidewalls near the end of the nozzle, as shown in the insert image in figure 3.2. Water emerges in the direction of the sidewalls of the cavity from each of these two openings, with an average velocity v_{in}. The end of the nozzle is at a depth $d_n = 0.1$ m below the equilibrium free surface level.

Through two 0.04 $\times$ T m^2 rectangular holes near the center of the bottom of the cavity, water is pumped out of the cavity into an external flow circuit. The water is recirculated, maintaining a constant average free surface position. The maximum bulk inlet velocity is v_{in} = 4.3 m/s corresponding to a maximum jet Reynolds number, based on d and v_{in} of Re = 6.0 $\times$ 10^4.

An orthogonal coordinate system is defined with its origin located at the intersection point of the equilibrium position of the free liquid surface and the axis of the nozzle. The x-axis is parallel to the equilibrium free liquid surface, and the y-axis is in the upward vertical direction. The z = 0 plane is the mid-plane of the cavity, located between the two broad walls. The free surface elevation, relative to $y = 0$, is denoted by η.

3.2.2 Measurement methods

Free surface tracking

Images of the capillary line at the front wall of the cavity are used for the tracking of the free surface location. Since the thickness T of the cavity is small compared to the width W, it is assumed that the position of the capillary line gives a good representation of the location of the free surface. A Photron SA1 high-speed camera is used to capture 20400 images of the free surface at a frame rate of 50 frames per second and with a resolution of 512 $\times$ 1024 pixels.

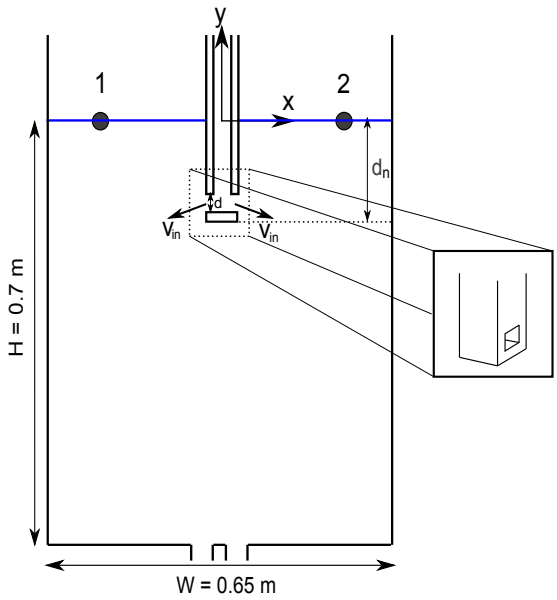

Figure 3.2: Schematic of the experimental flow configuration. The inner dimensions of the cavity are $H \times W \times T$. H and W are kept constant at H = 0.7 m and W = 0.65 m, respectively. The thickness T can be set to 0.035 m, 0.06 m and 0.1 m. Water flows into the cavity through a bifurcated nozzle with inner cross sectional dimensions $d \times d$ = 0.014 $\times$ 0.014 m^2 and outer dimensions of 0.02 $\times$ 0.02 m^2. The nozzle is submerged to a depth d_n = 0.1 m. Water exits the nozzle through two square exit holes $d \times d$ = 0.014 $\times$ 0.014 m^2 in opposite side walls of the nozzle, as schematically shown in the zoomed in image. The outflow is through two holes of 0.04 $\times$ T m^2 near the center of the bottom of the cavity. The two black dots at $x = \pm$ 0.175 m are monitoring points for measurements of the free surface elevation.

The spatial resolution is 0.63 mm/pixel. Background illumination is provided using an LED panel, resulting in a uniformly illuminated field of view.

Figure 3.3 shows an original image of the instantaneous free surface, and the detected free surface elevation. The analysis of the images is carried out in Matlab, using a steepest gradient detection method that determines the upper and lower edge of the free surface. The mean of the upper and lower position of the maximum gradient is used as the position of the free surface. The accuracy in the free surface elevation is 0.3 mm.

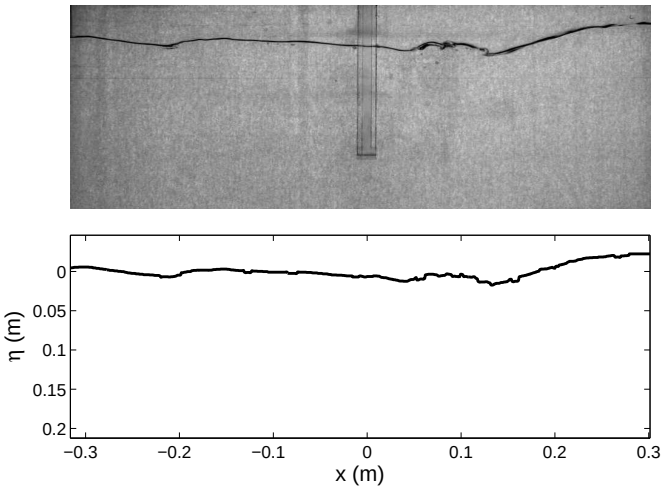

Figure 3.3: *Top*: Image of the instantaneous free surface with W/T = 18, v_{in} = 2 m/s and d_n = 0.1 m. *Bottom*: Detected free surface position.

Particle tracking

Images of neutrally buoyant opaque particles (Cospheric violet polyethylene microspheres,$\rho = 1.0$ kg/m^3, 0.85 - 1 mm in diameter) suspended in the flow are recorded, again using the Photron SA1 camera with back light provided by an LED-panel. The recorded images show the sub-surface for -0.3 m $< y < 0$ m. Image recording times vary between 100 and 200 seconds, the recording rate is 125 frames per second and the shutter time of the camera is $1/500$ s. During the recording time, every five seconds a group of approximately ten particles was inserted into the nozzle. Measurements are conducted with a low particle density to capture individual particle traces in the top region of the cavity.

The particle tracking algorithm introduced by Crocker and Grier (1996) is used to determine particle trajectories. The algorithm combines the positions of the recorded particle during subsequent time steps n and $n + 1$. Particles detected at time step $n+1$ within a distance of 12 pixels (0.8 cm) from a particle in frame n are linked, to form a trajectory. This means that particles with a maximum velocity of 1 m/s can be tracked. The particle tracking results that are presented in this article are for flows with an inlet velocity of v_{in} = 0.7 m/s, which is the maximum velocity in the measurement volume. When a suitable particle is detected, the process is repeated with the new particle location

in time step $n + 2$. If multiple particles are detected within the maximum displacement, the nearest neighbor method is applied to link particles in the subsequent time steps. Pathlines with a detection time longer than 125 frames (1 s) are regarded as valid pathlines.

3.3 Free jet vs. confined jet behavior: A model

Based on the apparent contradictory observations of the free surface instabilities in rectangular cavities, with water flowing in from a submerged bifurcated nozzle, reported in literature (Honeyands and Herbertson 1995, Jeon et al. 2010, Kalter et al. 2013, Lawson and Davidson 2002, Real-Ramirez and Gonzalez-Trejo 2011, Torres-Alonso et al. 2007) we conclude that the flow behavior in cavities with flow from a submerged bifurcated nozzle may vary depending on the width to thickness ratio (W/T) of the cavity. In this section we present a simple model based on the spreading angle of a turbulent jet, with which the flow behavior in the cavity can be predicted. Figure 3.4 depicts schematics of the top view of the cavity with the nozzle placed in the center. The spreading angle of 12° (Pope (2000)) of the two free turbulent jets emerging from opposite sides of the bifurcated nozzle is depicted by the dashed lines. When T = 0.035 m (W/T = 18) and when T = 0.06 m (W/T = 11), the edges of the jet reach the front and back walls before they reach the side walls. Because the jet completely fills the space between the front and back walls, the fluid is confined and after the subsequent impingement on the side walls it can only move in the y-direction, causing a semi two-dimensional movement of the fluid. This confined movement leads to more or less two-dimensional recirculating structures alongside the jet, as reported in Kalter et al. (2013). When the jets impinge the side walls before the shear layers of the jets reach the front and back walls (as is the case when W/T = 6.5) the jet spreading at the point of impingement can be in the y and z-direction. This results in a flow structure which behaves in a more three dimensional way.

Taking into account the spreading angle of a turbulent jet of 12° (Pope 2000) it is found that the critical value for the width to thickness ratio is $W/T = (\tan(\theta/2))^{-1} = (\tan(6°))^{-1} \approx 10$. When $W/T > 10$, a structured semi two-dimensional flow behavior is expected and when $W/T < 10$ an unstructured flow behavior is expected with complex three dimensional trajectories in the flow.

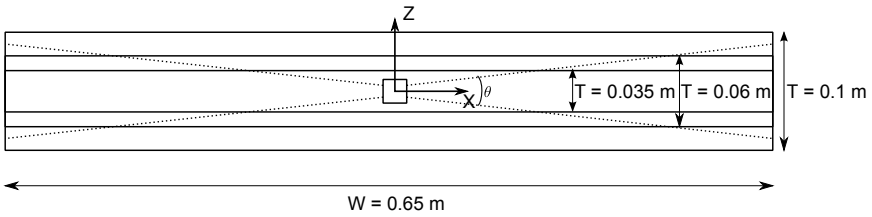

Figure 3.4: Schematics of the top view of the cavity with varying thickness T. The square in the center depicts the bifurcated nozzle. The jet spreading angles for free jets emerging from the nozzle are depicted by the dashed lines. It is seen that the shear layers of the jet reach the broad walls before the jets impinge the side walls when T = 0.035 m and T = 0.06 m. When T is 0.1 m, the jets impinge the side walls before the shear layers of the jets reach the broad walls.

3.4 Free jet vs. confined jet behavior: Experimental verification

3.4.1 Free surface behavior

Mean free surface profiles

Time-averaged free surface profiles are calculated from instantaneous free surface profiles by calculating the average y-position of the free surface at every x-position during the time of the measurement. Figures 3.5 (left) show the time-averaged free surface profiles for the different values of W/T and with inlet velocities of $v_{in} = 1.4$ m/s, $v_{in} = 2.1$ m/s and $v_{in} = 2.8$ m/s (corresponding to Re$_{jet}$ = 2×10^4, Re$_{jet}$ = 3×10^4, and Re$_{jet}$ = 4×10^4, respectively). It is seen that the mean free surface profiles are symmetric around the nozzle position. Minima in the free surface profile are located at x = ±0.2 m and maxima are located at the side walls. The mean wave amplitude, defined as $A = \eta_{max} - \eta_{min}$, grows with increasing inlet velocity. The mean wave amplitudes for W/T = 11 and W/T = 18 are more or less the same ($A = 0.008$ m when $v_{in} = 1.4$ m/s), but the mean wave amplitude for W/T = 6.5 is significantly smaller ($A = 0.002$ m when $v_{in} = 1.4$ m/s).

Figures 3.5 (right) show the standard deviations σ of the mean free surface elevation at every x-position. In the cavities with W/T = 18 and W/T = 11, the standard deviation of the free surface position shows peaks at the locations of the local minima in the mean free surface around x = ±0.2 m, indicating large fluctuations of the free surface at these locations. The standard deviation profile for W/T = 6.5 is more or less flat, indicating that the free surface fluctuations are evenly spread over the width of the cavity. It is observed

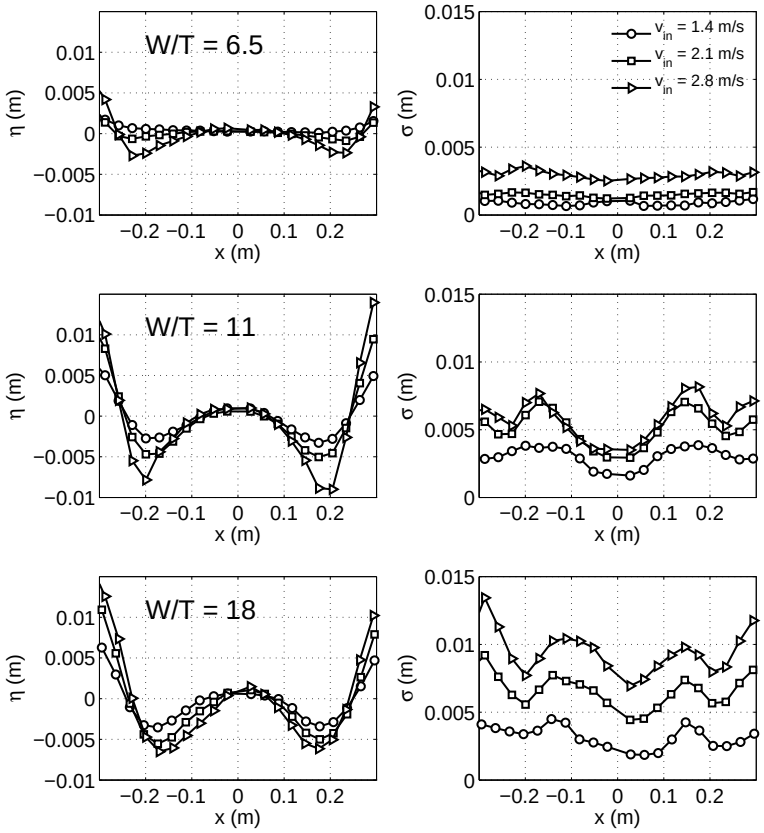

Figure 3.5: Left: Time averaged free surface profiles η for W/T = 6.5, W/T = 11 and W/T = 18. Right: Standard deviations σ of the time averaged free surface profiles for W/T = 6.5, W/T = 11 and W/T = 18. The symbols indicate: $\circ$ v_{in} = 1.4 m/s, $\square$ v_{in} = 2.1 m/s and $\triangleright$ v_{in} = 2.8 m/s.

that the magnitude of the standard deviation grows with inlet velocity, this is due to the larger amount of energy injected into the cavity, leading to more fluctuations. It is also observed that the values of the standard deviation grow with increasing W/T, indicating that larger fluctuations occur when the amount of fluid in the cavity is lower.

Transient free surface profiles

The results for the standard deviation profiles of the free surface fluctuations suggest qualitatively different flow behavior for W/T = 6.5 on one side and W/T = 11 and 18 on the other side. This section focuses on the transient free surface behavior for varying W/T. Figure 3.6 shows the transient profiles of the free surface in the cavity for W/T = 6.5, W/T = 11 and W/T = 18. Time is on the horizontal axis, the x-coordinate along the width of the cavity is on the vertical axis. At every time instant, the instantaneous free surface elevation profile along the width of the cavity is depicted by a vertical line of varying color, a dark tone represents a low surface elevation, and a light tone represents a high surface elevation.

Asymmetric oscillating patterns with oscillation periods of 8 and 11 seconds are found for W/T = 18 and W/T = 11, respectively. This suggests that in both cases the slow self-sustained oscillations reported in Kalter et al. (2013) play a major role. In the case with W/T = 6.5, an oscillating pattern is visible with an oscillation period of 1 second. Also the amplitude differs significantly from the amplitudes seen in the cases with higher W/T.

Frequency plots at the monitoring points

Figure 3.7 shows power spectra, calculated from time series of the free surface elevations at monitoring point 1 (indicated in figure 3.2) for $v_{in} = 1.4$m/s (Re$_j et = 2 \times 10^4$), $v_{in} = 2.1$m/s (Re$_j et = 3 \times 10^4$), and $v_{in} = 2.8$m/s (Re$_j et = 4 \times 10^4$). For W/T = 18 and W/T = 11 clear peaks are present at a frequency $f = 0.12$ Hz and $f = 0.09$ Hz, respectively. In the case of W/T = 18 a second harmonic is found at $f = 0.25$ Hz. These frequencies correspond well to the oscillation periods visualized in figure 3.6.

For $W/T = 6.5$ the single dominant frequency around $f = 0.1$ Hz is no longer present. Like in Lawson and Davidson (2002) many low frequency peaks are present below $f = 0.2$ Hz. In addition, a higher frequency peak is present at f = 1.10 Hz, corresponding to free surface fluctuations with a frequency in the gravity wave regime (Kalter et al. 2013, Lamb 1932),

$$f = \sqrt{\frac{g}{2\pi\lambda}} = \sqrt{\frac{g}{4\pi W}}, \tag{3.1}$$

where λ is the wave length of the gravity wave, which is twice the width of the cavity, $\lambda = 2W$. Higher order peaks are found at $f = 1.54$ Hz and at $f = 1.82$ Hz corresponding gravity waves with $\lambda = W$ and with $\lambda = 2/3W$, respectively. Note that the vertical scale of the power spectrum for W/T = 6.5 is much smaller than that for W/T = 18 and W/T = 11, indicating that the

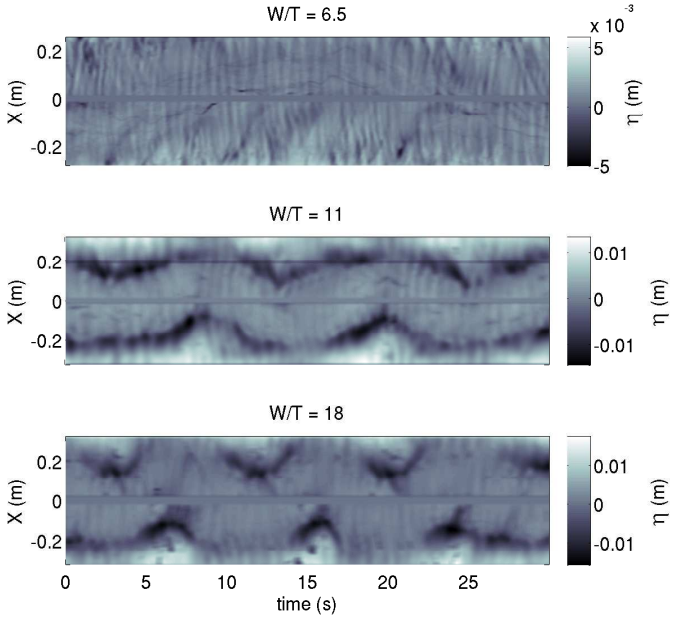

Figure 3.6: Transient profiles of the free surface position. On the vertical axis the x-position is depicted and on the horizontal axis the time is depicted. The graytone in the plot indicates the free surface elevation η. The inlet velocity is v_{in} = 1.4 m/s ($Re = 2 \times 10^4$) *Top*: W/T = 6.5. *Middle*: W/T = 11. *Bottom*: W/T = 18. Note that the colorbar for W/T = 6.5 has a different scale compared to the colorbars for W/T = 11 and W/T = 18.

gravity wave oscillations are much less dominant in the flow behavior than the self sustained oscillations.

3.4.2 Sub surface flow pattern

Particle trajectories

From the particle tracking measurements, trajectories of particles in the top of the cavities with W/T = 18 and W/T = 6.5 are recorded. Figure 3.8a shows 200 pathlines in the cavity with W/T = 18 and figure 3.8b shows 200 pathlines in the cavity with W/T = 6.5. In both cases, the inlet velocity is v_{in} = 0.7 m/s ($Re = 10^4$). The observed flow patterns are qualitatively different:

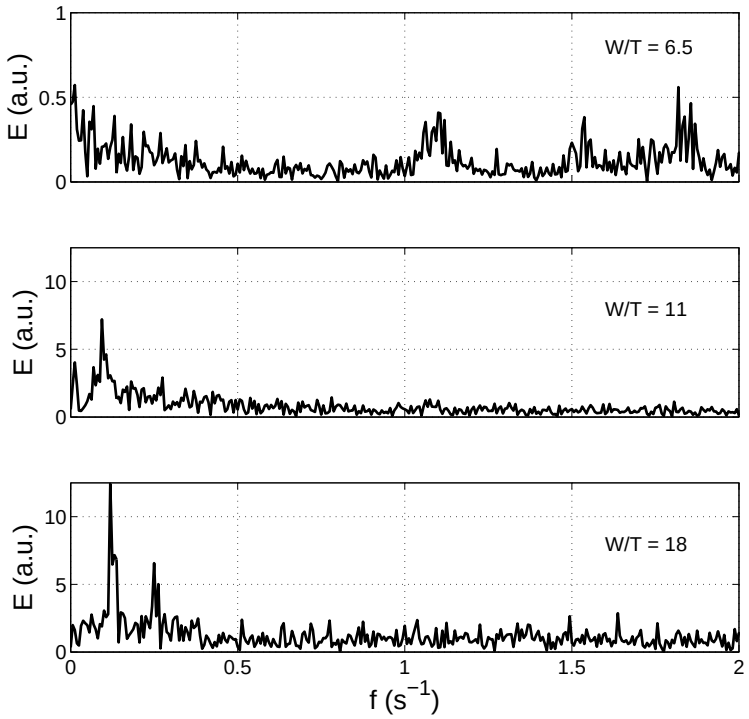

Figure 3.7: Power spectra from the time series of the free surface fluctuation at monitoring point 1 depicted in figure 3.2. The inlet velocity is v_{in} = 1.4 m/s ($Re = 2 \times 10^4$). *Top*: W/T = 6.5. *Middle*: W/T = 11. *Bottom*: W/T = 18. Note that the maximum values in the power spectrum for W/T = 6.5 are much lower than in the cases of W/T = 18 and W/T = 11.

For W/T = 18, recirculation cells are clearly visible at both sides of the nozzle. The variation in size and position of each of the upper recirculation cells, due to the oscillating jet, is also visible and comparable to that of the recirculation cells found from PIV measurements (Kalter et al. 2013). Most particles leave the field of view near the side walls at the bottom of the figure. Due to the recirculation cells downstream in the cavity, particles re-enter the field of view and may even re-enter the upper recirculation cells. The pathlines re-entering the field of view from the lower recirculation cells bend away from the jet towards the side walls with a horizontal velocity

component. Some particles in the upper recirculation cell at one side of the nozzle flow to the other side of the nozzle through the gaps between the nozzle and the front (and back) wall of the cavity. This phenomenon is known as cross flow (Gebert et al. (1998), Kalter et al. (2013)). The spreading angle of the jet is around 12° up to roughly 10 jet diameters from the nozzle ($|x| < 0.1$m). This equals the known spreading rate of a free turbulent jet (Pope 2000). When $|x| > 0.1$m the spreading rate increases due to the confinement of the jet between the front and the back wall and due to the oscillation of the jet. The spreading rate of 12° is indicated in figure 3.8a by the dashed lines, the deviation from the spreading rate is indicated by the curved dashed lines.

For W/T = 6.5, the pathlines show a constant jet spreading rate of 12° up to the impingement point of the jet at the side wall of the cavity at $y = -0.2$ m. This is indicated in figure 3.8b in the left half, by the dashed lines originating at the nozzle position. The constant spreading rate indicates free jet behavior in the entire width of the cavity. After impingement at the side walls, the pathlines do not form clear upper recirculation cells but follow a rather random path through the cavity. Pathlines re-entering the field of view from below reach the bottom of the nozzle by moving in the vertical direction before being accelerated by the jet in the horizontal direction.

The results from the PTV measurements only show the components of the pathlines in the x and y direction, since only a two-dimensional projection of the path lines could be recorded. Three dimensional path lines from CFD simulations in cavities with W/T = 10 and W/T = 3 have been reported by Real-Ramirez and Gonzalez-Trejo (2011). Especially in the case of W/T = 3 complex non-structured three dimensional trajectories were reported, but in the case of W/T = 10 the velocity component in the z-direction seems to be small. The present W/T = 6.5 case is in between the cases described by Real-Ramirez and Gonzalez-Trejo (2011). Since the jet seems to behave as a free jet throughout the cavity width, also significant velocity components in the z-direction are expected which can not be captured in the two-dimensional representation of the pathlines in the present PTV measurements.

3.5 Conclusions

A model was proposed to predict the presence of low frequency self-sustained jet oscillations in rectangular cavities with flow from a submerged bifurcated nozzle. The predictions of the model are based on the known spreading rate of turbulent jets of 12°. When $W/T > 10$, the shear layers of the jets reach the front and the back walls of the cavity before the jets impinge on the side walls. This leads to more or less two-dimensional recirculation zones alongside the

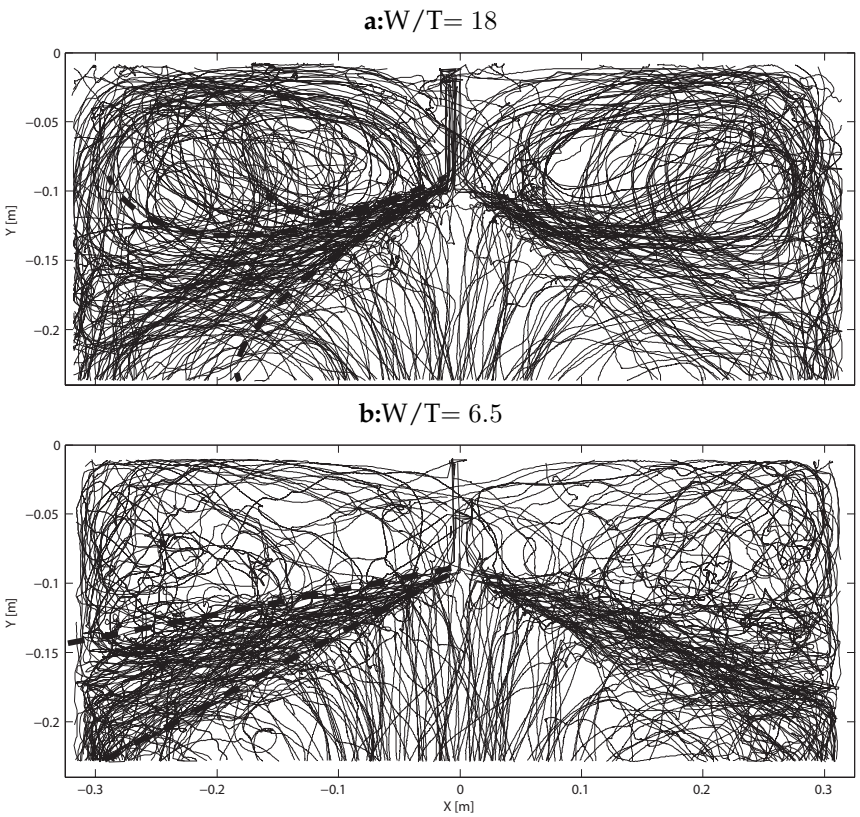

Figure 3.8: 200 pathlines obtained from PTV measurements for **a:**W/T = 18 and **b:**W/T = 6.5. The inlet velocity v_{in} = 0.7 m/s (*Re* = 1.0 $\times 10^4$). The dashed lines in the left half of the two images indicate the 12° spreading angle of the jet. In the top image the jet spreading diverges from 12° when $|x| > 0.1$ m, indicated by the curved dashed lines.

jet. These recirculation zones lead to self-sustained jet oscillations, due to confined flow behavior. When $W/T < 10$, the jets impinge the narrow side wall before their shear layers reach the front and the back walls, leading to complex three dimensional flow behavior.

Measurement results in rectangular cavities with W/T = 6.5, W/T = 11 and W/T = 18 have been presented to verify the model. Measurements of the free surface fluctuations indicate an oscillation of the free surface with a frequency around 0.1 Hz when W/T = 18 and when W/T = 11, due to the self-sustained jet oscillations. For W/T = 6.5, this low frequency oscillation has disappeared,

but oscillations in the natural mode of the cavity with a frequency of 1.1 Hz are present. This means that the transition of fully three dimensional flow behavior to semi two-dimensional flow behavior in the cavity takes place when $6.5 < W/T < 11$, as was predicted by the model.

Chapter 4

Heat transfer in a continuous casting mould model[1]

Temperature distributions in a thin continuous casting mould model have been studied experimentally, using water as a working fluid. The mould model consists of two narrow walls and two broad walls. One of the broad walls of the mould model was cooled with cooling water of a fixed temperature. Inflow of two turbulent jets with a constant high temperature was from a bifurcated nozzle, submerged to a depth of 0.1 m below the air/water interface.

The temperature drop over the mould was measured as a function of the temperature difference between the liquid flowing into the mould and the cooling water temperature. From these measurements the overall heat transfer coefficient and heat transfer coefficient due to convection in the mould were calculated.

Temperature distributions at the cooled wall have been measured using thermochromic liquid crystal sheets, which have a specific color depending on the temperature. The shear layers of the two jets hit the cooled wall, leading to hot spot formation. The jets show a self-sustained oscillating behavior, leading to a non stationary temperature distribution at the cooled wall. Between the jets and the air/water interface, recirculation zones occur where the liquid cools down significantly, leading to large wall temperature differences in the mould.

[1]Published in proceedings of the ASME 2014 4th Joint US-European Fluids Engineering Summer Meeting

4.1 Introduction

In the process of continuous slab casting, liquid steel flows through a submerged entry nozzle into a mould. In thin slab casting, the width W of the mould is much larger than the thickness T, typically leading to width-to-thickness ratios larger than 15. Cooling is applied at the walls of the casting mould for solidification of the steel. In the process of continuous casting, complex flow behavior, free surface dynamics and heat transfer play an important role. Based on the similar kinematic viscosity of liquid steel and water, the flow and free surface dynamics are often studied in simplified experimental models using water as a working fluid e.g. Honeyands and Herbertson (1995), Torres-Alonso et al. (2007). For heat transfer studies, the similarity between water models and actual casters is hampered by the large difference in Prandtl number. The advantage of using water as a working fluid is that it is transparent, such that optical measurement techniques like dye visualization, laser Doppler anemometry (LDA), particle image velocimetry (PIV) and particle tracking velocimetry (PTV) can be employed. The validity of using water models for predictions in the actual casting process is under debate and was discussed in the work of Chaudhary et al. (2009). However, experimental results in water models are extremely usefull for validation of numerical models.

Seyedein and Hasan (1997) present CFD simulation results using a standard $k - \epsilon$ turbulence model, assuming a stationary flow in a W/T = 5 casting mould. In their model, also solidification effects are considered. The numerical results were compared with experimental results presented in an earlier publication Nakato et al. (1984). Results from transient CFD studies on the heat transfer in a W/T = 7.5 casting mould were presented by Zhao et al. (2005). They used a large eddy simulation technique to study the time-dependent behavior of the flow and heat transfer in the mould. For validation of the numerical results, the flow velocities were compared to velocity measurements from dye visualization experiments in a water model. The heat transfer results were compared to data which was acquired during actual plant operations. Especially the measurements in the plant are difficult to perform and they have a large uncertainty.

From the examples given above, it can be concluded that good experimental test cases for heat transfer and temperature distributions in models of the continuous casting mould are rare. In the present work we investigate experimentally the heat transfer characteristics and temperature distribution in a water model of a continuous casting mould with W/T = 18. The mould model was a 2:1 scaled down model of an actual thin slab casting mould. One of the broad walls of the mould is made of stainless steel, and

is cooled with cooling water at a fixed low temperature. The other walls are made of glass, to provide optical access. Water is used as a working fluid, such that the optical measurement technique of liquid crystal thermography (LCT) can be employed. In our previous work Kalter et al. (2013) the flow in an isothermal caster mould model with W/T = 18 was studied, employing the PIV measurement technique. The inflow of two jets into the mould was from a submerged bifurcated nozzle. It was found that low frequency, self-sustained asymmetric oscillations of the two jets occurred in this configuration for inlet velocities larger than $v_{in} \approx 0.5$m/s and for nozzle depths larger than $d_n \approx 0.1$m. These self-sustained oscillations are generally unwanted since they may lead to inclusions into the mould, leading to a degradation of the steel quality. It is expected that the self-sustained jet oscillations result in hot spots at the cooled wall. In the present work, measurements were performed with liquid crystal sheets attached to the cooled wall so that hot spots at the wall could be recorded using a color camera.

The objective of the present work is to provide insight in heat transfer characteristics in the casting mould, as well as to provide meaningfull qualitative and quantitative experimental data for validation of numerical models. Due to dynamic, kinematic and thermal differences between steel and water, the data from the experiments presented here can not be used directly for the prediction of processes in the actual continuous casting process.

4.2 Physical modeling

4.2.1 Experimental setup

Figure 4.1 shows schematics of the experimental setup. Experiments are conducted in a rectangular casting mould model, schematically shown in figure 4.1 (right). The inner dimensions of the mould model are 0.8 $\times$ 0.65 $\times$ 0.035 m^3 (= $H \times W \times T$ = height $\times$ width $\times$ thickness) which is a 2:1 scaling of a realistic thin slab casting mould. The mould is filled with tap water to a height h = 0.7 m.

Water is injected into the cavity through a vertical, submerged nozzle of 0.6 m length, inner dimensions $d \times d$ = 0.01 $\times$ 0.01 m^2 and outer dimensions 0.02 $\times$ 0.02 m^2. The average flow velocity in the nozzle is $2v_{in}$. The nozzle is closed at the end, but has two square outflow openings of $d \times d$ = 0.01 $\times$ 0.01 m^2 in opposite sidewalls near the end of the nozzle. Water emerges in the direction of the sidewalls of the cavity from each of these two openings, with an average velocity v_{in}. The end of the nozzle is at a nozzle submergence depth $d_n = 0.1$ m below the water surface at rest.

Through two 0.04 $\times$ 0.035 m^2 rectangular holes near the center of the

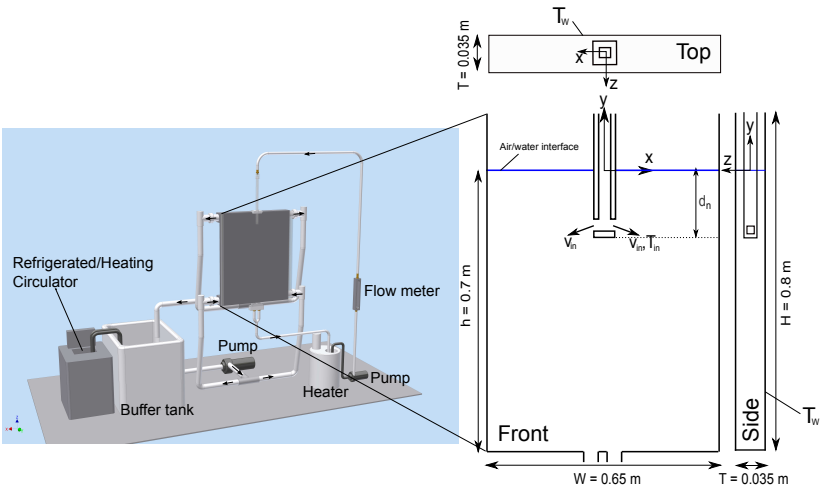

Figure 4.1: Schematics of the experimental setup. *Left:* On the left a refrigrating/heating recirculator is depicted which keeps water in the buffer tank at a constant temperature. This water is recirculated through a stainless steel cooling wall with a pump. *Right:* Zoomed in schematics of the mould model, the inner dimensions are $H \times W \times T = 0.8 \times 0.65 \times 0.035$ m^3. The back wall of the mould model consists of the stainless steel cooling wall and the other walls are made of glass. Water flows into the cavity through a bifurcated nozzle with inner dimensions $d \times d = 0.01 \times 0.01$ m^2 submerged to a depth d_n. The cavity is filled up to $h = 0.7$ m with water.

bottom of the mould, water is pumped out of the mould into an external flow circuit and back into the nozzle, maintaining a constant volume of water in the mould. The water flowing into the mould is kept at a constant inlet temperature T_{in} (within 0.1°C) by means of a thermostat bath and an immersion cooler in the external circuit. The temperatures at the inlet and outlet of the mould are monitored using Pt100 RTD sensors with an accuracy of 0.1°C. The inlet flow rate is controlled using a valve, and during the measurements the maximum flow rate was set to $\phi_v = 0.25\,\mathrm{l/s}$, corresponding to Reynolds numbers, based on d and v_{in} of Re = 1.25×10^4. This value of the Reynolds number is in the low range of Reynolds numbers encountered in the continuous casting process Najjar et al. (1995).

The mould consists of three walls made of glass. The fourth wall (one of the broad walls) consists of two stainless steel plates of two millimeters in thickness and separated by a gap of $d_{gap} = 2$ mm. Through this gap, cooling water flows with a constant temperature T_W (within 0.1°C). The cooling water is kept at a constant temperature using a Julabo FP51-SL ultra-low

refrigerated-heating circulator, shown on the left in figure 4.1. The cooling water is stored in a buffer tank and from this tank it is recirculated with a pump through the gap between the two stainless steel plates with a flow rate of 12 m^3/hr. This flow rate leads to a flow velocity of 2.4 m/s and a Reynolds number Re = 9.6×10^3 based on the hydraulic diameter $2 \times d_{gap}$. The water flow is from bottom to top, to prevent abrupt pressure changes.

For reference, in the mould an orthogonal coordinate system is defined with its origin located at the equilibrium position of the free liquid surface in the center of the cavity. The *x*-axis is parallel to the equilibrium free liquid surface and to the front wall of the cavity, and the *y*-axis is in the upward vertical direction. The cross sections of the experimental setup, shown in figure 4.1, are located at the x = 0, y = 0 and z = 0 planes.

4.2.2 Liquid crystal thermography

Thermochromic liquid crystal (TLC) sheets are attached to the cooled wall inside the cavity. They are used to quantify the temperature distribution in the mould at the position of the cooling wall. The TLC's reflect light with a specific wavelength, depending on their temperature. When going through a temperature trajectory, starting with a low temperature, the initially black sheets color to red, green and blue, before turning black again. The TLC sheets used in the present research have a colorplay between T = 25 °C (red) and T = 35 °C (blue) and they are manufactured by LCR Hallcrest. A thorough review of the use of TLC's was provided by Dabiri (2009). A Basler Pilot piA640-210gc color camera equipped with a Progressive Scan CCD chip with 648 × 488 pixels is used to collect images of the TLC's with a frame rate of 10 fps. Two TLC sheets with a usable surface area of 0.25 × 0.4 m^2 are used in this research and are attached to the top region of the cooled back wall of the mould, such that the influence of the jet dynamics on the heat transfer at the wall can be studied. The TLC sheets are covered with a polyester sheet, to prevent them from damage due to diffusion of water into the sheet.

The images from the color camera result in three values per pixel, for the red, blue and green component of the color. From these three values calibration is performed to find a relationship between the color and the temperature. Since the color-temperature relation is dependent on the measurement configuration, calibration was performed inside the actual experimental facility. Calibration of the TLC sheets was done using the RGB to HSI conversion Stasiek et al. (2006). The hue value is calculated as

$$H = \begin{cases} 90 - \tan^{-1}(\frac{F}{\sqrt{3}}) & , g > b, \\ 90 - \tan^{-1}(\frac{F}{\sqrt{3}}) + 180 & , g < b, \end{cases} \tag{4.1}$$

where

$$F = \frac{2r - g - b}{g - b}. \tag{4.2}$$

r, g and b are the color values for red, green and blue respectively. The hue-temperature calibration curve has to be calculated for every pixel position separately to account for local effects.

4.3 Results

4.3.1 Overall heat transfer

The temperatures at the inlet and outlet of the mould are registered using the Pt100 RTD probes. This was first done for a stainless steel cooling wall without the TLC sheets and without the coverage of a polyester sheet. The white symbols in figure 4.2 show the temperature drop over the cavity $\Delta T = T_{in} - T_{out}$ as a function of the temperature difference between the wall and the fluid flowing into the cavity $T_{in} - T_W$. Here T_W is the cooling water temperature which is kept constant at 22°C.

When TLC sheets are attached to the cooling wall, to visualize structures of the temperature distribution at this wall. The heat transfer characteristics change compared to the case with an uncovered stainless steel wall. To compare the global character of the two situations, again temperature drop measurements of the fluid in the cavity have been performed as a function of the difference between the applied wall temperature and the temperature of the fluid flowing into the cavity. The black symbols in figure 4.2 are the data points for the stainless steel wall covered with liquid crystal sheets and the protective polyester foil. It is observed that the temperature difference ΔT is smaller than without the liquid crystal sheets, which is expected, since the sheets add an extra heat resistance. We can calculate the total heat transfer coefficients h from the water in the mould to the cooling water in the cooled wall as

$$h = \frac{\rho c_p \phi_v}{A} \frac{T_{in} - T_{out}}{T_{in} - T_W}. \tag{4.3}$$

Figure 4.3 shows the total heat transfer coefficients as a function of the flow rate ϕ_v for the situations of the stainless steel wall with and without LC sheets attached. The contributions to the total heat transfer coefficient are the convective heat transfer coefficient of the cooling water to the stainless steel wall h_{cool}, the heat transfer coefficient of the stainless steel h_{ss}, the heat

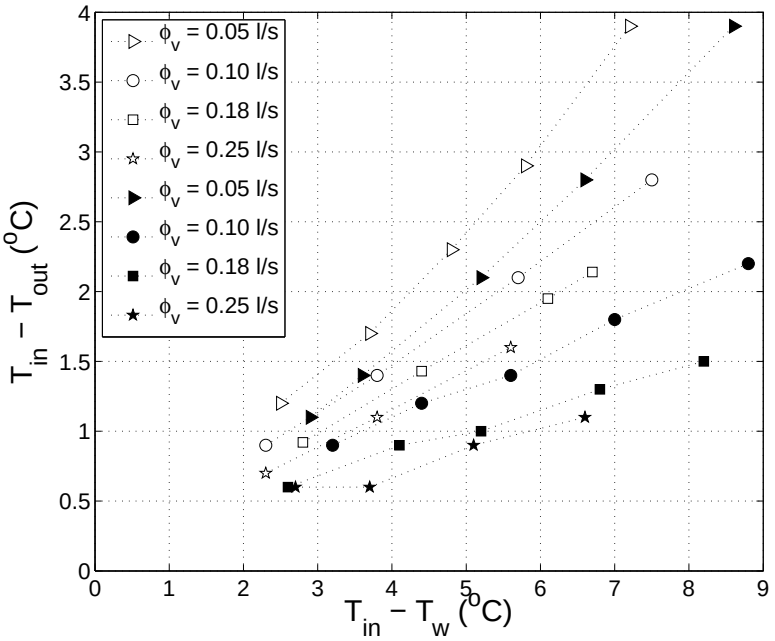

Figure 4.2: Temperature drop $\Delta T = T_{in} - T_{out}$ as a function of $T_{in} - T_W$. The cooling water temperature is kept constant at T_W = 22°C. The white symbols indicate the measurement results for the bare stainless steel cooling wall and the black symbols indicate the measurement results when the cooling wall is covered with the TLC sheets and the polyester foil.

transfer coefficient of the liquid crystal sheets and polyester foil h_{LC} and the convective heat transfer coefficient from the water inside the mould to the cooled wall h_{conv}. The total heat transfer coefficient h is calculated as

$$h = \left(\frac{1}{h_{cool}} + \frac{1}{h_{ss}} + \frac{1}{h_{LC}} + \frac{1}{h_{conv}} \right)^{-1} \tag{4.4a}$$

$$h = \left(\frac{1}{h_{cool}} + \frac{1}{h_{ss}} + \frac{1}{h_{conv}} \right)^{-1} \tag{4.4b}$$

for measurements with and without liquid crystal foil respectively. h_{conv} is the only parameter which depends on the flow rate into the mould.

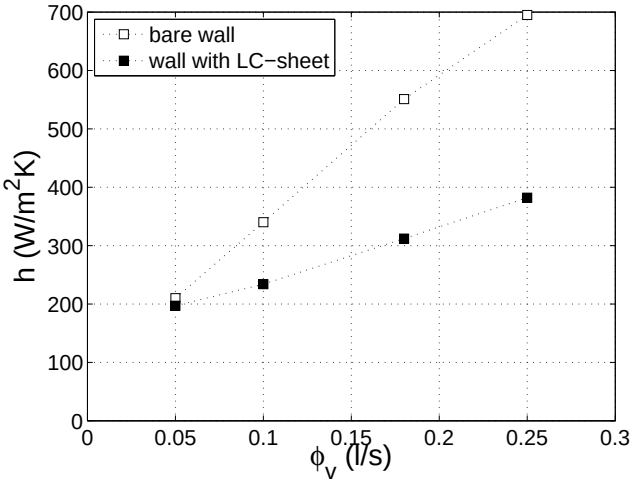

Figure 4.3: Calculated total heat transfer coefficients h (eq 4.3) as a function of the flow rate ϕ_v.

From equations 4.4 and measured values of the total heat transfer coefficient h, the heat transfer coefficient h_{conv} due to convection in the mould can be calculated once h_{ss}, h_{cool} and h_{LC} are known.

From estimated thicknesses and thermal conductivities of the stainless steel wall (λ_{ss} = 16 W/mK and d_{ss} = 2 mm) and the liquid crystal foil (λ_{LC} = 0.2 W/mK and d_{LC} = 0.3 mm) we estimate h_{ss} = 8 $\times$ 10^3 W/m^{2}K and h_{LC} = 8 $\times$ 10^2 W/m^{2}K. For h_{cool} we estimate Incropera and DeWitt (4th ed. 1996)

$$\mathrm{Nu} = \frac{2d_{gap}h_{cool}}{\lambda_{water}} = 0.027\mathrm{Re}^{0.8}\mathrm{Pr}^{0.33}, \tag{4.5}$$

with Re = 9.6$\times$$10^3$ as was indicated on page 4.2.1. This leads to h_{cool} = 1.2 $\times$ 10^4 W/m^{2}K. With the measured total heat transfer coefficients in figure 4.3 this leads to the convective heat transfer coefficients in figure 4.4. The convective heat transfer coefficient scales with the jet flow rate to the power 0.8.

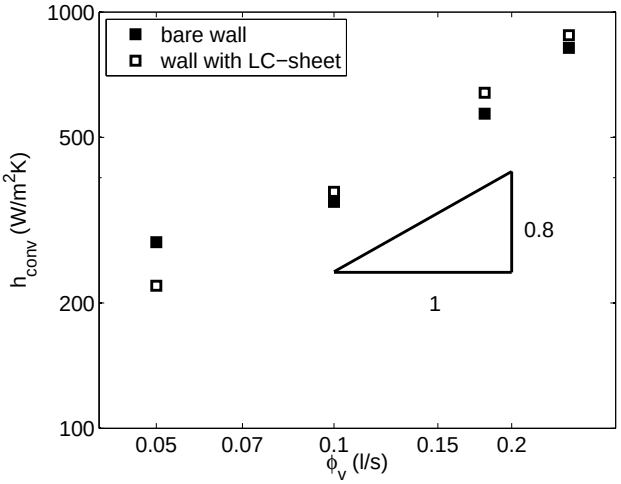

Figure 4.4: Log-log plot of the convective heat transfer coefficient h_{conv} as a function of the flow rate ϕ_v.

4.3.2 Qualitative description of the temperature distribution at the cooling wall

Figure 4.5 shows a snap shot of the color play of the usable area of the liquid crystal sheets attached to the cooling wall. The liquid crystal sheets are attached to the wall at the locations -0.4 m$< y <$ 0 m and -0.3 m $< x <$0.3 m and the usable area is -0.35 m$< y <$ -0.05 m and -0.27 m $< |x| <$0.025 m. The injected liquid is at a constant temperature of $T_{in} = 32°$C and the cooling water temperature is kept constant at $T_W = 25°$C. The structures of the shearing of the warm jets along the cooling wall is clearly visible. The shear layers of the jets hit the cooling wall at $x = \pm 0.03$m where a clear green spot is visible, indicating a high temperature. Following the jets towards the side walls, it is seen that the green zone expands due to the jet expansion and that the green color becomes a bit more dim, indicating a reduction in temperature. When the jets impinge on the side walls, they split into an upward moving part and a downward moving part and a recirculation zone is formed between the jet and the air/water interface. In the center of this recirculation zone a clear pink spot is visible, indicating that the wall temperature in the center of the recirculation zone is much lower than the wall temperature in the jet region. The recirculation zone center was not located at a fixed position. Due to the asymmetric jet oscillations (as previously reported Kalter et al.

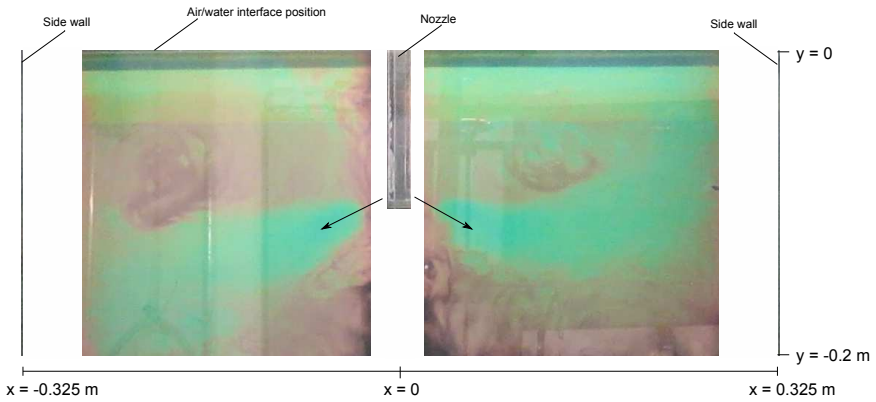

Figure 4.5: Snap shot of the color of the liquid crystal sheets due to the high temperature jets ($T_{in} = 32°$C) issuing from the nozzle and shearing along the low temperature wall ($T_W = 25°$C). The two arrows indicate the jet flow direction from the nozzle into the mould. The green color indicates a high wall temperature and the pink color indicates a low wall temperature. The impingement of the shear layers of the jets on the cooling wall is clearly seen and it is seen that the wall temperature is low in the recirculation zone between the jet and the air/water interface.

(2013)) the recirculation zones move in an asymmetric manner and so the low temperature zones also move in this asymmetric manner.

In continuous steel casting, the distinction can be made between thin and thick steel casting, which is expressed in the width to thickness ratio W/T. In thin slab casting, $W/T > 15$, while in thick slab casting, usually $W/T < 10$. The spreading angle of a turbulent jet is approximately 12^o Pope (2000), so in thin slab casting the shear layers of the jets hit the cooling wall rapidly after issuing from the nozzle, leading to the hot spot formation shown in figure 4.5. In thick slab casting the jets have much more space to develop such that the jet can actually develop freely until it impinges on the narrow side walls, preventing hot spot formation at the cooled wall completely. The prevention of the hot spot formation can lead to a more uniform cooling of the liquid steel, resulting in a more controlled solidification process and hence to a higher steel quality.

4.3.3 Quantitative description of the temperature distribution at the cooling wall

To quantitatively describe the temperature fluctuations at the cooled wall, a calibration of the color play of the liquid crystal sheets was performed. For

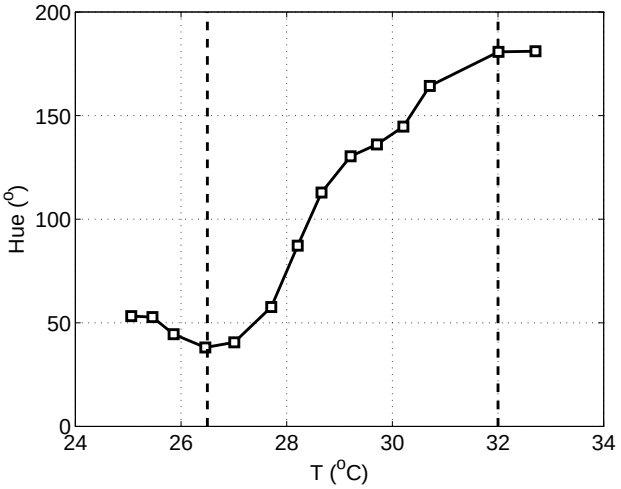

Figure 4.6: Example of the hue-temperature calibration curve at one pixel location in the field of view. The curve is monotonously growing when the temperature is larger than 26.5°C and lower than 32°C.

this, the cooling water was kept at a constant temperature, while the flow of water in the mould was shut down. After some time a constant temperature, equal to the cooling water temperature, was reached at the liquid crystal sheets and a series of ten pictures of the liquid crystal sheets was made with the color camera. Then the cooling water temperature was increased to a higher temperature and again images of the liquid crystal sheet were taken. With increasing temperature, the liquid crystal sheet changes color from red, through green to blue. The hue value (equation 4.1) is calculated at every pixel position from the average of the ten pictures for the different temperatures. A typical calibration curve for one pixel is shown in figure 4.6. It is seen that the hue increases monotoneously with temperature when the temperature is higher than 26.5°C and lower than 32°C. Below T = 26.5°C and above 32°C the hue value does not uniquely correspond to one value of the temperature.

Figure 4.7 shows the mean wall temperature distributions for flow rates of ϕ_v = 0.10 l/s, ϕ_v = 0.15 l/s and ϕ_v = 0.19 l/s. In all three cases a hot spot is observed at the location where the shear layer of the jet hits the wall ($x = -0.03$m and $y = -0.12$m). From the color distribution in the field of view it is seen that the average wall temperature is higher when the flow rate is the highest, in agreement with the earlier findings that h_{conv} increases with increasing flow rate from the jets.

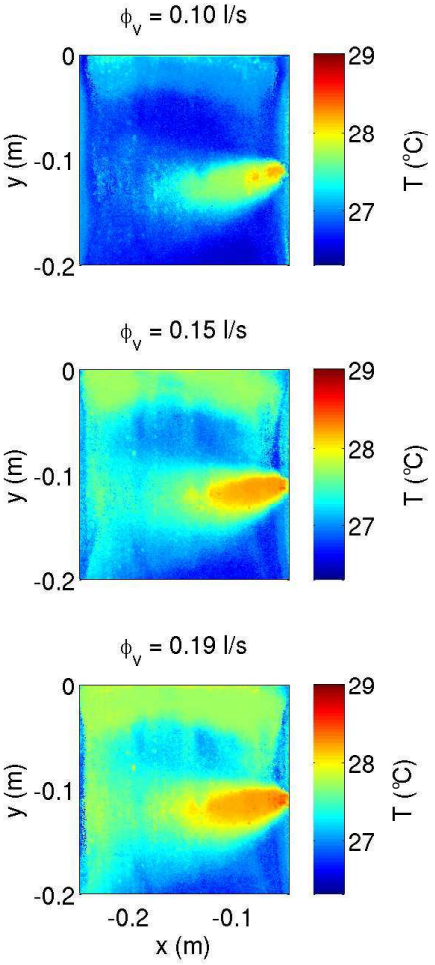

Figure 4.7: Mean temperature distribution at the cooled wall in the field of view for flow rates of ϕ_v = 0.10 l/s, ϕ_v = 0.15 l/s and ϕ_v = 0.19 l/s.

Figure 4.8 shows instantaneous wall temperature distributions for the case with a flow rate of ϕ_v = 0.19 l/s. These wall temperatures reflect the heat transfer from the hot jet to the cold wall and the mixing of the hot jet with the

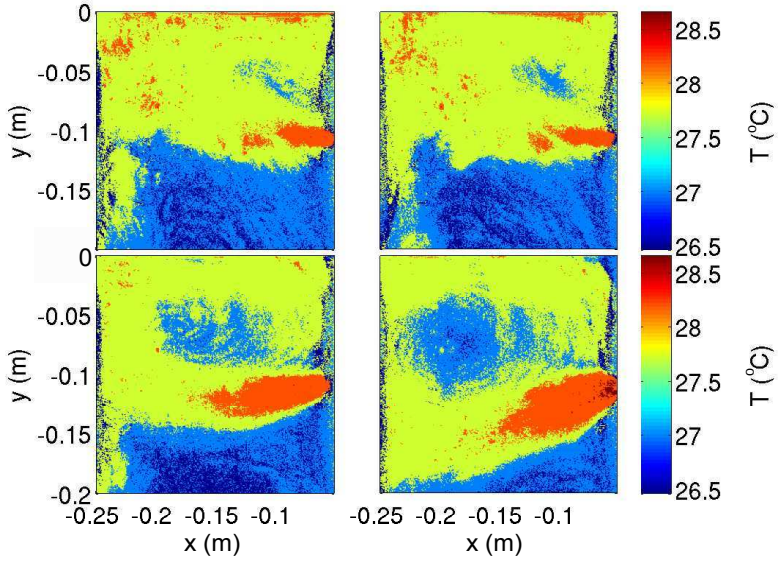

Figure 4.8: Cooling wall temperature distribution in the field of view for different stages of the jet oscillation. The time between the images is two seconds and the flow rate is ϕ_v = 0.19 l/s.

colder fluid in the mould. It is known from our previous work (Kalter et al. (2013)) that the jets oscillate in an asymmetric manner and the four images in figure 4.8 show half a jet oscillation in the region to the left of the nozzle. The time between the images is two seconds. A hot spot at the wall is seen in red at the location where the shear layers of the jet hit the cooled wall (x = -0.03 m, y = -0.12 m). The size of the hot spot is not constant, due to faster and slower mixing of the jet liquid. When the jet is directed upwards (as in the top two images) the liquid from the hot jet flows directly into the recirculation zone between the jet and the free surface, maintaining a high velocity and mixing quickly with the surrounding liquid as seen by the rapid temperature decrease from red to green. When the jet is in the downward direction as in the bottom two images, it spreads widely, leading to a deceleration of the liquid. This causes less mixing and hence the jet liquid can maintain a high temperature. Between the jet and the free surface a recirculation zone is present where the temperature is significantly lower than in the jet indicated by the blue regions around $x \approx$ -0.18m and $y \approx$ -0.07m. The liquid in the recirculation zone remains there for a relatively long time, giving it the opportunity to cool down

significantly.

4.4 Conclusions

Experiments have been performed in a thin continuous casting mould model ($W/T = 18$), using water as a working fluid. The water flows into the mould through a bifurcated nozzle which is submerged below the air/water interface. One of the broad walls was cooled with cooling water of a fixed temperature, lower than the temperature of the liquid flowing into the mould. Overall heat transfer measurements and measurements with thermochromic liquid crystal sheets attached to the cooled wall have been performed. The average convective heat transfer coefficient from the water in the mould to the cooled wall was found to increase with the jet flow rate to the power 0.8. Hot spot formation was observed at the location where the shear layers of the jet hit the cooled wall. Following the jet motion, the jet spreads and the jet liquid cools down. Between the jets and the air/water interface, recirculation zones occur in which the liquid movement slows down and the temperature of the liquid decreases significantly.

Time averaged temperature distributions at the cooled wall have been studied for flow rates of $\phi_v = 0.10$ l/s, $\phi_v = 0.15$ l/s and $\phi_v = 0.19$ l/s. In all three cases, a clear hot spot was visible at the point where the shear layers of the jet hit the cooled wall.

The jets issuing from the nozzle exhibit an oscillatory motion, which leads to large instantaneous wall temperature differences between the jet region and the region outside of the jet. The lowest wall temperature is found in the center of the recirculation zone between the jet and the air/water interface. This recirculation zone oscillates with the jet oscillation, leading to a periodic movement of the low temperature zone. This leads to transient behavior of the heat transfer from the liquid to the cooling wall and when modeling the continuous casting process this transient behavior needs to be taken into account.

Chapter 5

Effects of electromagnetic forcing on self-sustained jet oscillations[1]

The influence of electromagnetic forcing on self-sustained oscillations of a jet issuing from a submerged nozzle into a thin vertical cavity (width W much larger than thickness T) has been studied using particle image velocimetry. A permanent Lorentz force is produced by applying an electrical current across the width of the cavity in conjunction with a magnetic field from three permanent magnets across its thickness. As a working fluid a saline solution is used. The magnetic field is in the north-south-north configuration, such that the Lorentz force can be applied in an up-down-up configuration or in a down-up-down configuration by switching the direction of the electrical current.

A critical Stuart number N_c was found. For $N < N_c$, the jet oscillates with a constant Strouhal number St, independent of the Reynolds number Re. For $N > N_c$ and an oscillation enhancing up-down-up configuration of the Lorentz force, St grows with N as $St \propto \sqrt{N}$. In contrast, for $N > N_c$ and an oscillation suppressing down-up-down configuration of the Lorentz force, all jet oscillations are suppressed.

5.1 Introduction

Self-sustained flow oscillations are known to occur in confined geometries, when shear layers are bounded by recirculation zones Rockwell (1983),

[1]Published in Physics of Fluids **26**, 065101, 2014

Rockwell and Naudascher (1979). Flows in which self-sustained oscillations occur are (amongst others): jets issuing into a thin cavity Honeyands and Herbertson (1995), Kalter et al. (2013), Kolsek et al. (2007), Lawson and Davidson (2001), Mataoui and Schiestel (2009), Maurel et al. (1996), Molloy and Taylor (1969), the flow over backward facing steps Wee et al. (2004), Yokoyama et al. (2007) and flows over cavities Rockwell and Naudascher (1978), Rowley et al. (2002), Rowley and Williams (2006), Tam and Block (1978). The self-sustained oscillations have a much lower frequency than those produced by shear layer instabilities.

In the present work we focus on a single jet issuing from a submerged nozzle into a thin cavity. Honeyands and Herbertson Honeyands and Herbertson (1995) investigated this flow problem earlier and they reported a self-sustained oscillating behavior of the jet. Their results show that the interactions of the recirculation zones alongside the jet with the jet itself are of large importance for the mechanism leading to the self-sustained oscillation. An imbalance was found between the pressure force in the center of the recirculation zone and the inertial force in the jet. These two forces fluctuate with the same frequency as the frequency of the jet oscillation, but a phase difference with a specific delay time exists between the maxima in the pressure force and the inertial force. This delay time is essential in the mechanism behind the self repeating behavior of the jet oscillation. Influencing the formation of the recirculation zones changes the interaction between the recirculation zones and the jet, and hence the jet oscillation can be altered. To achieve this influence on the jet oscillation, we apply an electromagnetic forcing.

Electromagnetic forcing of flows can be introduced by applying an imposed electrical current in conjunction with a magnetic field. The use of this principle was reported in several publications, for instance to delay flow separations Crawford and Karniadakis (1997), Henoch and Stace (1995), to increase heat transfer Kenjereš (2008), Kenjereš et al. (2009) and to increase laminar mixing Kenjereš (2011), Rossi et al. (2012a;b). Electromagnetic actuators are used for the control of turbulent channel flow Berger et al. (2000), Spong et al. (2005), for the suppression of vortex shedding behind a cylinder Kim and Lee (2000), Zhang et al. (2010) and to prevent flow separation past an airfoil Cierpka et al. (2008), Weier et al. (2008; 2003).

The effect of electromagnetic forcing on self-sustained oscillations of a confined square jet issuing into a thin cavity is investigated experimentally using particle image velocimetry (PIV). A permanent Lorentz force is imposed on the fluid by an electrical current across the width of the cavity in conjunction with a permanent magnetic field perpendicular to the electrical current. A saline solution is used as a working fluid to increase the electrical

conductivity as compared to tap water. The electromagnetic forcing at the position of the recirculation zones alongside the jet is such that it can be in the same or in the opposite direction as the momentum of the liquid flowing in the recirculation zones. This leads to an increase or a decrease in the growth of the recirculation zones and hence to an enhancement or suppression of the jet oscillation.

The objective of the present research is to quantify the influence of the Lorentz force on self-sustained jet oscillations. We look for the presence of a critical value of the Stuart number, above which the flow dynamics are completely dominated by the Lorentz force.

5.2 Physical modeling

5.2.1 Experimental setup

The experiment is conducted in a vertical rectangular glass cavity, schematically shown in figure 5.1. The inner dimensions of the cavity are height H $\times$ width $W\times$ thickness T = 0.8 $\times$ 0.3 $\times$ 0.035 m^3 and it is filled to a height of h = 0.7 m. The working fluid is a solution of 10 wt% Na_2SO_4 in water. The density of the working fluid is ρ = 1.10 $\times 10^3$ kg/m^3, the kinematic viscosity is $\nu = 1.27 \times 10^{-6}$ m^2/s and the electrical conductivity is σ = 7.1 S/m (Wolf et al. Wolf et al. (1986)). The fluid is injected downwardly into the cavity through a vertical, submerged nozzle of 0.4 m length. The inner dimensions of the nozzle are $d \times d$ = 0.01 $\times$ 0.01 m^2 and the outer dimensions are 0.02 $\times$ 0.02 m^2. The bulk velocity in the nozzle is v_{in}. The end of the nozzle is positioned at a depth d_n = 0.1 m below the equilibrium free surface level.

Liquid flows out of the cavity through two 0.04 $\times$ 0.035 m^2 rectangular holes in the bottom of the cavity into an external flow circuit. The holes are placed off center, such that a light sheet for PIV measurements can enter the measurement volume through the bottom plate. The liquid is recirculated back to the nozzle by a pump to maintain a constant volume of liquid in the cavity. The liquid is kept at a constant temperature of T = $20°C \pm 0.5°$C by means of an immersion cooler in the external circuit to guarantee a constant viscosity of the liquid.

A Cartesian coordinate system is defined with its origin located at the equilibrium position of the free liquid surface in the center of the cavity, see figure 5.1. The *x*-axis is parallel to the front wall of the cavity, and the *y*-axis is in the upward vertical direction. The x- and y- component of the velocity are denoted by u_x and u_y, respectively.

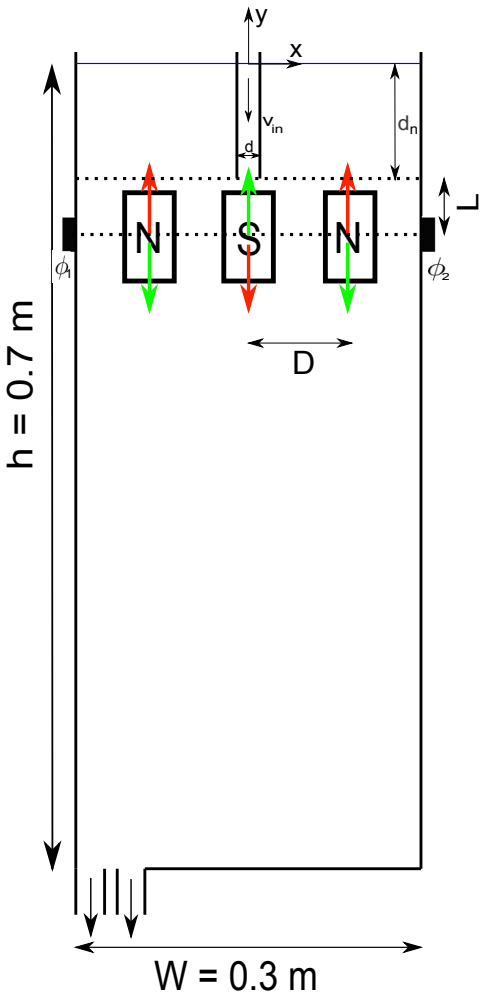

Figure 5.1: Experimental flow configuration. The inner dimensions of the cavity are $H \times W \times T = 0.8 \times 0.3 \times 0.035$ m^3. A 10 % Na_2SO_4 in water solution flows into the cavity through a nozzle with inner dimensions $d \times d$ = 0.01 $\times$ 0.01 m^2 and outer dimensions of 0.02 $\times$ 0.02 m^2. The nozzle is submerged to a depth d_n = 0.1 m below the free surface. The cavity is filled up to h = 0.7 m and the outflow is through two holes of 0.04 $\times$ 0.035 m^2 in the bottom of the cavity. Magnets are placed behind the cavity, and the vertical distance between the nozzle and the center of the magnets is denoted by L.

5.2.2 Electromagnetic forcing

Rolled up platinum electrode wires with a length of 0.8 m and a diameter of 1 mm are placed in compartments next to the cavity. The potential difference $\Delta\phi = \phi_1 - \phi_2$ between the electrodes can be set to a maximum of 50 V. This potential difference results in a maximum electrical current of $I = 4.0$ A between the electrodes. The electrodes are physically separated from the cavity by a porous wall, such that electrical contact is made, but bubbles due to electrolysis are prevented from entering the cavity. The area of the porous wall in the side wall of the cavity is 0.03×0.03 m^2. With an electrical current of I = 4.0 A, the mean current density at the position of the porous walls is $|\mathbf{j}| = 4.4 \times 10^3$ A/m^2.

Three permanent NdFeB magnets, each with dimensions $0.04 \times 0.04 \times 0.084$ m^3, are placed against the back wall of the cavity. The magnets are placed in a north-south-north configuration, such that the resulting Lorentz force is either up-down-up or down-up-down, depending on the direction of the electrical current. The horizontal distance between the centers of the magnets is D = 0.10 m. The magnetic field strength in the z-direction is measured using a Hall-flux sensor and the result is plotted for three values of z in figure 5.2. The center of the magnets is located at the same y-position as the center of the porous walls. The vertical distance between the nozzle and the center of the magnets is denoted as L, as indicated in figure 5.1.

5.2.3 PIV system

A Quantronix Darwin DUO 527-80-M laser and light sheet optics are used to produce a laser light sheet that enters the cavity through the bottom wall. The laser produces 27 mJ pulses at a wavelength of 527 nm and a repetition rate of 1000 Hz. Neutrally buoyant silver coated hollow glass spheres with a nominal diameter of 25 μm are used as seeding particles. The field of view has size 0.3×0.3 m^2 and shows the full width of the cavity (-0.15 m $< x <$ 0.15 m) and the region just below the nozzle ($-d_n - 0.3$m $< y < -d_n$). The light sheet is located in the $z = 0$ plane between the two broad walls of the cavity and the light sheet thickness in the measurement region is less than 1 mm. Particle images are recorded with an Imager HS pro 4M camera with a Nikon Nikkor 55 mm lens with $f^{\#}$ = 16. The camera is equipped with a 2016×2016 pixel CMOS-chip with a pixel size of 11×11 μm^2. Velocity vectors are calculated based on cross correlation of interrogation areas of 32×32 pixels with 75 % overlap using Davis 8.1 PIV software.

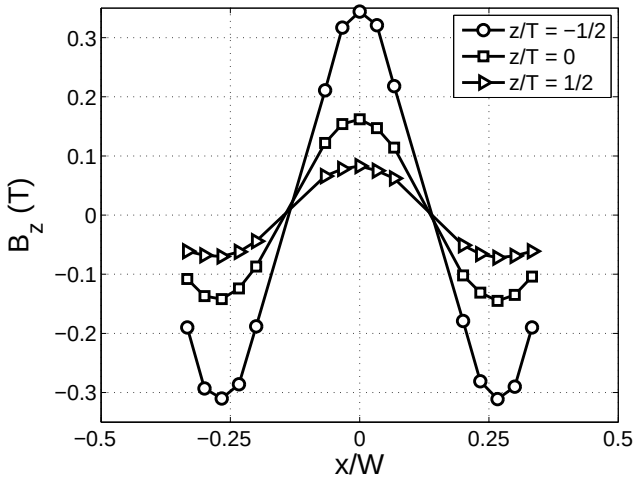

Figure 5.2: Measured z-component of the magnetic field strength at $y = -d_n - L$ for different positions in the x and z-direction.

5.2.4 Proper orthogonal decomposition

Due to the coherent nature of the investigated flows a proper orthogonal decomposition (POD, Holmes et al. (1996), Sirovich (1987)) can be applied to find dominant temporal and spatial energy modes in the flow. In the proper orthogonal decomposition, a time series of velocity fields is decomposed as

$$\mathbf{u}(\mathbf{x}, t) = \sum_{n=0}^{N} a_n(t)\phi_n(\mathbf{x}), \tag{5.1}$$

where the velocity field is expanded into a finite series of orthogonal spatial basis functions $\phi_n(\mathbf{x})$ and mutually uncorrelated time coefficients $a_n(t)$. Here n denotes the mode number and N is the number of snapshots from the PIV. The mode n = 0 is the mean velocity field. The lowest $n > 0$ modes are related to the large scale, low frequency fluctuations in the flow. The higher modes are related to the turbulent fluctuations. An overview of the proper orthogonal decomposition is provided in refs. Adrian and Westerweel (2011), Holmes et al. (1996), Sirovich (1987).

5.3 Relevant dimensionless numbers

The dimensionless momentum equation for the incompressible flow in the cavity reads

$$\frac{\partial \mathbf{u}}{\partial t} + (\mathbf{u} \cdot \nabla)\mathbf{u} = -\nabla p + \frac{1}{\mathrm{Re}}\nabla^2 \mathbf{u} + \mathrm{N}(\mathbf{j} \times \mathbf{B}), \tag{5.2}$$

where $\mathbf{u}$ is the dimensionless fluid velocity, p is the dimensionless pressure, $\mathbf{j}$ is the dimensionless electrical current density and $\mathbf{B}$ is the dimensionless magnetic field strength. The Lorentz force acting on the flow is given by $\mathbf{F}_L = \mathbf{j} \times \mathbf{B}$. For low conducting fluids (e.g. salt water), induced currents $\sigma(\mathbf{u} \times \mathbf{B})$ due to a magnetic field are small and the current density $\mathbf{j} = \sigma(\mathbf{E} + \mathbf{u} \times \mathbf{B}) \approx \sigma\mathbf{E}$ is independent of the local flow velocity. Then the Lorentz force is:

$$\mathbf{F}_L = \mathbf{j} \times \mathbf{B} \approx \sigma(\mathbf{E} \times \mathbf{B}) \tag{5.3}$$

Two dimensionless numbers appear in equation 5.2, the Reynolds number:

$$\mathrm{Re} = \frac{v_{in} d}{\nu}, \tag{5.4}$$

and the Stuart number:

$$\mathrm{N} = \frac{\sigma E_{ref} B_{ref} d}{\rho v_{in}^2}. \tag{5.5}$$

The quantities used to determine the values of N and Re are the maximum measured magnetic field strength B_{ref} = 0.15 T in the z-direction at ($x/W = 0, y = -d_n - L, z/T = 0$), the nozzle hydraulic diameter d = 0.01 m, the liquid density ρ = 1.10 $\times 10^3$ kg/m^3 and the liquid viscosity $\nu = 1.27 \times 10^{-6}$ m^2/s. The two varied parameters in N and Re are the current density at the position of the porous walls, $\sigma E_{ref} = |\mathbf{j}_{ref}|$, and the inlet velocity, v_{in}. When v_{in} = 0 m/s, the characteristic velocity in the Stuart number is taken to be the maximum measured time-averaged velocity in the vertical direction induced by the Lorentz force above the middle magnet, v_{max}.

A third relevant dimensionless parameter in this study is the Strouhal number, defined as

$$\mathrm{St} = \frac{fW}{v_{in}}, \tag{5.6}$$

which can be interpreted as a dimensionless frequency. The frequency f is made dimensionless using the inlet velocity v_{in} and the width of the cavity W, in accordance with Lawson and Davidson Lawson and Davidson (2001). As before, in case v_{in} = 0 m/s the characteristic velocity is taken to be v_{max}.

5.4 Jet oscillations without Lorentz forcing (N = 0)

PIV measurements with a duration of five minutes and with a sampling rate of 1 fps have been performed in flows with $\Delta\phi = 0$, i.e. without an applied Lorentz force. Figure 5.3 shows four PIV snapshots of the flow for Re = 7.1 $\times$ 10^3, illustrating one period of a jet oscillation. The oscillation period is about 30 seconds.

A proper orthogonal decomposition is performed on the PIV snapshots to calculate the first temporal mode $a_1(t)$ for different values of the Reynolds number. The temporal mode $a_1(t)$ is connected to the most energetic fluctuations in the flow: the large scale jet oscillation Semeraro et al. (2012). Figure 5.4 shows a distribution of the fraction of kinetic energy present in the temporal modes $a_n(t)$ of the POD. It is seen that the fraction of energy contained in the first mode $a_1(t)$ is 39%. Figure 5.5 (left) shows a time trace of $a_1(t)$ and figure 5.5 (right) shows the corresponding power spectrum. A dominant frequency is found at f = 0.033 Hz, in accordance with the oscillation period of 30 seconds. The Strouhal number is determined With this dominant frequency. The same procedure is applied for measurement results for Reynolds numbers between Re = 1.5$\times$$10^3$ and Re = 3.0$\times$$10^4$. Figure 5.6 shows that the Strouhal number is independent of the Reynolds number, which is in accordance with results presented in literature Lawson and Davidson (2001), Mataoui and Schiestel (2009), Maurel et al. (1996), Uzol and Camci (2002).

5.5 Pure Lorentz forcing of the flow (Re = 0)

PIV measurements of the flow due to the Lorentz force only (i.e. in absence of jet inflow, $v_{in} = 0$) have been performed at a recording rate of one image pair per second and with a duration of five minutes. Figure 5.7 shows the mean velocity field for an electrical current of I = 4.0 A for the up-down-up forcing configuration (left) as well as for the down-up-down forcing configuration (right). It is seen that the flow patterns are reversed due to the reversed electromagnetic forcing. In figure 5.7right, the free surface is present at y/W = 0, which leads to a confinement of the recirculation zones, while in figure 5.7left this is not the case. The magnet positions are indicated by

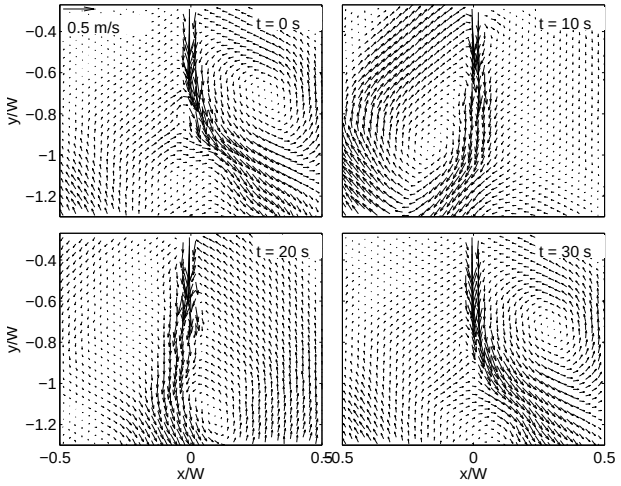

Figure 5.3: Jet oscillation at N = 0, Re = 7100. Going from left top to right bottom, the time between the first and the last image is 30 seconds. The height and width of the images is 0.3 m.

the rectangles. In the remainder of this section we focus on the flow in the up-down-up forcing configuration.

The Lorentz force at the center magnet position is in the downward direction, causing a relatively large flow velocity in the downward direction at $x/W = 0$. The Lorentz force at the position of the left and right magnets is in the upward direction, causing an upward directed flow. The combination of the three magnets results in two counter rotating recirculation zones on the left and on the right of the center magnet. The maximum velocity in the flow field, v_{max} = 0.08 m/s, is found at $x/W = 0$ and $y/W = -0.6$, so below the center of the middle magnet. The centers of the two counter rotating recirculation zones are also located below the position of the center of the middle magnet, at $y/W = -0.4$ and $x/W = \pm 0.2$. Above the magnets on the left and on the right two secondary recirculation zones emerge.

Figueroa et al. Figueroa et al. (2009) reported results for flows of saline solutions in shallow layers due to a Lorentz force produced by the combination of a single magnet and an electrical field. They report that the centers of the recirculation zones and the location of the maximum velocity v_{max} are located downstream of the center of the magnet, which is

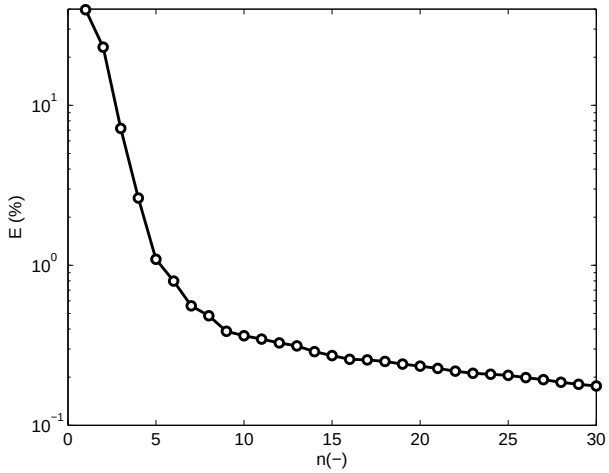

Figure 5.4: Energy contained in POD modes 1-30 shown as a percentage of the total kinetic energy.

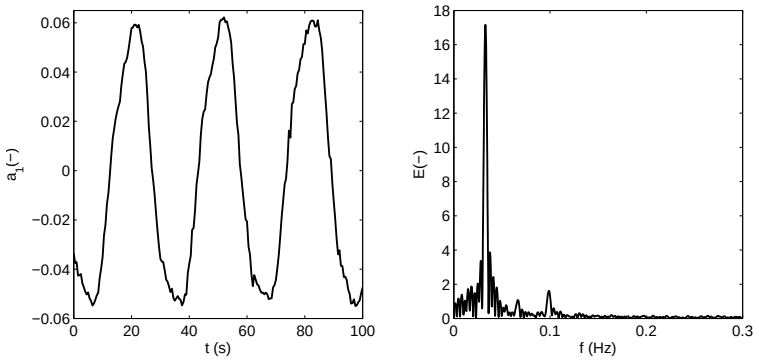

Figure 5.5: *Left*: Time trace of the first temporal mode $a_1(t)$ of the POD for Re = 7100. *Right*: Power spectrum of the time trace of $a_1(t)$, a clear peak is found at f = 0.033 Hz, with second harmonics at f = 0.067 Hz and f = 0.099 Hz.

in agreement with the results presented in figure 5.7left.

Duran-Matute et al. Duran-Matute et al. (2011) reported results for stationary flows of saline solutions due to a Lorentz force produced by three magnets in the south-north-south configuration in combination with an

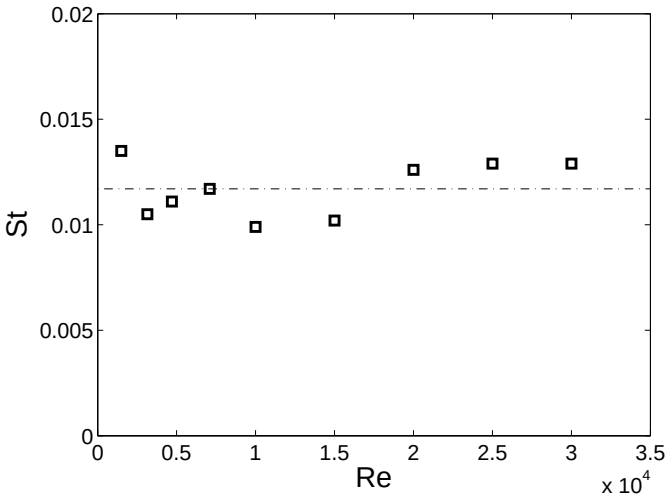

Figure 5.6: Strouhal number as a function of Reynolds number for flows with a confined jet without an applied Lorentz force.

electrical field. Streamwise elongated vortices, similar to the ones observed in figure 5.7, were reported. They also found the small recirculation zones above the left and right magnet, shown in the top right and top left corner of figure 5.7left.

Figure 5.8 shows v_{max}^2 as a function of the applied electrical current. It is observed that $v_{max} \propto \sqrt{I} \propto \sqrt{\sigma E}$, which is to be expected when the Lorentz force is balanced by the inertial forces Duran-Matute et al. (2011): $v_{max} = \sqrt{\sigma EBl/\rho}$. For the calculation of v_{max}, the distance between the centers of the magnets ($D = 0.1$ m) is used as the typical length scale l. It is seen that the calculated velocity over estimates the measured velocity by a factor of about 3, so $v_{max} = \alpha\sqrt{\sigma EBl/\rho}$, with $\alpha \approx 0.33$. The over estimation of the calculated velocity is expected due to the oscillatory flow behavior and from an over estimation of the electrical current density σE at the position of the center magnet.

The flow in the cavity induced by the Lorentz forces is non-stationary. The eddies on the left and the right interact with each other, leading to an oscillating behavior of the downward moving flow emerging at the position of the center magnet. The oscillations can exist due to the confined space in the x- and z-direction. A proper orthogonal decomposition is performed on the snapshots from the PIV measurement with the up-down-up forcing

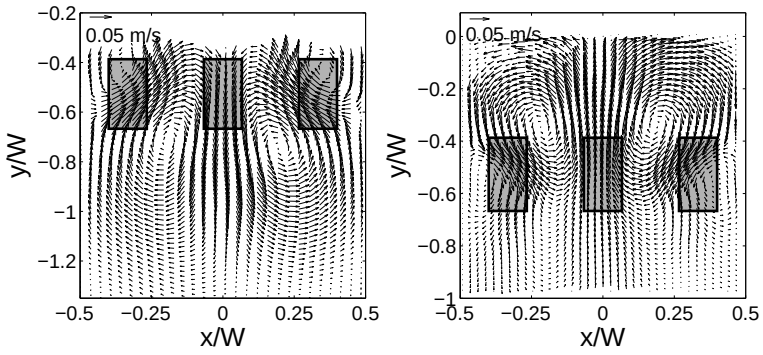

Figure 5.7: Mean velocity field for I = 4.0 A in combination with the magnetic field in the up-down-up configuration. The gray rectangles indicate the magnet positions.

configuration. From the first temporal mode, $a_1(t)$, the dominant frequency of the most energetic fluctuating structures in the flow is determined. Figure 5.8 shows the square of the frequency as a function of the applied current. The results indicate that the frequency f is proportional to the square root of the electrical current I which means St$\propto \sqrt{\mathrm{N}}$.

Table 5.1 summarizes measured maximum velocities and frequencies, depending on the forced electrical current. In analogy with the self-sustained jet oscillations discussed in section 5.4, it is expected that $f \propto v_{max}$, and since $v_{max} \propto \sqrt{I}$ it follows that $f \propto \sqrt{I}$. This would lead to a constant Stuart number N and to a constant Strouhal number St, as can indeed be seen in table 5.1. The constant of proportionality between the square root of the Stuart number and the Strouhal number is approximately 0.1:

$$\mathrm{St} \approx 0.1\sqrt{\mathrm{N}}. \tag{5.7}$$

Contrary to the present experiment, no flow oscillations were reported by Figueroa et al. Figueroa et al. (2009) and by Duran-Matute et al. Duran-Matute et al. (2011). This can be expected since in their experiments, there was no confinement of the vortices in the x- or y-direction.

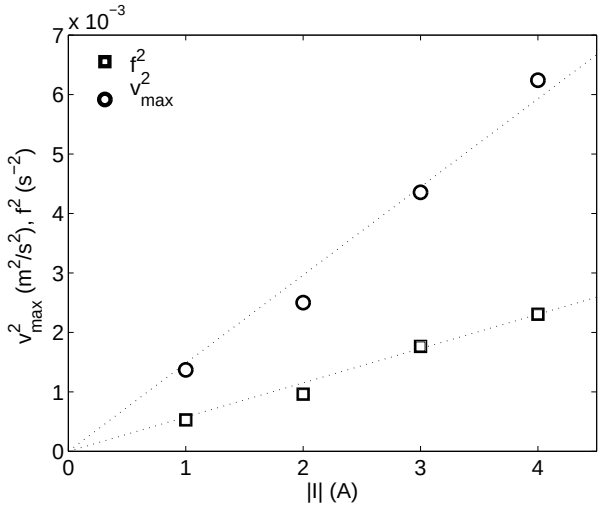

Figure 5.8: □ Square of the dominant frequency in the flow as a function of the electrical current in purely electromagnetically forced flow ($v_{in} = 0$). ○ Square of the maximum of the mean velocity in the flow as a function of the electrical current in the purely electromagnetically forced flow ($v_{in} = 0$).

5.6 Mixed forcing (N $>$ 0, Re $>$ 0): Up-down-up

In the previous two sections we discussed the two limiting cases of zero jet flow (Re = 0) and zero Lorentz force (N = 0), respectively. This section presents results from measurements with combined jet flow (Re > 0) and flow induced by the Lorentz force (N > 0). Figure 5.9 shows St as a function of N being independent of the dimensionless distance between the nozzle and the center of the middle magnet, L/d. Two regimes can be distinguished, separated by a critical Stuart number $\mathrm{N}_c \approx 0.01$. The Lorentz force is significant in this configuration, even for Stuart numbers far below one. This is due to the choice of the characteristic length and velocity scales in our definition of the Stuart number, as mentioned in section 5.3.

For $\mathrm{N} < \mathrm{N}_c$, inertia forces are dominant, the Strouhal number is constant and has the same value as in the case without Lorentz forces: St = 0.012 (figure 5.6). For $\mathrm{N} > \mathrm{N}_c$, the Lorentz forces are dominant and the Strouhal number is proportional to the square root of the Stuart number, $\mathrm{St} \propto \sqrt{\mathrm{N}}$. The constant of proportionality between St and $\sqrt{\mathrm{N}}$ is approximately 0.1, as was the case for $v_{in} = 0$ in section 5.5.

$\|I\|$ (A)	v_{max} (m/s)	f (Hz)	N	St
1.0	0.037	0.023	3.48	0.186
2.0	0.050	0.031	3.81	0.182
3.0	0.066	0.042	3.28	0.190
4.0	0.079	0.048	3.06	0.182

Table 5.1: Maximum of the mean velocity v_{max}, dominant frequency f, Strouhal number St and the Stuart number N for various values of the electrical current I.

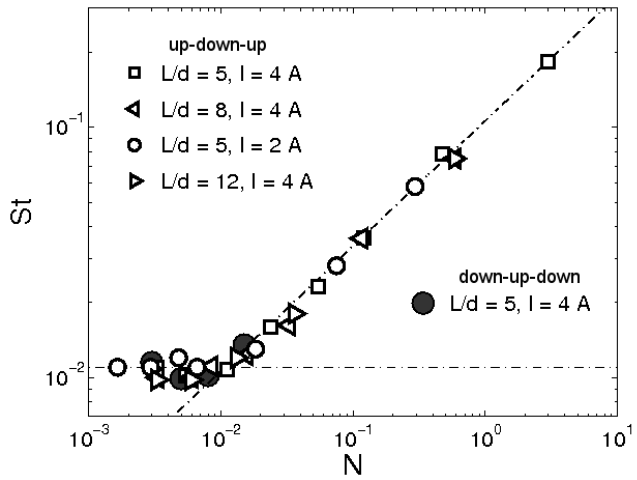

Figure 5.9: Strouhal as a function of Stuart. The straight lines are the lines St = 0.012 and St$= 0.1\sqrt{N}$ and they intersect at the critical Stuart number, $\mathrm{N_c} = 0.01$.

5.7 Mixed forcing (N $>$ 0, Re $>$ 0): Down-up-down

In addition to the results for up-down-up forcing, figure 5.9 also shows St as a function of N for the down-up-down forcing configuration. For $\mathrm{N} < \mathrm{N}_c \approx 0.01$, St is again constant and equal to the value found for the up-down-up configuration and to the value found in the absence of Lorentz forces, indicating that inertia forces are dominant. For $\mathrm{N} > \mathrm{N}_c$, however, the oscillations are suppressed in the case of down-up-down forcing. Measurements have been performed for N $>$ 0.01, all leading to full suppression of the oscillations and therefore not shown as data points in figure 5.9.

Figure 5.10 shows the fraction of the energy contained in the first spatial

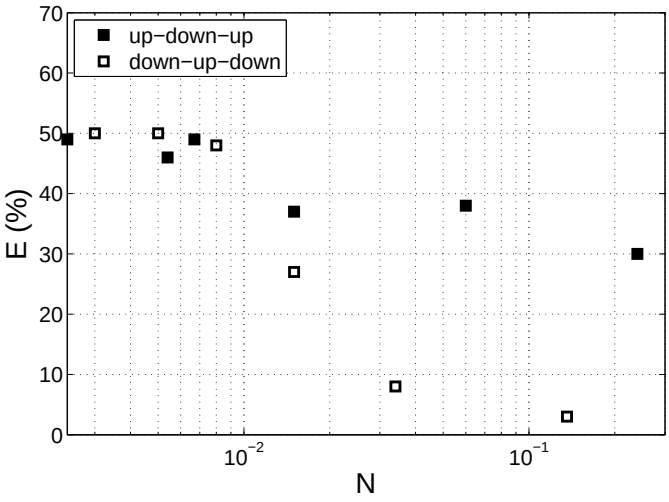

Figure 5.10: Fraction of the kinetic energy contained in the first mode of the POD as a function of the Stuart number for the up-down-up and the down-up-down configuration.

mode of the POD as a function of the Stuart number. It is seen that for $N > N_c \approx 0.01$ the fraction of the kinetic energy contained in the first spatial mode sharply drops for the down-up-down configuration. This indicates the suppression of the oscillation and hence a stabilizing effect on the flow. To investigate the effect of the Lorentz force on the jet oscillations, mean velocity profiles, profiles of the turbulence kinetic energy and results from the POD have been calculated. These will be discussed in sections 5.7.1, 5.7.2 and 5.7.3, respectively. The analysis is done for flows with Reynolds numbers of Re = 3150 (N = 0.05), Re = 4700 (N = 0.02) and Re = 7100 (N = 0.007).

5.7.1 Mean velocity field

Figure 5.11 shows the mean velocity fields for the (oscillation suppressing) down-up-down forcing configuration (left) and for the configuration without Lorentz forces (right). The gray tone indicates the magnitude of the mean velocity $|u| = \sqrt{u_x^2 + u_y^2}$, where a dark tone indicates a high velocity. The velocity fields are made dimensionless with the inlet velocity v_{in}. For good visualization of the mean flow pattern, the values of the dimensionless velocity have been clipped at $|u|/v_{in} = 0.5$. As expected, the maximum

velocity occurs in the near jet region in all cases. For Re = 3150 (N = 0.05) and Re = 4700 (N = 0.02) the flow induced by the Lorentz force results in the formation of recirculation zones in the top corners. These recirculation zones are absent for Re = 7100 (N = 0.007).

The mean velocity fields in figure 5.11 give a good indication of the global flow pattern in the cavity, but due to a lack of spatial resolution of the PIV measurements, accurate quantitative data can not be determined from these measurements. Figure 5.12 shows quantitative results of the normalized velocity in the vertical direction, u_y, from PIV measurements with a smaller field of view zoomed in into the jet region. The field of view is $-d_n < y < -d_n - 0.15$m and -0.15 $< x/W <$ 0.15. This results in a spatial resolution of 200 μm per interrogation area and with 50 % overlap between the interrogation areas this results in 1 velocity vector per 100 μm. The measurement time was 126 seconds at a sampling rate of 25 fps, resulting in 3155 image pairs. The velocity profiles shown here are taken at $y = -d_n - 0.08$m, i.e. 8 pipe diameters downstream from the nozzle exit. The x-position of the nozzle is indicated by the vertical lines at $|x/W| = 0.017$. The edges of the center magnet are indicated by the vertical lines at $|x/W| = 0.067$. Figure 5.12 shows that the peak velocity is reduced by 20 % due to the Lorentz force when Re = 3150 (N = 0.05). The velocities outside the jet region are affected in the cases with Re = 3150 (N = 0.05) and Re = 4700 (N = 0.02). For $|x/W| > 0.05$ a reversal of the flow direction is seen, which is due to the upward directed Lorentz force. In the jet region this upward directed Lorentz force is overcome by the jet, but outside the jet region this results in an upward directed flow. When Re = 7100 (N = 0.007) the flow reversal due to the Lorentz force has vanished, indicating that the flow in this case is dominated by the jet flow.

5.7.2 Turbulence kinetic energy distribution

The Reynolds decomposition of the horizontal velocity component is

$$u_x = \overline{u_x} + u'_x, \tag{5.8}$$

where u_x is the instantaneous velocity component, $\overline{u_x}$ is the mean velocity and u'_x is the velocity fluctuation associated with turbulence. With a similar decomposition for u_y, the two-dimensional turbulence kinetic energy is then calculated from

$$k = 1/2[\overline{u'^2_x} + \overline{u'^2_y}]. \tag{5.9}$$

The two-dimensional representation of the turbulence kinetic energy is used since measurements are performed with a two-component PIV system.

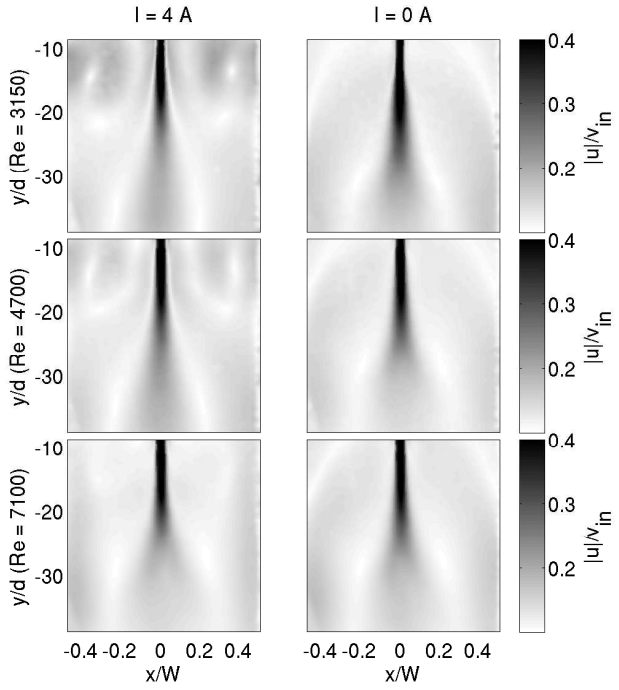

Figure 5.11: Mean velocity magnitude made dimensionless with the inlet velocity for the down-up-down forcing configuration. From top to bottom, the values of the Stuart number in the left column are N = 0.05, N = 0.02 and N = 0.007.

Figure 5.13 shows the spatial distribution of the turbulence kinetic energy, made dimensionless with the square of the inlet velocity, calculated from the same measurement data used to calculate the mean velocity fields in figure 5.11. The values of k/v_{in}^2 have been clipped at $k/v_{in}^2 = 0.025$ to provide a clearer picture of the global distribution of the turbulence kinetic energy. A peak in k is located near the jet exit region in all three cases, when moving in the streamwise direction, the jet shear layer spreads while turbulence levels decrease. This is due to the entrainment of low velocity ambient fluid. Due to the limited spatial resolution of the PIV measurements in the jet region, the jet shear layers can not be resolved in detail.

In absence of the Lorentz force ($I = 0$), two lobes are present in the turbulence kinetic energy distribution. These lobes are related to the extreme positions of the oscillating jet. When down-up-down forcing is applied with

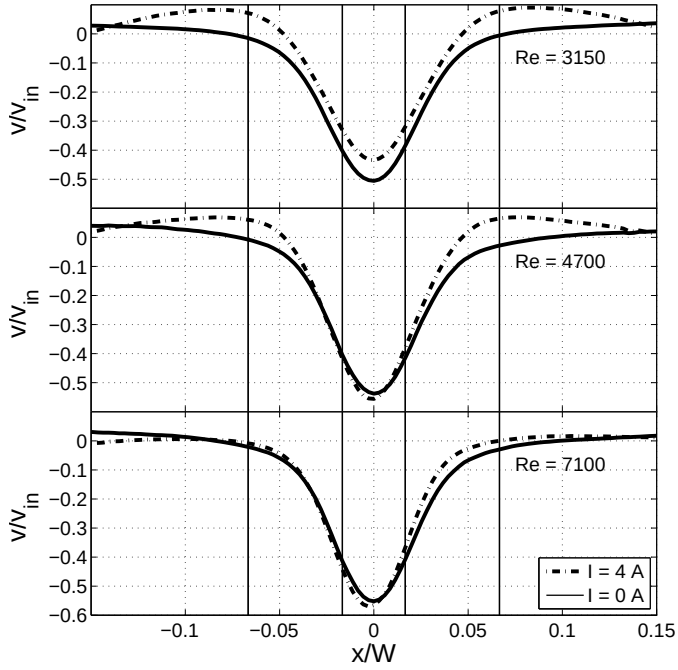

Figure 5.12: Profiles of the y-component of the mean velocity u_y at $y = -d_n - 0.08$m. The vertical lines at $|x/W| = 0.017$ indicate the x-position of the inner nozzle walls and the vertical lines at $|x/W| = 0.067$ indicate the x-position of the edges of the middle magnet.

an electrical current of I = 4.0 A it is seen that the strength of the lobes is reduced for Re = 3150 (N = 0.05) and Re = 4700 (N = 0.02). This indicates that the Lorentz force for the down-up-down configuration has a stabilizing effect on the large scale jet fluctuations. For Re = 7100 (N = 0.007) the applied Lorentz forcing has no observable effect on the jet oscillations, indicating that the transition from electromagnetically dominated flow towards inertia dominated flow is between N = 0.02 and N = 0.007 in agreement with the earlier found critical Stuart number N_c = 0.01.

5.7.3 Proper orthogonal decomposition

A POD is performed on the PIV snapshots that were used to calculate the results shown in figures 5.11 and 5.13. Values of the fraction of the turbulence

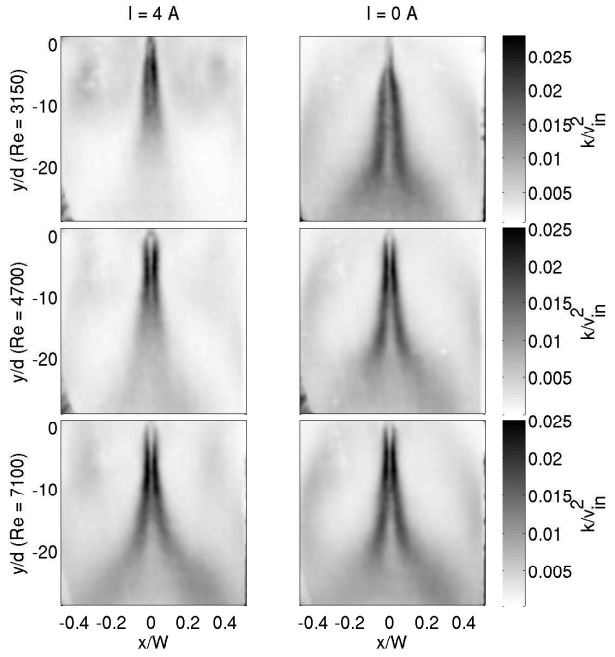

Figure 5.13: Turbulence kinetic energy, determined from a set of 300 PIV velocity fields recorded at a frequency of 1 fps. From top to bottom, the values of the Stuart number in the left column are N = 0.05, N = 0.02 and N = 0.007.

kinetic energy contained in the first spatial POD mode, ϕ_1, for Reynolds numbers of 3150 (N = 0.05), 4700 (N = 0.02) and 7100 (N = 0.007) are listed in table 5.2. It is seen that the energy contained in the first POD mode is lowest for cases with Lorentz forcing and Re = 3150 (N = 0.05). This indicates that at a relatively low inlet velocity, the large scale structures in the flow are stabilized considerably when the Lorentz force is applied. Figure 5.15 shows the energy per POD mode number n as a fraction of the total kinetic energy for modes 1-30. For Re = 3150, the distribution of the fraction of kinetic energy is affected significantly by the presence of electromagnetic forcing, leading to a more or less even distribution of the kinetic energy. For Re = 7100, the distributions of the fraction of the kinetic energy are equal for the cases with and without electromagnetic forcing, leading to the conclusion that in this case the electromagnetic forcing does not affect the flow dynamics.

Figure 5.14 shows phase diagrams of the first and second temporal modes,

Re	I = 0 A	I = 4.0 A
3150	32 %	6 %
4700	39 %	39 %
7100	39 %	46 %

Table 5.2: Fraction of the turbulence kinetic energy contained in the first spatial mode of the POD, $\phi_1(\mathbf{x})$, for varying Reynolds numbers and with and without applied Lorentz forcing.

$a_1(t)$ and $a_2(t)$, for the cases with and without Lorentz forcing for Re = 3150 (N = 0.05), Re = 4700 (N = 0.02) and Re = 7100 (N = 0.007). In flows with strong periodicities these temporal modes reduce to the first two Fourier modes, which have a phase difference of 90 degrees. In the cases without Lorentz forcing, the coefficients show a closed curve of ellipsoidal shape. This indicates that $a_1(t)$ and $a_2(t)$ are periodic with the same frequency. The axes of the ellipsoid are aligned with the x- and y-axis, indicating that the phase difference between $a_1(t)$ and $a_2(t)$ is 90 degrees. This indicates that the large scale flow dynamics in these flows can be described using only two POD modes. When a Lorentz force is applied with N > 0.02, a deviation from the ellipsoidal shape is observed, indicating that the low dimensional description for the oscillating jet is not valid anymore. For N = 0.05, the coefficients $a_1(t)$ and $a_2(t)$ no longer form a closed curve, indicating that in this case more POD modes are necessary to describe the flow dynamics correctly.

5.8 Physical mechanism of the jet oscillation

Figure 5.16 schematically shows the main stages of the jet oscillation. Visual observation of the start up phase of the jet oscillation showed that the jet initially flows straight to the bottom of the cavity, inducing (nearly) symmetric recirculation zones on both sides of the jet (stage A). Once the high velocity liquid of the jet reaches the bottom of the cavity, the fluid preferentially moves either towards the left wall or the right wall. This is a random process, but in the description below it is assumed that the jet fluid moves towards the right. Then the fluid moves upward along the right wall thus forming a recirculation zone (stage B). The recirculation zone has a pressure minimum in its center that causes the jet fluid to bend towards the right, thus feeding the right recirculation zone. The jet bending continues to increase until the jet impinges on the side wall with the impingement point gradually moving upward. The impinging jet splits in an upward directed part and a downward directed part. The part of the jet fluid flowing towards the bottom of the

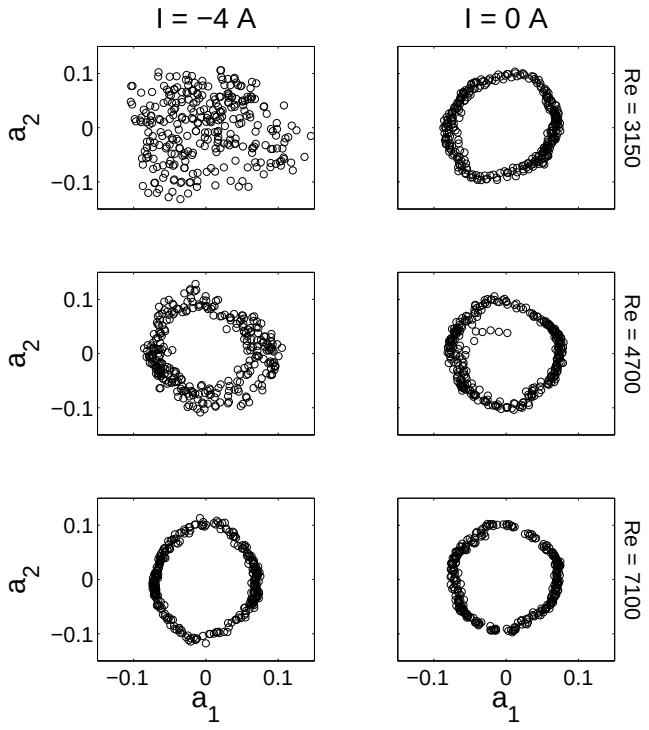

Figure 5.14: Phase diagram of the first and second temporal POD coefficients $a_1(t)$ and $a_2(t)$. From top to bottom, the values of the Stuart number in the left column are N = 0.05, N = 0.02 and N = 0.007.

cavity leads to the formation of a recirculation zone on the other side of the jet. The strength of this recirculation zone gradually increases thus increasing the pressure difference between the jet and the center of this recirculation zone. The jet is then drawn towards the left in stage C until it impinges on the side wall in stage D and from then on the process repeats itself.

To quantitatively investigate this oscillation mechanism, attention was focused on the temporal variation of the jet angle θ and the vertical fluid velocity u_y on both sides of the jet, following the approach presented by Honeyands and Herbertson Honeyands and Herbertson (1995) and in our previous publication Kalter et al. (2013). In Figure 5.17 (left) the jet angle θ is defined as the angle between (1) the vertical line $x = 0$ and (2) the line through the position of the maximum jet velocity at $y = -0.3$ m and the tip

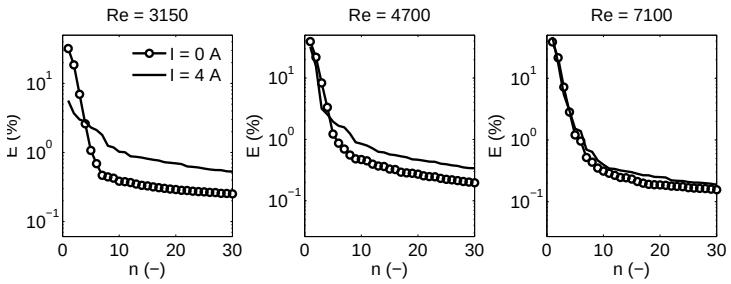

Figure 5.15: Energy contained in POD modes 1-30 shown as a percentage of the total kinetic energy.

of the nozzle. The jet angle is assumed to be positive when the jet is directed to the right. The vertical fluid velocity on the left and on the right of the jet was monitored at $y = -0.175$ m and $x = \pm 0.1$ m. When the liquid velocity is directed in the upward direction, the velocity is positive.

Figure 5.17(right) shows both the jet angle and the vertical velocities for a jet Reynolds number of 3150 and a Lorentz force in the up-down-up configuration (N = 0.05). Three characteristic events in the jet oscillation have been marked with numbers. At $t = 35$ s (1) the jet angle has a maximum, meaning that the jet is flowing towards the right wall. This is when the jet impinges on the side wall and splits in an upward and downward part (see figure 5.16b). The velocity on the right side of the jet is decreasing, while the velocity on the left is increasing leading to the formation of a strong recirculation zone on the left. At $t = 41$ s (2) the velocity on the left side of the jet has a maximum and the velocity on the right has a minimum. The jet angle is still decreasing (figure 5.16c). At $t = 43$ s (3) the jet angle reaches its minimum, and at this point the velocity on the right is growing and the velocity on the left is decreasing, leading to the formation of the strong recirculation cell on the right (figure 5.16d). Now the same process repeats, leading to a stable jet oscillation.

When the Lorentz force is in the up-down-up configuration (as is the case for the results shown in figure 5.17) the upward directed flow due to the Lorentz force on the right side of the jet adds to the growing velocity in the initial recirculation zone that forms on the right side of the jet. This leads to a faster growth of the velocity in the recirculation zone. When the jet angle has a maximum value and the velocity on the left starts to grow, this growth is enhanced by the presence of the upward directed flow due to the Lorentz force on the left side and the jet is drawn to the left much quicker than in the absence of the Lorentz force. The whole process of the formation of recirculation zones

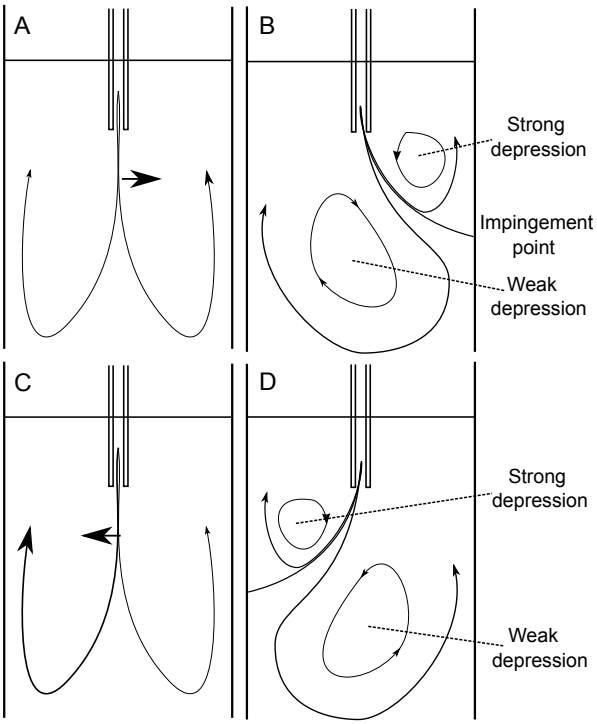

Figure 5.16: Schematics of subsequent stages of the jet oscillation. A: Initially the jet flows symmetrically towards the bottom of the cavity and then it is bended towards the right. B: The jet has bended towards the recirculation zone on the right until it impinges on the right wall. The jet splits in an upward moving part and in a downward moving part. C: The jet has moved to the neutral position ($\theta = 0$), moving towards the left. D: The jet impinges on the left wall and splits in an upward moving part and in a downward moving part.

is faster leading to a higher oscillation frequency when the Lorentz force is applied in the up-down-up configuration as was already depicted in figure 5.9.

When the Lorentz force is in the down-up-down configuration the flow due to the presence of the Lorentz force at the position of the left and right magnet is in the downward direction. This means that the formation of the recirculation zones is hampered by the Lorentz force. If the Lorentz force is of sufficient strength (in comparison to the inertial forces) it prevents the formation of the low pressure regions next to the jet. This means that the

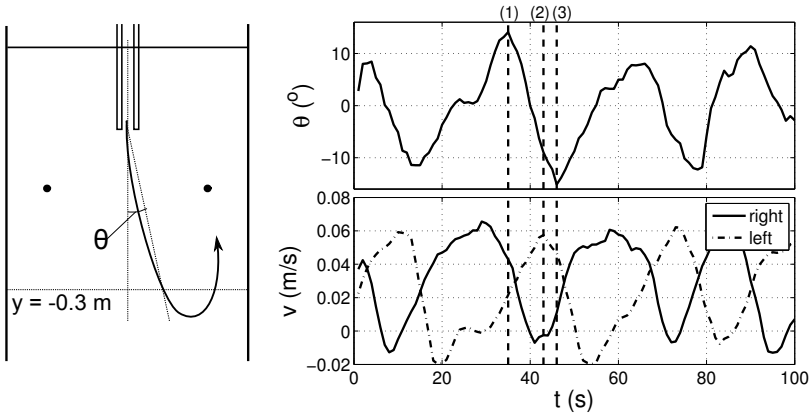

Figure 5.17: *Left:* The jet angle θ is defined as the angle between the vertical line through $x = 0$ and the line through the position of the maximum in the jet velocity at $y = -0.3$ m and through the tip of the nozzle θ. The dots on the left and right indicate where the vertical component of the velocity is monitored. *Right,top:* Jet angle development, a positive jet angle means that the jet is directed to the right. *Right, bottom:* Variation of the vertical velocity on the left and the right of the jet at $y = 0.175$ m and $x = \pm 0.1$ m. A positive velocity means that the fluid moves in the upward direction. Re = 3150 and N = 0.05 with the Lorentz force in the up-down-up configuration.

mechanism needed for the jet oscillation has disappeared, as was shown for the flow with Re = 3150 and N = 0.05.

5.9 Conclusions

The effect of Lorentz forcing on self-sustained oscillations of a liquid jet flowing into a liquid filled thin cavity has been studied. The Lorentz force was imposed on the fluid by applying a magnetic field in a north-south-north configuration in conjunction with an electric field perpendicular to the magnetic field. The Lorentz force could be either in the up-down-up configuration or in the down-up-down configuration, by reversing the electrical current.

A critical Stuart number of $N_c \approx 0.01$ was found. For $N < N_c$, the jet oscillates with a constant Strouhal number, St = 0.012, for $1500 < Re < 30000$. For $N > N_c$ in the (oscillation enhancing) up-down-up configuration, St grows with N as $St \approx 0.1\sqrt{N}$. In contrast, for $N > N_c$ in the (oscillation suppressing)

down-up-down configuration, oscillations are suppressed.

Chapter 6

Electromagnetic flow control in a rectangular cavity with a bifurcated nozzle[1]

The effect of Lorentz forcing on self-sustained oscillations of jets issuing from a submerged bifurcated nozzle into a thin rectangular cavity was investigated using free surface visualization and time-resolved particle image velocimetry (PIV). A permanent Lorentz force is supplied by applying an electrical current across the width of the cavity and by imposing a permanent magnetic field perpendicular to the electrical current. As a working fluid a saline solution is used for an increased electrical conductivity. The Lorentz force can be directed downward ($F_L < 0$) or upward ($F_L > 0$), to reduce or enhance the self-sustained jet oscillations. When $F_L < 0$ the amplitude of the free surface oscillations is reduced by a factor of 6 and the frequency of the oscilations is reduced from f = 0.04 Hz to f = 0.03 Hz. When $F_L > 0$ the free surface oscillation amplitude is enhanced by a factor of 1.5 and the oscillation frequency increases from f = 0.04 Hz to f = 0.05 Hz.

A proper orthogonal decomposition (POD) was applied to the set of instantaneous PIV velocity fields. Due to the presence of the unsteady large scale motion, a large fraction of the turbulence kinetic energy $k = \frac{1}{2}\overline{u_i' u_i'}$ is due to the very low frequency modes of the POD. When $F_L < 0$ the fraction of turbulence kinetic energy contained in the first fluctuating mode is 20 %, when $F_L = 0$ this fraction is 42 % and when $F_L > 0$ this fraction is 56 %, indicating that the structure of the large scale unsteady motion is reduced when $F_L < 0$ and increases when $F_L > 0$.

A triple decomposition of the instantaneous velocity was used to divide the

[1]Published in International Journal of Heat and Fluid Flow 47:113-122, 2014

turbulence kinetic energy into a part originating from the large scale oscillation k_{osc} and a part originating from the turbulent fluctuations' turbulence kinetic energy k_{turb}. It follows that the Lorentz force does not influence k_{turb} in the measurement plane, but the distribution of k_{osc} is altered significantly due to the Lorentz force.

6.1 Introduction

Flow instabilities in liquid steel in a continuous casting mould are controlled in a non-intrusive manner by using induced magnetic forces. Magnets placed next to the casting mould in conjunction with induced electrical currents produce a Lorentz force that acts in a direction opposite to the local flow direction. This so-called electromagnetic braking in the continuous casting mould is investigated computationally by, for example, Haiqi et al. (2008) and Garcia-Hernandez et al. (2010). Velocity measurements in flows of liquid metal alloys with electromagnetic forcing are performed by, for example, Harada et al. (2001) and Timmel et al. (2010). However, experimental methods in liquid metals are still immature. In the field of continuous casting, experiments are often performed in scale models using water as a working fluid (e.g. Honeyands and Herbertson (1995), Torres-Alonso et al. (2007)). Water has the advantage that it is transparent, so that well-developed, non-intrusive measurement techniques like PIV and LDA can be used. The kinematic viscosity of water and liquid steel are approximately the same (within 20 %, Yuan et al. (2004)), so Reynolds similarity is reached when an exact replica of the caster mould configuration is employed. Electromagnetic flow interaction in these experiments is not possible since the electrical conductivity of water is too low. Recently Andreev et al. (2013) reported measurements with induced magnetic forcing of a transparent liquid. This was done using a sulphuric acid solution with electrical conductivity σ = 87 S/m as a working fluid and a superconducting magnet with a maximum magnetic field strength B = 5 T. The experiment was conducted in a cylindrical vessel with a diameter of 0.28 m and a height of 0.15 m and in a Reynolds number range of $5 <$Re < 100. Experiments modeling continuous casting processes are performed in larger facilities with higher Reynolds numbers, so this way of magnetic forcing of the flow is not (yet) possible.

To introduce electromagnetic forcing in transparent saline solutions with low electrical conductivity (1 S/m $< \sigma <$10 S/m), a combination of permanent magnets and imposed electrical currents can be applied. This results in a constant Lorentz force that is independent of the local flow field. This concept was used to increase laminar mixing (Rossi et al. 2009; 2012a;b), to increase heat transfer (Kenjereš 2008, Kenjereš et al. 2009) and to delay flow separation

(Crawford and Karniadakis 1997, Henoch and Stace 1995).

Electromagnetic control of turbulent channel flows of saline solutions was investigated by Berger et al. (2000) and Spong et al. (2005) using actuators where electrodes and magnets are placed at the wall of the channel in an alternating pattern. This produced a wall parallel forcing and reduced wall friction considerably. Electromagnetic actuators are also investigated by Kim and Lee (2000) and Zhang et al. (2010) for flow past a cylinder where vortex shedding in the wake of the cylinder is suppressed and by Weier et al. (2008; 2003) and Cierpka et al. (2008) for flow about an airfoil to prevent flow separation.

In the present work electromagnetic control of the flow in a thin rectangular cavity with a submerged bifurcated nozzle and with a free air/water interface is investigated. The dynamics of the flow and the air/water interface in absence of electromagnetic forcing have been reported in an earlier publication (Kalter et al. (2013)). It was observed that low-frequency, self-sustained jet oscillations were present in the cavity for a large range of inlet velocities and nozzle depths. The objective of the present work is to determine the effect of the Lorentz force on these self-sustained jet oscillations.

In continuous casting the flow along the steel/slag interface can cause entrainment of particles into the bulk flow, which can have a detrimental impact on the steel quality. Oscillations of the jet issuing from the nozzle cause local and temporal peaks in the velocity at the steel/slag interface, increasing the risk of entrainment. Therefore a secondary objective is to apply the Lorentz force as a flow control device to reduce jet oscillations and hence to reduce peaks in the flow velocity along the steel/slag interface, which is modeled as the air/water interface in the experiments.

Due to the coherent nature of the flow a proper orthogonal decomposition (POD, Holmes et al. (1996), Sirovich (1987)) can be applied to find dominant temporal and spatial energy modes in the flow. The POD analysis is performed to investigate the distribution of kinetic energy over the different sized structures in the flow. A separation is made between energy attributed to the large scale fluctuations and the energy attributed to turbulence.

6.2 Electromagnetic flow interaction

The momentum equation for the incompressible flow in the cavity reads

$$\rho\frac{\partial \mathbf{u}}{\partial t} + \rho(\mathbf{u}\cdot\nabla)\mathbf{u} = -\nabla p + \mu\nabla^2\mathbf{u} + \mathbf{j}\times\mathbf{B}, \tag{6.1}$$

where ρ is the fluid density, **u** is the fluid velocity, p is the pressure, μ is the dynamic viscosity, **j** is the electrical current density and **B** is the magnetic field strength. The body force term $\mathbf{j} \times \mathbf{B}$ accounts for the Lorentz force acting on the flow.

The electrical current density **j** follows from Ohm's law

$$\mathbf{j} = \sigma(\mathbf{E} + \mathbf{u} \times \mathbf{B}), \tag{6.2}$$

where **E** is the externally imposed electric field and σ is the electrical conductivity. In a saline solution with relatively low electrical conductivity, the induced current $\sigma(\mathbf{u} \times \mathbf{B})$ is much smaller than the imposed current $\sigma\mathbf{E}$ ($|\mathbf{u}||\mathbf{B}|/|\mathbf{E}| \approx 10^{-3}$). Since the electrical current density is primarily due to the imposed electric field, $\mathbf{j} = \sigma\mathbf{E}$, the electromagnetic forces are considered to be independent of the local flow velocity.

The electromagnetic forces should be of similar magnitude as the inertial forces to ensure a significant effect on the flow. The ratio of electromagnetic forces and inertial forces is expressed by the Stuart interactive number for electrohydrodynamics:

$$N = \frac{\sigma EBL}{\rho u^2}, \tag{6.3}$$

where, L and u are characteristic length and velocity scales for the inertial forces.

6.3 Physical modeling

6.3.1 Experimental setup

The experiment is conducted in a rectangular glass cavity, schematically shown in figure 6.1. The inner dimensions of the cavity are 0.8 $\times$ 0.65 $\times$ 0.035 m^3 (= H $\times$ W $\times$ T = height $\times$ width $\times$ thickness) and it is filled with a working fluid to a height h = 0.7 m. The working fluid is a solution of 10 wt% Na_2SO_4 in water. The density of the fluid is ρ = 1.10 $\times 10^3$ kg/m^3, the kinematic viscosity is ν = 1.27 $\times 10^{-6}$ m^2/s and the electrical conductivity is σ = 7.1 S/m (Wolf et al. 1986). The fluid is injected into the cavity through a square cross section nozzle of 0.6 m length with inner bore dimensions of $d \times d$ = 0.01 $\times$ 0.01 m^2 and outer dimensions of 0.02 $\times$ 0.02 m^2. The average flow velocity in the nozzle is $2 \times v_{in}$. The nozzle has two square outflow openings with size $d \times d = 0.01 \times 0.01$ m^2 in opposite sidewalls at the end of the nozzle, in planes perpendicular to the front and

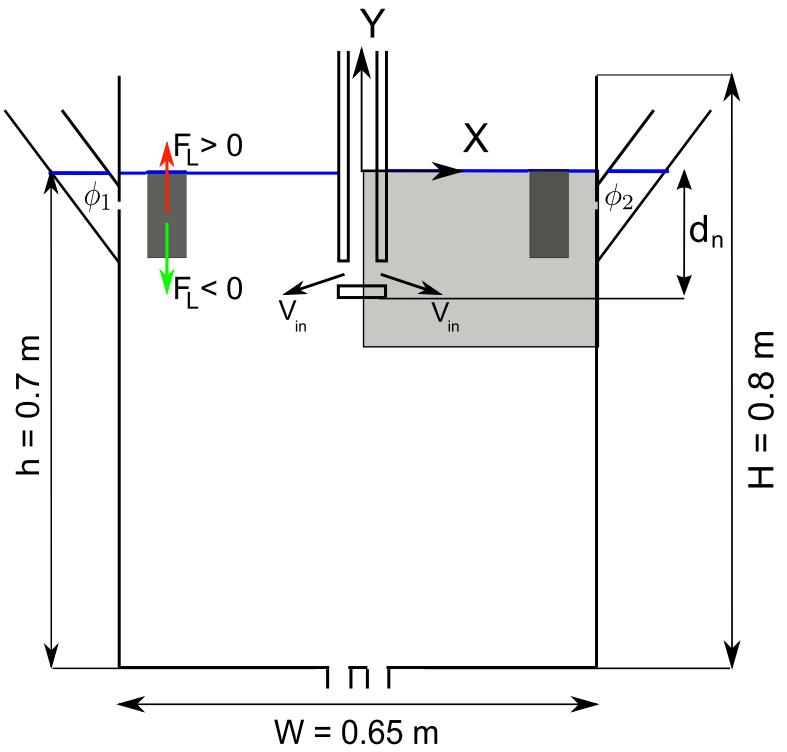

Figure 6.1: Schematic of the cavity with bifurcated nozzle. The inner dimensions of the cavity are H $\times$ W $\times$ T = 0.8 $\times$ 0.65 $\times$ 0.035 m^3. A solution of 10 wt% Na_2SO_4 in water flows into the cavity through a square cross section nozzle with inner dimensions of $d \times d$ = 0.01 $\times$ 0.01 m^2 and outer dimensions of 0.02 $\times$ 0.02 m^2. The nozzle is submerged to a depth d_n = 0.1 m. Water exits the nozzle through two square exit holes of $d \times d$ = 0.01 $\times$ 0.01 m^2 in opposite side walls of the nozzle. The cavity is filled up to h = 0.7 m and the outflow is through two holes of 0.04 $\times$ 0.035 m^2 in the bottom wall of the cavity. The light grey region in the top right corner is the field of view for the PIV measurements, the PIV light sheet is located in the z = 0 mid-plane. Near the top corners of the cavity, electrodes are placed which are electrically connected to the bulk fluid by a porous wall. The area of the porous walls is 0.03 $\times$0.03 m^2 and the top of the porous walls is located at y = -0.01 m. Next to the back wall 2 magnets, denoted by the dark gray regions, of 0.04 $\times$ 0.084 $\times$ 0.04 m^3 are placed, with the center of the magnet located at $x = \pm 0.25$m and y = -0.05 m. The z-component of the magnetic field strength (B_z) of one magnet is given in figure 6.2.

back wall of the cavity. The lower end of the nozzle is positioned at a depth

d_n = 0.1 m below the equilibrium free surface level. Liquid issues in the direction of the side walls of the cavity from each of these two openings, with a bulk velocity v_{in}.

Liquid flows out of the cavity through two 0.04 $\times$ 0.035 m^2 rectangular holes in the bottom wall of the cavity. The liquid is recirculated back to the nozzle by a pump and kept at a constant temperature (within 0.5°C) by means of an immersion cooler to guarantee a constant viscosity of the liquid.

A Cartesian coordinate system is defined with its origin located at the equilibrium position of the free liquid surface in the center of the cavity, see figure 6.1. The *x*-axis is parallel to the front wall of the cavity, and the *y*-axis is in the upward vertical direction. The free surface elevation, relative to $y = 0$, is denoted by η.

6.3.2 Electromagnetic forcing

Platinum electrode wires of 0.8 m length are placed in small compartments near the top corners of the cavity. The potential difference $\Delta\phi = \phi_1 - \phi_2$ between the electrodes was set to 50 V. This potential difference results in an electrical current of $I = 2.0$ A between the electrodes. The electrodes are physically separated from the cavity by a porous wall, such that electrical contact is made, but bubbles from electrolysis are prevented from entering the cavity. The area of the porous wall is 0.03 $\times$ 0.03 m^2 and the top of the porous wall is located at y = -0.01 m. The mean current density at the location of the porous walls is **j** = 2 $\times 10^3$ A/m^2 for an electrical current of $I = 2.0$ A.

Two NdFeB magnets with dimensions 0.04 $\times$ 0.084 $\times$ 0.04 m^3 are placed on the back wall of the cavity with the center of the magnets at $x = \pm 0.25$m and $y = -0.05$m. The magnetic field strength in the z-direction, $|B_z|$, is measured using a Hall-flux sensor. Figure 6.2 shows contour lines of $|B_z|$ in different z-planes in the cavity. A maximum field strength of 0.3 T occurs at the back wall on the side of the cavity at z = -0.0175 m. The magnetic field strength at the front wall inside the cavity is 0.07 T. The electrode/magnet configuration is positioned such that the resulting Lorentz forces at the locations of the magnets are symmetrical in the yz-plane. The electrical current between the electrodes can be reversed by changing the sign of the potential difference. This results in the possibility of an upward directed or a downward directed Lorentz force at the magnet positions, this is indicated as $F_L < 0$ or $F_L > 0$ in figure 6.1.

The quantities used to determine the value of the Stuart interactive number, N, are: $\sigma E = |\mathbf{j}| = 2\times 10^3$ A/m^2 at the position of the magnets, B is the magnetic field strength in the z-direction at the center position of the magnet ($x'' = 0$ and $y'' = 0$) in the z = 0 mid-plane of the caviy, B = 0.15 T, L is

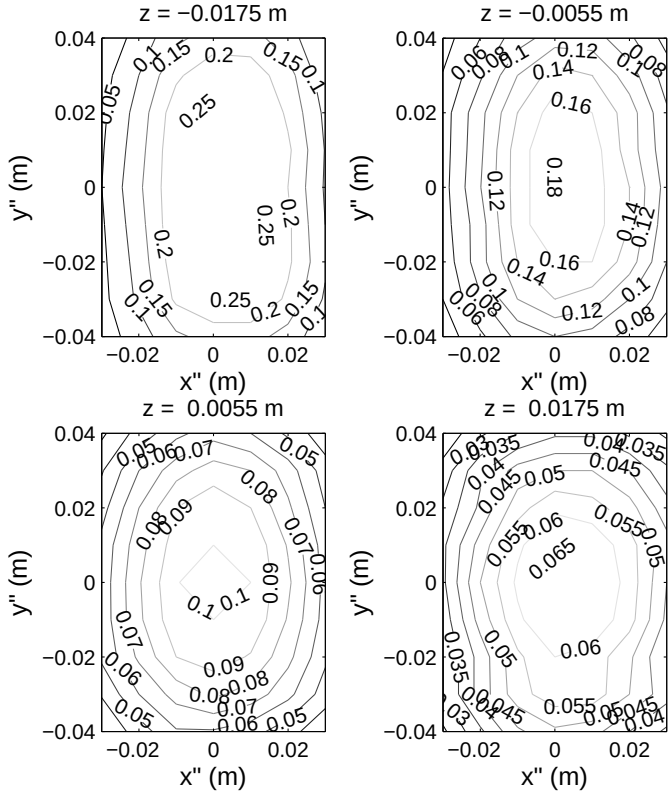

Figure 6.2: Magnetic field strength in the z-direction, $|B_z|$ (T) at the position of the magnet for different z-planes in the cavity. The center of the magnet is denoted by $x'' = 0, y'' = 0$.

the hydraulic diameter of the nozzle, ($L = d$ = 0.01 m), and the liquid density equals ρ = 1.10 $\times 10^3$ kg/m^3. The only parameter that is varied in the Stuart interactive number is the velocity, u, which is taken to be the inlet velocity v_{in}. The values chosen for the characteristic length scale and velocity scale result in significant electromagnetic forcing for Stuart numbers well below 1.

6.3.3 Measurement methods

Free surface tracking

Images of the capillary line at the front wall of the cavity are used for the tracking of the free surface. Since the thickness T of the cavity is small compared to the width W, it is assumed that the position of the capillary line gives a good representation of the location of the free surface. A Photron SA1 high-speed camera is used to collect images of the capilary line of the free surface with a resolution of 1024 $\times$ 512 pixels. The 32 GB internal memory of the camera allows for a total measurement time of 873 s. The field of view has size 0.08 $\times$ 0.04 m^2 and it is centered around a monitoring point at x = 0.175 m. The spatial resolution is 78 μm/pixel and the image of the capillary line is about ten pixels thick. The analysis of the images is carried out in Matlab, using a steepest gradient detection method that determines the upper and lower edge of the capillary line of the free surface. The mean of the upper and lower position of the maximum gradient is used as the free surface position.

PIV system

A Quantronix Darwin DUO 527-80-M laser and light sheet optics are used to produce a laser light sheet that enters the cavity through the bottom wall. The laser produces 27 mJ pulses at a wavelength of 527 nm and a repetition rate of 1000 Hz. Neutrally buoyant silver coated hollow glass spheres with a nominal diameter of 25 μm are used as seeding particles. The field of view has size 0.32 $\times$ 0.18 m^2 and is located in the top right corner of the cavity, as shown in figure 6.1. The light sheet is located in the mid-plane (z = 0) between the two broad walls and the light sheet thickness is less than 1 mm in the field of view. Particle images are recorded with an Imager HS pro 4M camera with a Nikon Nikkor 55 mm lens with $f^{\#}$ = 16. The camera is equipped with a 2016 $\times$ 2016 pixel CMOS-chip with a pixel size of 11 μm. This results in a spatial resolution of 0.17 mm/pixel. Velocity vectors are calculated based on cross correlation of interrogation areas of 32 $\times$ 32 pixels with 50 % overlap using Davis 8.1 PIV software.

6.4 Influence of electromagnetic forcing on the averaged flow dynamics

6.4.1 Pure electromagnetic forcing (Re = 0)

The applied Lorentz force is a body force, so there will be fluid flow in the cavity, even in the absence of inflow from the nozzle. Figures 6.3**a** and 6.3**b** show the mean velocity fields determined from the PIV measurements for a downward directed Lorentz force ($F_L < 0$) and an upwards directed Lorentz force ($F_L > 0$), respectively. In both cases there is no inflow from the nozzle. The flow fields induced by the Lorentz forces were practically stationary so that a short measurement time of 10 s was sufficient to determine the mean velocity field. The magnet position is indicated by the gray rectangle. The Lorentz force produces a stationary velocity field with velocities around 0.02 m/s at the magnet position.

6.4.2 Forced inflow: Lorentz forces are dominant

Figures 6.3**c**, **d** and **e** show the mean velocity fields from time-resolved PIV measurements with a duration of 106 seconds and with a frame rate of 100 fps. The inlet velocity is v_{in} = 0.2 m/s, giving rise to Re= 2×10^3 and N = 0.07. The three different cases **c**, **d** and **e** represent: no Lorentz force ($F_L = 0$), downward directed Lorentz force ($F_L < 0$) and upward directed Lorentz force ($F_L > 0$). The velocity magnitude in the region of the magnet is about 0.04 m/s.

Downward directed forcing ($F_L < 0$)

In figure 6.3**c** the Lorentz force is directed downward ($F_L < 0$). This results in a deviation from the mean velocity field without Lorentz force ($F_L = 0$) shown in figure 6.3**d**. A small recirculation zone is present near the top right corner which is also seen in the mean velocity field without forced inflow ($v_{in} = 0$) shown in figure 6.3**a**. The downward directed Lorentz force decreases the amount of fluid flowing towards the free surface as indicated by the weaker recirculation zone in the region above the jet. Comparing the mean velocity field for $F_L < 0$ to the mean velocity field for the case $F_L = 0$, it can be concluded that the general flow behavior is unchanged.

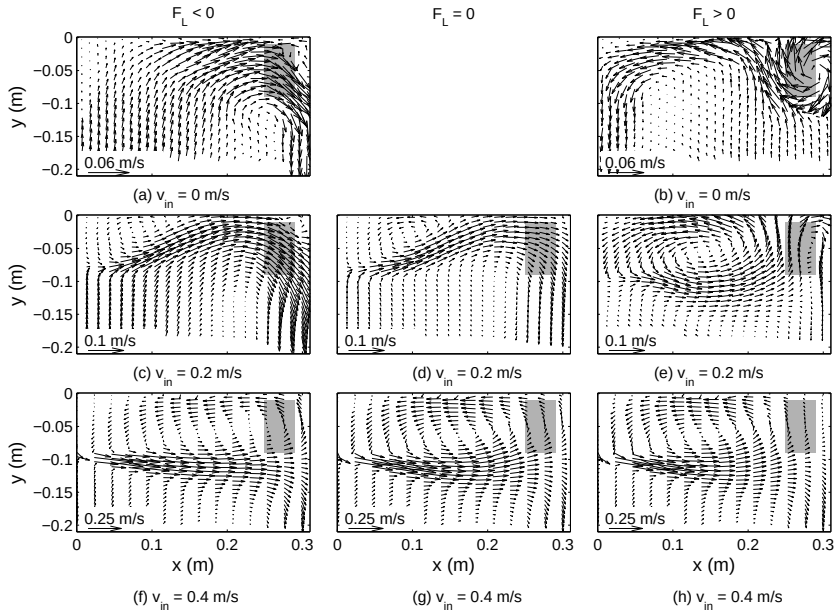

Figure 6.3: (a & b) Mean velocity fields with applied electromagnetic forcing, but without inflow from the nozzle. **(a)**The Lorentz force is pointing downward ($F_L < 0$), causing a clockwise directed mean flow. Between the magnet and the side wall a recirculation zone is present. **(b)** The Lorentz force is pointing upward ($F_L > 0$), causing an impingement point at the free surface above the magnet position. A recirculation zone is present between the magnet and the side wall. (**c**, **d** & **e**) Mean velocity fields from measurements with and without electromagnetic forcing. The inlet velocity v_{in} = 0.2 m/s (Re =2×10^3). The Stuart interactive number is N $\approx$ 0.07. (**f**, **g** & **h**) Mean velocity fields with and without electromagnetic forcing. The inlet velocity v_{in} = 0.4 m/s (Re= 4×10^3). The Stuart interactive number is N$\approx$ 0.02. The gray rectangles indicate the position of the magnet.

Upward directed forcing ($F_L > 0$)

In figure 6.3**e** the Lorentz force is directed upward, resulting in a strong recirculation zone in the region above the jet. Also, a recirculation zone near the top right corner is present, comparable to the recirculation zone in figure 6.3**b**. Comparing the mean velocity field in figure 6.3**e** to that in figure 6.3**d** it is seen that the global velocity pattern is changed significantly due to the electromagnetic forcing. Figures 6.4**a** and 6.4**b** illustrate these the differences.

Figure 6.4**a** shows the horizontal component of the velocity, 0.01 m below the free surface. It is seen that when $F_L > 0$, the velocity is negative in the whole domain, indicating a flow towards the nozzle. In figure 6.4**b** it is seen that when $F_L > 0$ the flow towards the free surface is up to v = 0.03 m/s at the magnet position.

6.4.3 Forced inflow: Inertial forces are dominant

Figures 6.3**f**, **g** and **h** show mean velocity fields determined from two time-resolved PIV measurements, each with a duration of 53 seconds and a frame rate of 200 fps. The inlet velocity is v_{in} = 0.4 m/s resulting in Re $= 4{\times}10^3$. As before, three cases are considered: no Lorentz force ($F_L = 0$), downward directed Lorentz force ($F_L < 0$) and upward directed Lorentz force ($F_L > 0$). In the cases with an applied Lorentz force, the Stuart interactive number is N = 0.02.

Downward directed forcing ($F_L < 0$)

Comparison of the mean velocity field for $F_L < 0$ in figure 6.3**f** to that for $F_L = 0$ in figure 6.3**g** shows that the mean velocity fields are qualitatively the same. In both cases the jet issues on the left at $y = -0.1$ m and splits at the side wall on the right at $x = 0.32$ m in an upward moving part and a downward moving part. Above the jets recirculation zones are present and the centers of the recirculation zones are located at the same location ($x = 0.16$ m and $y = -0.06$ m).

Profiles of the mean velocity component in the x- and the y-direction at y = -0.01 m have been plotted in figure 6.5. The x-position of the magnet is indicated by the gray band. When $F_L < 0$ a reduction of 20 % is seen in the horizontal component of the mean velocity, u, compared to the case with $F_L = 0$. The minimum in u has shifted towards the magnet location. Note that a negative velocity in the x-direction means that the flow is directed towards the nozzle. The reduction in the horizontal component of the velocity indicates that on average the shear forces along the free surface have decreased when $F_L < 0$. Extrapolation of these results indicates the possibility of electromagnetic flow control in this configuration and a reduction of the risk of entrainment.

Upward directed forcing ($F_L > 0$)

When the mean velocity field for $F_L > 0$ in figure 6.3**h** is compared to that for $F_L = 0$ in figure 6.3**g** it is seen that the center of the recirculation zone above the jet has moved from x = 0.16 m to x = 0.14 m. In figure 6.5**a** it is seen that

the mean velocity component in the horizontal direction at y = 0.01 m is not altered too much when the Lorentz force is directed upward. This indicates that on average the magnitude of the shear stress along the air/water interface is not altered and that the risk of entrainment is not affected in this case. The position of the maximum in the vertical component of the flow velocity, v, is largest in the region just to the left of the magnet, while with $F_L = 0$ the maximum in the velocity component towards the free surface is closer to the side wall. This shift in peak velocity indicates a larger deformation of the free surface on the left of the magnet position.

6.5 Free surface fluctuations

Time traces of the free surface elevation η with a duration of 873 seconds have been recorded at a monitoring point at x = 0.175 m. Figure 6.6 shows a part of these time traces with a duration of 75 s. The inlet velocity equals v_{in} = 0.4 m/s (Re = 4×10^3). For visualization purposes, the time traces have been smoothed by using a moving average filter with a window size of two seconds. For $F_L = 0$ and $F_L > 0$ clear oscillations of the free surface elevation are present with a free surface amplitude, defined as $A = (\eta_{max} - \eta_{min})/2$. Values of A are listed in table 6.1. Figure 6.7 shows power spectra of the recorded time traces. The dominant frequencies in the power spectra are also listed in table 6.1.

It is seen that the amplitude of the oscillation is damped and the frequency is reduced when $F_L < 0$ while the amplitude and the frequency are enhanced when $F_L > 0$. The reduction in free surface oscillation amplitude when $F_L < 0$ indicates a reduction in the peak velocities below the free surface and hence a delay in the risk of air entrainment. The increase in the free surface oscillation amplitude when $F_L > 0$ indicates an increase in the risk of entrainment. This illustrates that electromagnetic flow control is possible in this configuration, but one must be careful how to apply the Lorentz force.

Kalter et al. (2013) have reported time traces and power spectra of the free surface elevation in a very similar experimental setup. It was reported that three flow regimes could occur, depending on the inlet velocity and on the nozzle depth. Low frequency oscillations of the free surface elevation were found in the self-sustained oscillations regime and these free surface oscillations were linked to oscillations of the jet. In the present case, the low frequency oscillations are also found, as indicated by the peak in the power spectrum at $f = 0.041$ Hz for $F_L = 0$ in figure 6.7. Second and third harmonics are found in the spectrum for $F_L = 0$ at $f = 0.08$ Hz and $f = 0.12$ Hz. For $F_L < 0$ the peak in the power spectrum is reduced significantly and the peak is located at $f = 0.03$ Hz, indicating a reduction in the oscillation amplitude and

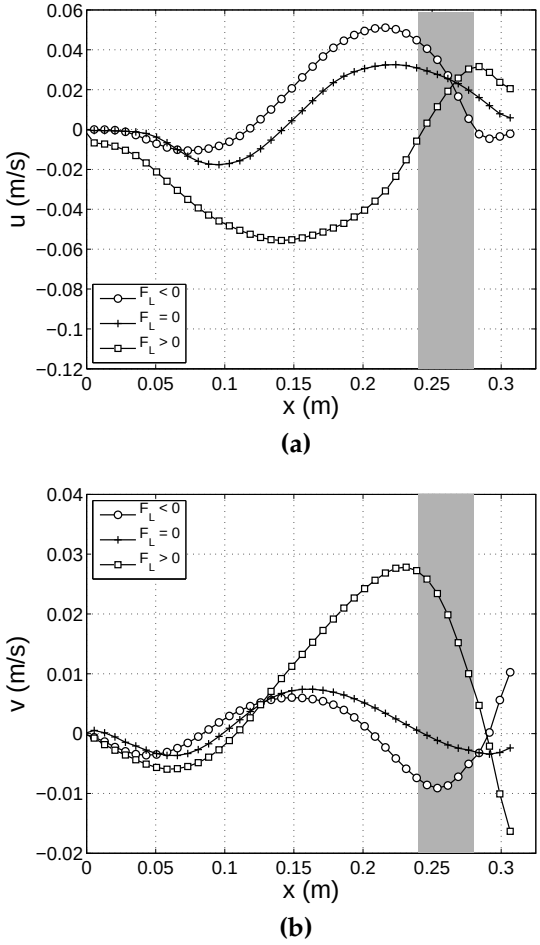

Figure 6.4: Horizontal component of the mean velocity u (top) and vertical component of the mean velocity v (bottom) at y = -0.01 m. The inlet velocity is v_{in} = 0.2 m/s giving rise to Re= 2×10^3, N = 0.07. The gray band indicates the x-position of the magnet.

frequency of the jet. For $F_L > 0$ the peak in the power spectrum is enhanced and located at $f = 0.047$ Hz, indicating an enhancement in the oscillation amplitude and frequency of the jet. Also second and third harmonics in the oscillation frequency are found when $F_L > 0$.

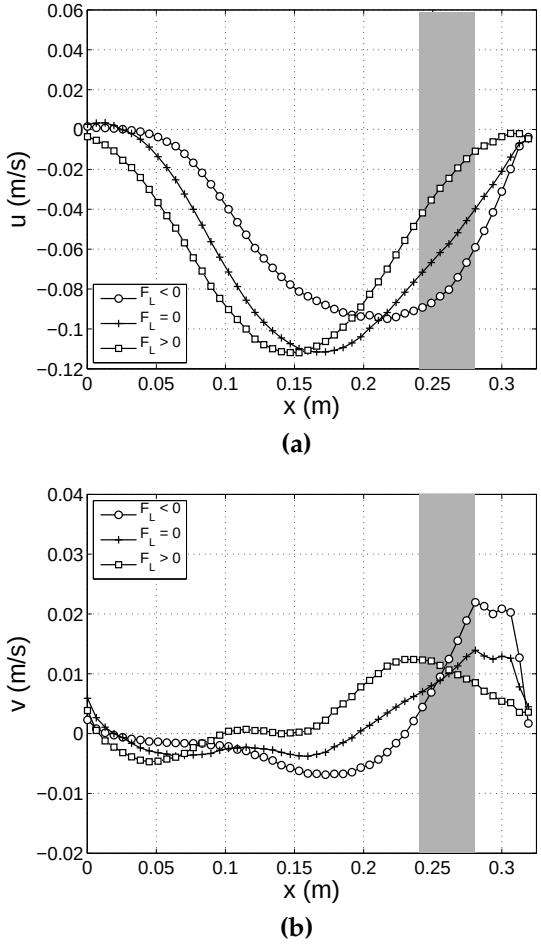

Figure 6.5: Horizontal component of the mean velocity u (top) and vertical component of the mean velocity v (bottom) at y = -0.01 m. The inlet velocity is v_{in} = 0.2 m/s giving rise to Re= 2×10^3, N = 0.02. The gray band indicates the x-position of the magnet.

6.6 Proper orthogonal decomposition

A proper orthogonal decomposition (POD) is performed on the sets of instantaneous velocity fields for Re= 4×10^3. In POD the velocity is split in a time dependent (chrono) part $a_n(t)$ and a space dependent (topo) part $\phi_n(\mathbf{x})$

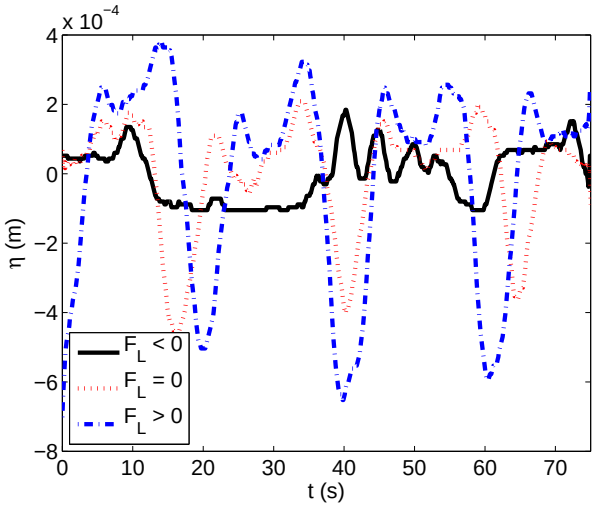

Figure 6.6: Time traces of the free surface elevation at a monitoring point located at x = 0.175 m with v_{in} = 0.4 m/s (Re = $4{\times}10^3$). When the Lorentz force is directed downward ($F_L < 0$, solid line), the amplitude of the free surface elevation is about 0.5×10^{-4} m. Without Lorentz force ($F_L = 0$, dotted line) the amplitude of the free surface elevation is about 3×10^{-4} m and when the Lorentz force is directed upward ($F_L > 0$, dash-dotted line), the amplitude of the free surface instabilities is about 4.5×10^{-4} m.

(Holmes et al. 1996, Semeraro et al. 2012, Sirovich 1987)

$$u(\mathbf{x},t) = \sum_{n=0}^{N} a_n(t)\phi_n(\mathbf{x}), \tag{6.4}$$

	A (mm)	f_{TS} (Hz)	f_{POD} (Hz)
$F_L < 0$	0.5	0.030	0.027
$F_L = 0$	3	0.041	0.046
$F_L > 0$	4.5	0.047	0.050

Table 6.1: Amplitude A and frequency f_{TS} of the free surface oscillation at a monitoring point at x = 0.175 m for the three different forcings (Re= $4{\times}10^3$, N = 0.02). Dominant frequency F_{POD} from the power spectrum of the first chrono mode of the POD.

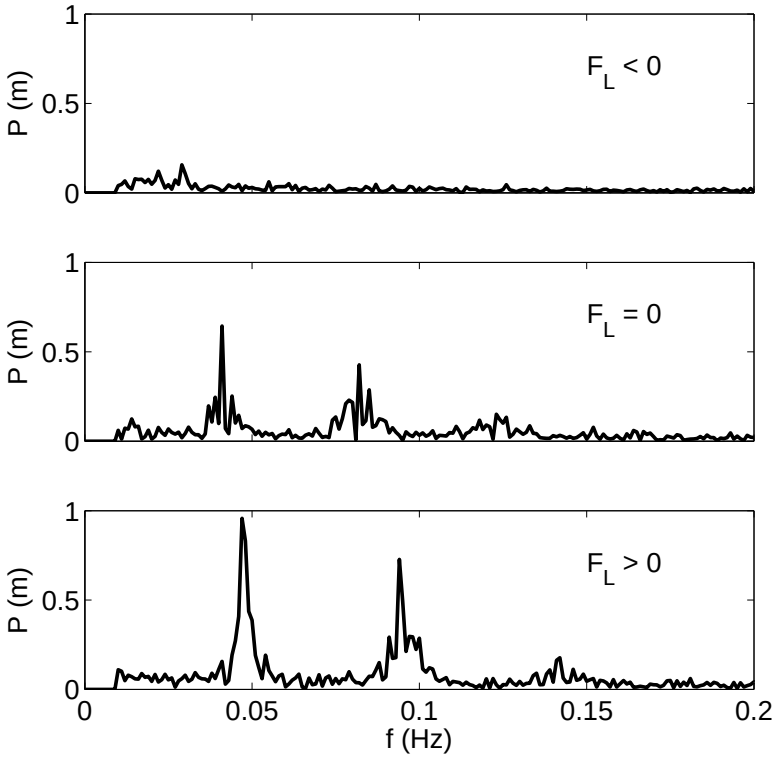

Figure 6.7: Power spectra of the free surface elevation recorded at a monitoring point at x = 0.175 m. The inlet velocity is v_{in} = 0.4 m/s (Re= 4×10^3, N= 0.07). The peaks are located at f = 0.030 Hz for $F_L < 0$, f = 0.041 Hz for $F_L = 0$ and f = 0.047 Hz for $F_L > 0$.

where n denotes the mode number and N is the number of PIV snapshots used to calculate the POD (which is equal to 425 in this case). The POD is determined using the standard Davis 8.1 software.

POD energies

The zeroth POD mode is the mean velosity field that was already presented in figure 6.3. Figure 6.8**a** shows the energy per mode as a fraction of the total kinetic energy for modes 1 to 50. Figure 6.8**b** shows the cumulative energy

distribution for the 425 eigenmodes.

When $F_L < 0$, the energy contained in the first mode is 20 % of the total kinetic energy. When $F_L = 0$ the energy in the first mode is 42 %. When $F_L > 0$ the energy in the first mode is 56 %. Recently, Podvin and Sergent (2012) applied the POD to PIV snapshots of Raleigh-Bénard convection and they showed that the first mode of the POD is related to large-scale structures in the flow. This interpretation of the first mode is adopted here as well, and figure 6.9 shows the first spatial mode of the POD for the three different forcings. The first modes for the different forcings are qualitatively the same. The two extreme positions of the oscillating jet can be distinguished by the positions of two recirculation zones in the velocity fields. The first recirculation zone center in all three cases is located around $x = 0.08$ m and $y = 0.05$ m this recirculation zone is connected to the extreme position of the jet towards the nozzle location. The second recirculation zone center in all three cases is located around $x = 0.22$ m and $y = 0.1$ m this recirculation zone corresponds to the position the jet is in when it flows downwards along the narrow side wall. The small fraction of kinetic energy in the first POD mode for the downwards directed Lorentz force in combination with this interpretation of the first POD mode indicates that the energy in the large-scale oscillation has decreased considerably. This illustrates the suppression of the oscillations due to the applied Lorentz force.

The fractions of the total kinetic energy contained in the first POD modes are high, compared to that for other structured flows like Rayleigh-Bénard convection in varying aspect ratio cells (Podvin and Sergent (2012), Verdoold et al. (2009)), the flow of a confined jet with co-flow (Semeraro et al. (2012)) or the flow from an array of impinging jets (Geers et al. (2006; 2005)). Table 6.2 summarizes the fractions of the kinetic energy in the first few modes for the present work and for the above mentioned works. From table 6.2 it can be concluded that when $F_L = 0$ and when $F_L > 0$, the fraction of the kinetic energy contained in the first few POD modes is much higher than in flow situations like Rayleigh-Bénard convection and an array of jets. However, when $F_L < 0$, the fraction of energy contained in the low modes of the POD is much lower and comparable to the energy contained in the first mode for Rayleigh-Bénard convection.

Temporal modes

Figure 6.10**a** shows the first chrono-mode $a_1(t)$ for the three cases (related to the most energetic spatial mode $\phi_1(\mathbf{x})$). The power spectra of the time traces of the first chrono-mode are shown in figure 6.10**b**.

In figure 6.10**a** clear oscillations of $a_1(t)$ are seen with different oscillation

Modes	1	1-3	1-4	1-10
Present case $F_L < 0$	20	26	28	35
Present case $F_L = 0$	42	55	57	63
Present case $F_L > 0$	56	72	73	76
Hexagonal jet array (Geers et al. 2005)				24
In-line jet array (Geers et al. 2005)				34
Rayleigh-Bénard (Ra = 4×10^7 (Verdoold et al. 2009))		27		
Rayleigh-Bénard (Ra = 5.9×10^8 (Verdoold et al. 2009))		29		
Rayleigh-Bénard (Ra = 6×10^8 (Podvin and Sergent 2012))	28		46	
Rayleigh-Bénard (Ra = 6×10^9 (Podvin and Sergent 2012))	15		47	
Rayleigh-Bénard (Ra = 10^{10} (Podvin and Sergent 2012))	13		45	
Confined jet with co-flow (Semeraro et al. 2012)	4.5			22

Table 6.2: Percentages of total kinetic energy in the first few POD modes for comparison of the results presented in this work with results from other flow situations with highly structured flows.

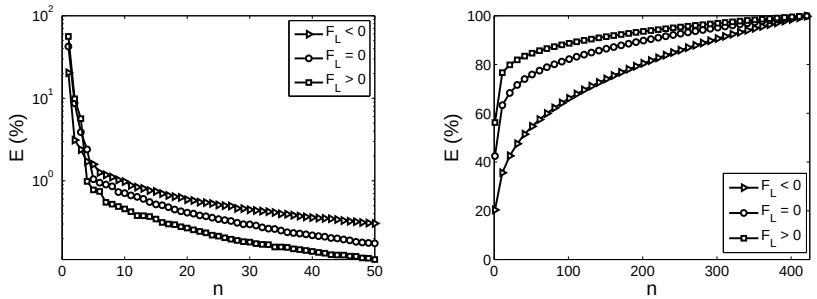

Figure 6.8: (a) Energy contained in POD modes 1 to 50 shown as a percentage of the total kinetic energy. **(b)** Cumulative energy as a percentage of the total kinetic energy.

frequencies for the three different forcings. Peaks are found in the power spectra at f_{POD} = 0.027 Hz when $F_L < 0$, f_{POD} = 0.046 Hz when $F_L = 0$ and f_{POD} = 0.050 Hz when $F_L > 0$. The values found for the oscillation frequencies are in reasonable agreement with the frequencies found for the free surface fluctuations (f_{TS}), as presented in figure 6.7 and in table 6.1.

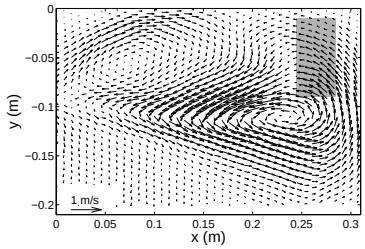

(a) $F_L < 0$,

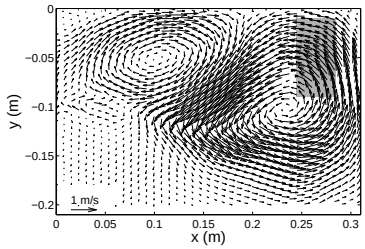

(b) $F_L = 0$

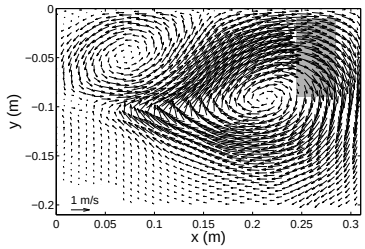

(c) $F_L > 0$

Figure 6.9: The first spatial modes, ϕ_1, of the POD for the three different forcings (Re= 4×10^3, N = 0.02). The gray rectangle indicates the magnet position.

6.7 Kinetic energy distribution

The free surface fluctuations reported in section 6.5 and the POD analysis in section 6.6 indicate that large scale, low frequency oscillations are present in the cavity flow. The large scale oscillations will affect turbulence statistics when conventional Reynolds averaging is performed. Hussain and Reynolds (1970) proposed a triple decomposition of the velocity components for

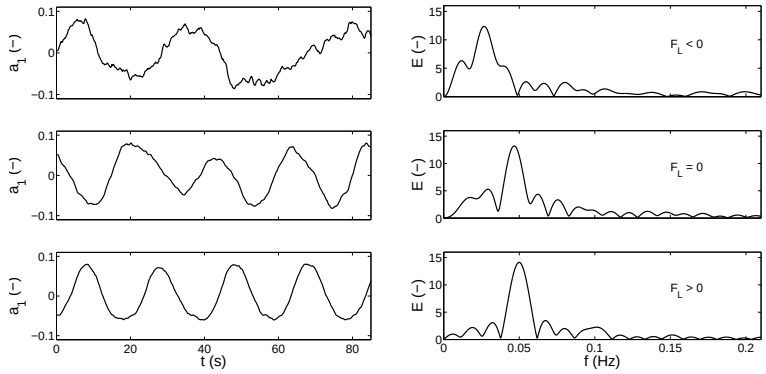

Figure 6.10: (a) Time series for the first chrono-mode of the POD, $a_1(t)$, for the three different forcings with $v_{in} = 0.4$ m/s (Re = $4{\times}10^3$, N = 0.02). **(b)** Power spectra of the chrono-modes $a_1(t)$. Frequency peaks are found at f_{POD} = 0.027 Hz ($F_L < 0$), f_{POD} = 0.046 Hz ($F_L = 0$) and f_{POD} = 0.050 Hz ($F_L > 0$). The values of the frequency peaks are in reasonable agreement with the frequencies found for the free surface fluctuations, f_{TS}.

turbulent flows exhibiting periodic fluctuations. The triple decomposition is used to differentiate between velocity fluctuations due to turbulence and fluctuations due to the large-scale periodicity. The triple decomposition of the horizontal velocity component is

$$u = \bar{u} + \tilde{u} + u' \tag{6.5}$$

where u is the instantaneous velocity component in the horizontal direction, $\bar{u}$ is the mean velocity, $\tilde{u}$ is the velocity associated with the long term oscillations and u' is the velocity associated with the turbulent fluctuations. The total fluctuation $\tilde{u} + u'$ is calculated by subtracting the mean velocity $\bar{u}$ from the instantaneous velocity u. The oscillating velocity $\tilde{u}$ is subsequently obtained by applying a moving average filter to the total fluctuation $\tilde{u} + u'$ with a filter width of 0.5 second. The filtered signal is then subtracted from the total fluctuation to obtain the velocity fluctuation u'. The filter width of 0.5 second is around 1/40th of the period of the large-scale oscillation, making sure that the large-scale oscillation is well resolved by the moving average filter. From the decomposed velocities, the kinetic energy associated with turbulence can

be calculated from

$$k_{turb} = \frac{1}{2}[\overline{u'^2} + \overline{v'^2}], \tag{6.6}$$

and the kinetic energy associated with the long term oscillation can be calculated from

$$k_{osc} = \frac{1}{2}[\overline{\tilde{u}^2} + \overline{\tilde{v}^2}]. \tag{6.7}$$

The two dimensional surrogates for the kinetic energy are used since the PIV measurements were performed with a two component system.

Figures 6.11**a**, **b** and **c** show the partial distribution of the turbulence kinetic energy k_{turb}. It is clear that a peak in k_{turb} is located near the jet exit region with maximum values of approximately $k_{turb} = 6 \times 10^{-2}$ m^2/s^2 in all three cases. When moving in the streamwise direction the jet shear layer spreads while turbulence levels decrease. This is due to the entrainment of low velocity ambient fluid. Due to the limited spatial resolution of the PIV measurements in the jet region, the jet shear layers can not be resolved in detail. Nevertheless, it is clear from figure 6.11**a**, **b** and **c** that the electromagnetic forcing does not have a significant influence on the turbulence kinetic energy k_{turb}.

Figures 6.11**d**, **e** and **f** show the kinetic energy associated with the long term oscillations, k_{osc}. The maximum value of k_{osc} is much lower than that of k_{turb}, but the kinetic energy k_{osc} is spread over the entire field of view, thus contributing significantly to the total kinetc energy in the cavity. The amount of energy contained in the oscillation, loosely defined as the integral of k_{osc} over the field of view, is three times lower when $F_L < 0$ (figure 6.11**d**) compared to the situation with $F_L > 0$ (figure 6.11**f**). This reduction in kinetic energy is in agreement with the results from the POD in section 6.6, where also the fraction of kinetic energy in the first spatial mode $\phi_1(\mathbf{x})$ is about three times lower for the case with $F_L < 0$ compared to the case with $F_L > 0$. It is also seen in figure 6.11**d** that the values of k_{osc} are reduced near the free surface, indicating a stabalizing effect of the Lorentz force on the fluctuations near the free surface. This reduction in the kinetic energy near the free surface results in the reduction of the free surface elevation η as reported in section 6.5, indicating again the possibility of the use of the Lorentz force as a flow control device.

6.8 Conclusions

Instantaneous velocity fields and free surface elevations were measured in the flow in a cavity with a submerged bifurcated nozzle for jet Reynolds numbers

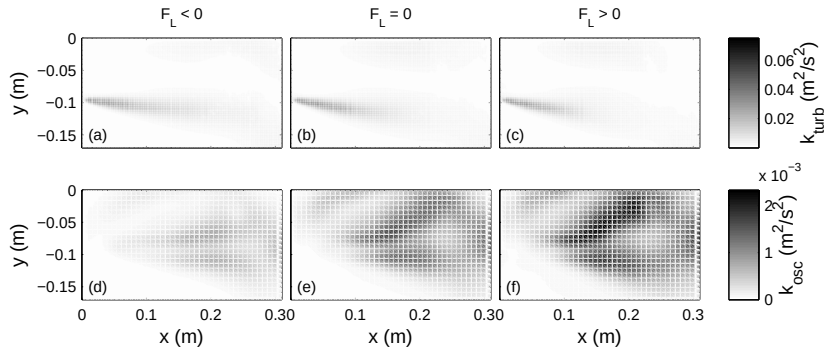

Figure 6.11: a, **b** & **c** Profiles of the turbulence kinetic energy k_{turb}. **d**, **e** & **f** Profiles of the kinetic energy associated with the large-scale oscillations k_{osc}. The inlet velocity is $v_{in} = 0.4$m/s (Re= 4×10^3, N = 0.02).

of Re= 2×10^3 and Re= 4×10^3. The working fluid is an electrically low conducting saline solution that experiences an electromagnetic forcing due to the combined effects of an externally applied magnetic field and an imposed electrical current.

When the jet Reynolds number is Re= 2×10^3, the Stuart number is N = 0.07. In this case the velocity fields are stationary. When the Lorentz force is applied the flow patterns are dominated by electromagnetic forces.

With a jet Reynolds number of Re= 4×10^3 and without an applied Lorentz force (N = 0), self-sustained jet oscillations with a frequency of f = 0.04 Hz occur in the cavity. When the Lorentz force is applied, N = 0.02, and inertial forces are in the same order of magnitude as the electromagnetic forces. A downward directed Lorentz force ($F_L < 0$) counteracts the force needed to sustain the self-sustained jet oscillation and hence the jet oscillation amplitude and frequency are strongly reduced. An upward directed Lorentz force ($F_L > 0$) has the opposite effect and increases both the amplitude and the frequency.

A proper orthogonal decomposition has been performed to investigate the distribution of kinetic energy over the different sized structures in the flow. Due to the strong oscillation of the jet for $F_L = 0$ and for $F_L > 0$, the fraction of the kinetic energy contained in the low POD modes (which are connected to the large-scale flow structures) is high compared to the case with $F_L < 0$, where the oscillations are significantly damped. These energies are also high compared to the energies contained in low POD modes in several other well structured flow situations.

A triple decomposition of the velocity components has been carried out to make a distinction between the energy contained in the large scale fluctuations k_{osc} and in turbulence k_{turb}. The distribution of k_{turb} is not altered due to the Lorentz forcing. The kinetic energy contained in the long term oscillations k_{osc} is altered significantly depending on the Lorentz force configuration. For $F_L < 0$, the maximum value in k_{osc} and the amplitude of the spread in k_{osc} are reduced significantly.

Chapter 7

Conclusions and outlook

In this chapter we present the main conclusions regarding the self-sustained oscillations, electromagnetic forcing and temperature distributions in the studied experimental setups. In the first three sections the research questions raised in section 1.2 are addressed one by one. In the final section, a discussion about the applicability of the experimental results for continuous casting is presented and possibilities for further experimental research are highlighted.

7.1 The mechanism of self-sustained jet oscillations

The physical mechanism leading to the self-sustained jet oscillations was studied in chapters 2 and 5 for the flow of two jets from a bifurcated nozzle into a thin cavity and for the flow of a single jet into a cavity, respectively. In this section we first discuss the mechanism of the self-sustained jet oscillations by analyzing the case of a single jet issuing into a thin cavity, followed by conclusions for the case with two jets emerging from a bifurcated nozzle.

In the startup phase of a single jet issuing from a vertical nozzle into a thin cavity, the jet flows symmetrically to the bottom of the cavity. At the bottom of the cavity, the high velocity jet fluid moves to the left or to the right, this is a random process. In our further description, the fluid moves to the right. Once the fluid reaches the right wall, it flows upward, forming a recirculation zone on the right side of the jet. In the center of this recirculation zone, a low pressure region is present, which draws the jet towards this region. The jet is drawn upward until the center of the jet hits the side wall, at which point it splits into two parts, one part flowing upward, filling the recirculation

zone on the right side of the jet and one part flowing downward, forming a recirculation zone on the left side of the jet. A low pressure zone is now also present in the center of the left recirculation zone, which grows in strength. At a certain moment the recirculation zone on the left becomes stronger than the one on the right and it draws the jet towards the left side of the cavity. This continues until the jet impinges the left side wall. Now the reverse process starts, until the jet bends back towards the right wall again. This process continues indefinitely, resulting in self-sustained jet oscillations.

In the case of two jets issuing from a bifurcated nozzle, the same mechanism as for the single jet causes the jet oscillations. However, in this case there is also a strong interaction between the recirculation zones alongside the left jet and the recirculation zones alongside the right jet. This leads to an imbalanced system in which at any given point in time, two "strong" recirculation zones and two "weak" recirculation zones are present.

For the bifurcated jet it was observed that a cross-flow through the gaps between the nozzle and the front and back wall of the cavity is necessary for the self-sustained oscillations to exist. Although not tested, we believe that this observation also holds for single jet flows.

In chapter 3 the width-to-thickness ratio W/T of the cavity with a bifurcated nozzle is considered. When W/T becomes smaller than 10, the self-sustained oscillations disappear. The disappearance of the self-sustained oscillations is due to a transition from semi two dimensional flow, where recirculation zones are confined between the front and back walls, to three dimensional flow. The critical width-to-thickness ratio is predicted by taking into account the known spreading angle of $\theta = 12^\circ$ of a turbulent jet. Self-stained jet oscillations exist when $W/T \gtrsim (\tan(\theta/2))^{-1} \approx 10$.

7.2 Temperature distribution in a cavity due to self-sustained jet oscillations

Chapter 4 presents heat transfer characteristics and transient temperature distributions in the cavity with flow from a submerged bifurcated nozzle. The average convective heat transfer coefficient of the water in the cavity to the cooled wall was found to scale with the flow rate into the cavity as $h_{conv} \propto \phi_v^{0.8}$.

The oscillating jet leaves a thermal imprint at the cooled wall. Hot spot formation is present at the location where the shear layers of the jet reach the wall, and a low temperature region is present at the wall in the center of the recirculation zone between the jet and the air/water interface. The cold spot in the center of the recirculation zone oscillates along with the jet oscillation.

This means that the heat transfer is not uniform over the cavity wall and that the local heat transfer is not constant in time.

7.3 Effect of electromagnetic forcing on self-sustained jet oscillations

In chapters 5 and 6, electromagnetic forcing was applied to the flow in order to influence the self-sustained jet oscillations for a single jet issuing vertically into a thin cavity, and for two jets issuing from a bifurcated nozzle, respectively.

In the case of a single jet, using three magnets, the applied Lorentz force can be in an up-down-up configuration, or it can be in a down-up-down configuration.

In the up-down-up configuration, the Lorentz force in the jet region is directed downward (in the same direction as the jet movement) and the Lorentz force on the left and right side of the jet is directed upward. The electromagnetic forcing alongside the jet adds to the momentum in the recirculation zones that are present alongside of the jet. When the jet deflects to one side, the Lorentz force increases the speed with which the recirculation zone is formed and when the recirculation zone on the other side is formed, the momentum due to the Lorentz force also adds to the flow in this recirculation zone. This means that the formation of the recirculation zones is faster, leading to a higher jet oscillation frequency. For sufficient electromagnetic forcing, the oscillation frequency grows with the square root of the applied forcing.

In the down-up-down forcing configuration, the Lorentz force in the jet region is directed upward (opposite to the jet direction) and the Lorentz forcing alongside the jet acts downward. The momentum from the Lorentz force is opposite to the momentum of the recirculation zones on the left and right sides of the jet. When the forcing is of sufficient strength, the formation of the recirculation zones can be prevented and hence the jet oscillation can be prevented. A critical Stuart number was found, above which the jet oscillations disappear.

In the case with two jets issuing from a bifurcated nozzle, as discussed in chapter 6, the applied Lorentz force acts perpendicularly to the movement of the jet oscillation. The location where the Lorentz force is applied is between the jet and the air/water interface, near the narrow side wall, and it can be directed upward or downward.

When the Lorentz force is directed upward, the momentum due to the Lorentz force adds to the formation of the recirculation zone above the jet and hence the formation of this recirculation zone is accelerated. This happens to

the jets on both sides of the nozzle, leading to a higher oscillation frequency and also to an increased amplitude of the free surface fluctuations.

When the Lorentz force is directed downward, it acts against the jet movement, leading to a slower formation of the recirculation zones above the jets on both sides of the nozzle. This leads to a lower oscillation frequency of the jet. The velocities below the free surface are suppressed, which leads to a decreased amplitude of the free surface fluctuations.

7.4 Outlook

7.4.1 Applicability of the experimental data for continuous casting

Due to the use of water, rather than liquid metals, as a working fluid, the experimental results presented in this thesis cannot directly be used to design or optimize actual steel casters. However, the acquired data is indispensable for the validation and optimization of numerical models, the latter being capable of predicting the real flow dynamics, heat transfer and influence of electromagnetic forcing in the mould of an actual continuous casting machine.

Ideally, one would like to validate numerical models with measurements in the actual casting process, but these measurements are usually difficult to perform, expensive and inaccurate. The main reason to use results from water model laboratory experiments as validation data for numerical models is that it is relatively simple and cheap to perform these measurements, and the accuracy of the laboratory experiments is high. Requirements for improving the numerical model, based on water model laboratory experiments, are that the experiments capture the relevant physics and that the experimental setup is geometrically representative of the industrial device.

In the present chapter we sketch a picture of the applicability of the obtained experimental results for validation of numerical models in the field of continuous casting, taking into account these two requirements.

Fluid dynamics

For a fluid dynamical similarity between the experimental model and the actual casting mould, Reynolds and Froude number similarity are required, and since the kinematic viscosities of liquid steel and of water are comparable, a close to 1:1 scaled model of the mould is required. However, when the flow is fully turbulent the requirement of Reynolds similarity can be relaxed.

In the present work, a 1:2 scaled down model of the mould was employed, so full Reynolds number similarity in combination with full Froude number

similarity is not reached. For further simplification, a simplified submerged bifurcated nozzle geometry is used, and no slag layer and solidifying shell are included. This indicates that results from the experiments can be indicative for the flow behavior in the mould, but a detailed prediction of the flow behavior, including heat transfer and solidification, in the actual casting mould is not possible based on the experimental results only.

On the other hand, the usability of the experimental results as validation data for numerical models is large, since detailed measurements of the free surface dynamics and of the sub-surface flow behavior have been reported and a detailed database with experimental results is available. The behavior of the large scale fluctuations, like the jet oscillation (chapter 2) is captured in detail and can be used as robust validation data. In hindsight, a minor set back of the performed experiments is that the flow from the nozzle is not closely related to the flow from nozzles that are actually used in continuous casting. Due to the abrupt corners at the end of the nozzle used in the present experiments, high Reynolds stresses and flow separation occurs in the flow. In the industrial process, lots of effort has been put into preventing flow separation and high Reynolds stresses by designing nozzles with smooth curvatures. In numerical models, it is difficult to capture the high Reynolds stresses faithfully, due to the occurrence of small turbulent length scales which need to be resolved using a fine numerical grid.

The single jet case (as presented in chapter 5) is easier to capture numerically, since no flows through abrupt corners are present in this case. This leads to a reduction in the local shear stresses in the flow, and hence to a more generic test case where the flow dynamics are still representative for the flow in the casting mould.

Heat transfer

The main physical parameter influencing the applicability of the results from the heat transfer measurements (as presented in chapter 4) for the validation of heat transfer simulations in liquid steel is the Prandtl number. For water Pr = O(10) and for liquid steel, Pr = O(0.1). In both the flows in the experiment and in the actual caster, forced convection heat transfer is dominant over natural convection and conduction, and as such, the Prandtl dissimilarity does not impose great problems.

In direct numerical simulation studies of heat transfer in the presence of forced convection, the smallest length scale that needs to be solved for the heat transfer, the Batchelor scale λ, scales with the Kolmogorov length scale, η, as $\lambda \sim \eta \mathrm{Pr}^{-0.5}$. This means that in the case of water the smallest length scale to be solved is $\lambda \sim 0.3\eta$, while in the steel case this is $\lambda \sim 10\eta$. This

means that heat transfer dynamics are easier to solve in liquid metals than in water, due to the much higher diffusion of heat in liquid metals than in water. Consequently, our results obtained in water are more difficult to use as validation for numerical simulations than results that would have been obtained in low Prandtl number fluids.

In the experiment we do not take into account the heat transfer due to the presence of the solidified strand. In the strand heat transfer due to conduction and phase change of the metal play a large role. Also, the strand roles along the cooling plates of the mould, forming a gap. The nature of this gap fully determines how heat is transferred from the steel towards the cooling wall. A last factor influencing the local heat transfer is the specific composition of the steel, which influences local conduction and phase change characteristics.

In conclusion we can say that our results can be used for a proper validation of the forced convection flow, but due to severe simplifications in our experiments there is not a close resemblance to the actual heat transfer problem in the continuous casting mould.

Electromagnetic forcing

In chapters 5 and 6, the electrical conductivity of the water was increased by adding 10 wt.% sodium sulfate, and a Lorentz force was applied by means of a static electrical field in conjunction with a static magnetic field. This results in a Lorentz force $\mathbf{F}_E = \sigma \mathbf{E} \times \mathbf{B}$ at a fixed position, and with a fixed direction.

In the flow of liquid steel, no fixed electrical field can be applied. Therefore, and due to the much larger electrical conductivity of the steel ($\sigma_{steel} \approx 10^5$ S/m) as compared to the sodium sulfate solution ($\sigma_{salt_water} \approx 10$ S/m), the magnetic part of the Lorentz force, $\mathbf{F}_M = \sigma \mathbf{u} \times \mathbf{B} \times \mathbf{B}$, is dominant. This Lorentz force is opposite to the local direction of the flow through the magnetic field. This means that in a liquid steel flow, magnets produce a local Lorentz force that can be seen as an obstacle which deforms the local flow pattern when the magnetic field is sufficiently strong.

The differences in the application of the Lorentz force lead to the conclusion that design and optimization of the actual casting mould cannot be based on the present experimental results.

Now, how are the presented experimental results of benefit in the validation of numerical models of pure MHD flows? In the numerical modeling, the modelled Lorentz force reads

$$\mathbf{F}_L = \mathbf{J} \times \mathbf{B} \tag{7.1}$$

where **J** is the electrical current density, which is

$$\mathbf{J} = \sigma(\mathbf{E} + \mathbf{u} \times \mathbf{B}) = \sigma(-\nabla\psi + \mathbf{u} \times \mathbf{B}), \tag{7.2}$$

where in the second part of equation 7.2 the electrical field **E** has been replaced by the negative gradient of the electrical potential ψ. Due to conservation of charge $\nabla \cdot \mathbf{J} = 0.$, such that

$$\nabla^2\psi = \nabla \cdot (\mathbf{u} \times \mathbf{B}). \tag{7.3}$$

In the cases presented in chapters 5 and 6, the magnetic force is negligible, so $\nabla \cdot \mathbf{J} = 0$ reduces to $\nabla^2\psi = 0$, and in the numerical setup $\nabla\psi$ is dominated by the applied boundary conditions for the electrical potential. These boundary conditions state that at the positions of the electrodes at the wall the electrical current density perpendicular to the wall is $\mathbf{J}_\perp \neq 0$ whereas $\mathbf{J}_\perp = 0$ at all the other boundaries. The electrical current density parallel to the walls is always $\mathbf{J}_\parallel = 0$. In the numerical model, still equation 7.3 is solved however.

In the case of pure magnetic forcing, again conservation of charge is required, so again,$\nabla^2\psi = \nabla \cdot (\mathbf{u} \times \mathbf{B})$ at all positions in the flow. Now the electrical potential is not dominated by the boundary conditions, but it follows completely from the induced electrical currents due to the flow of charge carriers through the magnetic field. The boundary conditions in this case reduce to $\mathbf{J}_\perp = \mathbf{J}_\parallel = 0$ at all walls of the mould.

Since in the flows with sodium-sulfate solution and with liquid steel, the same set of equations is solved for the Lorentz force, validation of a numerical model against the present experimental results is undoubtedly valuable.

For a further improved description of MHD flows, one needs to consider whether the increase in electrical conductivity, when going from a saline solution to liquid metal, causes a change in the dominant physical processes. For instance Hartmann layers may become important for high conductivity liquids. To investigate the influence of the changing physics when going to liquid metals, the MHD models need to be validated further using results from measurements of flows in which MHD effects play a large role.

7.4.2 Research opportunities

In the remainder of this chapter we look at two possibilities for further experimental investigation of flows with MHD effects. The first is the flow of a high conductivity acidic solution through a strong magnetic field, which is an intermediate step towards MHD flows, using a transparent liquid as a working fluid. Secondly, we look at the possibilities for measurements with liquid metals for full MHD flows.

High Stuart number flows in transparent liquids

To be able to use optical techniques in MHD flows, we need transparent liquids with an electrical conductivity that is much higher as compared to that of the saline solution used in the present experiments. Andreev et al. (2013) introduced high Stuart number flows in transparent liquids, using a sulfuric acid solution with electrical conductivity of $\sigma = 87$ S/m, (which is about ten times higher than the electrical conductivities encountered in this thesis) in combination with a ten Tesla magnet (which is about twenty times higher than the magnetic field strengths encountered in this thesis). Using the sulfuric acid solution in combination with a ten Tesla magnet in the setup presented in chapter 6, leads to Stuart numbers based on the magnetic force, $\mathrm{N}_{MHD} = \frac{\sigma B^2 T}{\rho u}$, of $0.1 < \mathrm{N}_{MHD} < 1$. This is in the same range as the Stuart numbers based on the electrical force, $\mathrm{N}_{EMHD} = \frac{\sigma E B T}{\rho u^2}$, presented in chapter 6. We can also estimate the Stuart numbers encountered in the actual steel casting process. Based on an electrical conductivity of $\sigma \approx 10^5$ S/m, a magnetic field strength of B = 0.3 T, a mould thickness of T = 0.07 m, a steel density of $\rho = 7{\times}10^3$ and an inlet velocity of $u_{in} \approx 1$ m/s, the Stuart number is N_{cast} = 0.09. Based on this comparison, a significant influence of the magnetic force on the flow can be expected when a ten Tesla magnet in combination with a sufuric acid is used, and hence this would be a suitable way to investigate MHD effects using transparent liquids. A footnote here is that safety issues regarding the sulfuric acid and also regarding the high magnetic field strengths should be taken into account.

Flows in liquid metals for actual MHD

The next step in investigating MHD effects is by performing experiments in actual liquid metal flows. Liquid metal flows in continuous casting configurations are being performed at some research centra in the world (e.g. Helmholtz Zentrum Dresden-Rossendorf, see Timmel et al. (2010)). For the working fluids, some options are available, which all have their advantages and disadvantages.

Working fluids

The first and most well known liquid metal is mercury, which is liquid at room temperature. The advantage of using mercury is that it is widely available and relatively cheap (around 15 Euros per kilogram). However, fumes from mercury are highly toxic so strict safety measures need to be taken into account, and in some laboratories it is even strictly prohibited.

A second possibility is the use of Gallium Indium Tin (Galinstan) alloys.

Galinstan is available in varying compositions, and has a melting point of -19°C. Compared to mercury, galinstan has a reduced toxicity and it has a low reactivity. The disadvantage of galinstan is that it is expensive, roughly 3000 €/kg, so for an experiment with the same size as reported in this thesis, with roughly 30 liters of liquid flowing, that would amount to roughly 700.000 Euros.

The third possible working fluid is a bismuth tin (BiSn) alloy, which has a melting point around 170°C. Experiments using BiSn are presented by Timmel et al. (2010) and promising results have been shown. The price of the bismuth tin alloy is around 25 €/kg, so this means an investment of less than 10.000 Euros for the working fluid when an experiment is performed with the size of the experiments reported in this thesis. However, a large investment needs to be done for equipment to melt the metal and keep the metal at a constant temperature of about 200°C.

Measurement techniques

Measurements in liquid metals provide a new set of challenges that are to be dealt with. One of the main disadvantages of using liquid metals, as compared to water, is that the liquid metals are opaque, so optical measurement techniques cannot be employed. Measurement techniques of the velocity in these configurations are existent, but still immature, especially when second order turbulence statistics are required.

The most common technique for the measurements of velocity in liquid metals is ultrasonic Doppler velocimetry (UDV) (Takeda 1991). In the UDV technique, a pulse of collimated ultrasounds travels into the measurement volume. Echoes come back from particles suspended in the liquid metal, and the delay time of the echo provides the distance from the particle to the transducer. The corresponding Doppler shift provides its velocity.

With the UDV measurement technique, promising results have been obtained for flows mimicing the continuous casting process, also with the inclusion of magnets as magnetic obstacles in the flow (Timmel et al. 2011). The spatial resolution in galinstan (as reported by Timmel et al.) when using UDV is 5 to 10 mm, depending on the distance from the transducer. Also, one transducer, which emits the ultrasonic burst, can measure velocities along one line. For the measurement of the velocity in a plane, a series of transducers is needed. Nowadays, complete systems are available which can handle up to 10 transducers. The recording rate of the system is 5 Hz, which is sufficient for capturing transient flow behavior, like the low frequency self-sustained oscillations.

Bibliography

Adrian, R. J., Westerweel, J., 2011. Particle image velocimetry. Cambridge university press, UK.

Anagnostopoulos, J., Bergeles, G., 1999. Three-dimensional modeling of the flow and the interface surface in a continuous casting mold model. Metallurgical and Materials Transactions B 30 (6), 1095–1105.

Andreev, O., Kolesnikov, Y., Thess, A., 2013. Visualization of the Ludford column. Journal of Fluid Mechanics 721, 438–453.

Berger, T. W., Kim, J., Lee, C., Lim, J., 2000. Turbulent boundary layer control utilizing the Lorentz force. Physics of Fluids 12 (3), 631–649.

Bouchet, G., Climent, E., Maurel, A., 2002. Instability of a confined jet impinging on an water/air free surface. Europhysics Letters 59 (6), 827–833.

Chanson, H., 1996. Air bubble entrainment in free surface turbulent shear flows. Academic Press.

Chaudhary, R., Rietow, B. T., Thomas, B. G., 2009. Differences between physical water models and steel continuous casters: A theoretical evaluation. in Inclusions and Clean Steels, Materials Science and Technology Conference, AIST/TMS, Pittsburgh, PA, 1090–1101.

Cierpka, C., Weier, T., Gerbeth, G., 2008. Evolution of vortex structures in an electromagnetically excited separated flow. Experiments in Fluids 45 (5), 943–953.

Crawford, C. H., Karniadakis, G. E., 1997. Reynolds stress analysis of EMHD-controlled wall turbulence. part i. streamwise forcing. Physics of Fluids 9 (3), 788–806.

Crocker, J., Grier, D., 1996. Methods of digital video microscopy for colloidal studies. Journal of Colloid and Interface Science 179 (1), 298–310.

Dabiri, D., 2009. Digital particle image thermometry/velocimetry: a review. Experiments in Fluids 46 (2), 191–241.

Dauby, P. H., 2011. Real flows in continuous casting moulds. Iron and Steel Technology 8 (6), 152–160.

Davidson, P. A., 2001. An Introduction to Magnetohydrodynamics. Cambridge University press, UK.

Duran-Matute, M., Trieling, R. R., van Heijst, G. J. F., 2011. Scaling and asymmetry in an electromagnetically forced dipolar flow structure. Physical Review E 83, 016306.

Durst, F., Melling, A., Whitelaw, J. H., 1976. Principles and practice of laser-Doppler anemometry. Academic Press.

Farkas, B., Paál, G., Szabó, K. G., 2012. Descriptive analysis of a mode transition of the flow over an open cavity. Physics of Fluids 24 (2), 027102.

Figueroa, A., Demiaux, F., Cuevas, S., Ramos, E., 2009. Electromagnetically driven vortices in a dipolar magnetic field in a shallow layer. Journal of Fluid Mechanics 641, 245–261.

Garcia-Hernandez, S., Morales, R. D., Torres-Alonso, E., 2010. Effects of EMBr position, mould curvature and slide gate on fluid flow of steel in slab mould. Ironmaking & Steelmaking 37 (5), 360–368.

Gebert, B. M., Davidson, M. R., Rudman, M. J., 1998. Computed oscillations of a confined submerged liquid jet. Applied Mathematical Modelling 22 (11), 843–850.

Geers, L. F. G., Hanjalić, K., Tummers, M. J., 2006. Wall imprint of turbulent structures and heat transfer in multiple impinging jet arrays. Journal of Fluid Mechanics 546, 255–284.

Geers, L. F. G., Tummers, M. J., Hanjalić, K., 2005. Particle imaging velocimetry-based identification of coherent structures in normally impinging multiple jets. Physics of Fluids 17 (5), 055105–055105–13.

Gupta, D., Chakraborty, S., Lahiri, A. K., 1997. Asymmetry and oscillation of the fluid flow pattern in a continuous casting mould: A water model study. ISIJ International 37 (7), 654–658.

Gupta, D., Lahiri, A., 1996. Cold model study of the surface profile in a continuous slab casting mold: Effect of second phase. Metallurgical and Materials Transactions B 27 (4), 695–697.

Gupta, D., Lahiri, A. K., 1994. Water-modelling study of the surface disturbances in continuous slab caster. Metallurgical and Materials Transactions B 25 (2), 227–233.

Haiqi, Y., Baofeng, W., Huiqin, L., Jianchao, L., 2008. Influence of electromagnetic brake on flow field of liquid steel in the slab continuous casting mold. Journal of Materials Processing Technology 202 (1-3), 179–187.

Harada, H., Toh, T., Ishii, T., Kaneko, K., Takeuchi, E., 2001. Effect of magnetic field conditions on the electromagnetic braking efficiency. ISIJ International 41 (10), 1236–1244.

Heeger, C., Gordon, R. L., Tummers, M. J., Sattelmayer, T., Dreizler, A., 2010. Experimental analysis of flashback in lean premixed swirling flames: upstream flame propagation. Experiments in Fluids 49 (4), 853–863.

Henoch, C., Stace, J., 1995. Experimental investigation of a salt water turbulent boundary layer modified by an applied streamwise magnetohydrodynamic body force. Physics of Fluids 7 (6), 1371–1383.

Holmes, P., Lumley, J. L., Berkooz, G., 1996. Turbulence, coherent structures, dynamical systems and symmetry. Cambridge University press, UK.

Honeyands, T. A., Herbertson, J., 1995. Flow dynamics in thin slab casting moulds. Steel Research 66 (7), 287–293.

Hussain, A. K. M., Reynolds, W. C., 1970. Mechanics of an organized wave in turbulent shear flow. Journal of Fluid Mechanics 41, 241–258.

Incropera, F. P., DeWitt, D. P., 4th ed. 1996. Fundamentals of heat and mass transfer. John Wiley & Sons.

Jeon, Y. J., Sung, H. J., Lee, S., 2010. Flow oscillations and meniscus fluctuations in a funnel-type water mold model. Metallurgical and Materials Transactions B 41B, 121–130.

Kalter, R., Tummers, M. J., Kenjereš, S., Righolt, B. W., Kleijn, C. R., 2013. Oscillations of the fluid flow and the free surface in a cavity with a submerged bifurcated nozzle. International Journal of Heat and Fluid Flow 44, 365 – 374.

Kenjereš, S., 2008. Electromagnetic enhancement of turbulent heat transfer. Physical Review E 78 (6), 066309.

Kenjereš, S., 2011. Electromagnetically driven dwarf tornados in turbulent convection. Physics of Fluids 23 (1).

Kenjereš, S., Verdoold, J., Tummers, M. J., Hanjalić, K., Kleijn, C. R., 2009. Numerical and experimental study of electromagnetically driven vortical flows. International Journal of Heat and Fluid Flow 30 (3), 494–504.

Kiger, K. T., Duncan, J. H., 2012. Air-entrainment mechanisms in plunging jets and breaking waves. Annual Review of Fluid Mechanics 44, 563–596.

Kim, S. J., Lee, C. M., 2000. Investigation of the flow around a circular cylinder under the influence of an electromagnetic force. Experiments in Fluids 28 (3), 252–260.

Kolsek, T., Jelic, N., Duhovnik, J., 2007. Numerical study of flow asymmetry and self-sustained jet oscillations in geometrically symmetric cavities. Applied Mathematical Modeling 31 (10), 2355–2373.

Lamb, H., 1932. Hydrodynamics. 6th ed. Dover, New York.

Lawson, N. J., Davidson, M. R., 2001. Self-sustained oscillation of a submerged jet in a thin rectangular cavity. Journal of Fluids and Structures 15, 59–81.

Lawson, N. J., Davidson, M. R., 2002. Oscillatory flow in a physical model of a thin slab casting mould with a bifurcated submerged entry nozzle. Journal of Fluids Engineering 124 (2), 535–543.

Madarame, H. Okamoto, K., Iida, M., 2001. Self-induced sloshing caused by an upward round jet impinging on the free surface. Journal of Fluids and Structures 16, 417–433.

Mahmoudi, J., 2006. Mathematical modelling of fluid flow, heat transfer and solidification in a strip continuous casting process. International Journal of Cast Metals Research 19 (4), 223–236.

Mataoui, A., Schiestel, R., 2009. Unsteady phenomena of an oscillating turbulent jet flow inside a cavity: Effect of aspect ratio. Journal of Fluids and Structures 25 (1), 60–79.

Maurel, A., Ern, P., Zielinska, B. J. A., Wesfreid, J. E., 1996. Experimental study of self-sustained oscillations in a confined jet. Physical Review E 54, 3643–3651.

Miranda-Tello, J. R., Sanchez-Rangel, F., Real-Ramirez, C. A., Khatchatourov, G., Aragon-Lezama, J. A., Hoyos-Reyes, L. F., Andrade-Gonzalez, E. A., Gonzalez-Trejo, J. I., 2012. Characterization of the level fluctuations in a physical model of the steel continuous casting mold through image processing. Revista Mexicana de Fysica 58 (2), 166–173.

Mizoguchi, S., Ohashi, T., Saeki, T., 1981. Continuous casting of steel. Annual Review of Materials Science 11 (1), 151–169.

Molloy, N. A., 1970. Impinging jet flow in a two-phase system: The basic flow pattern. Journal of the Iron and Steel Institute 208, 943–950.

Molloy, N. A., Taylor, P. L., 1969. Oscillatory motion of a jet into a blind cavity. Nature 224, 1192–1194.

Najjar, F. M., Thomas, B. G., Hershey, D. E., 1995. Numerical study of steady turbulent-flow through bifurcated nozzles in continuous casting. Metallurgical and Materials Transactions B 26 (4), 749–765.

Nakato, H., Ozawa, M., Kinoshita, K., Habu, Y., Emi, T., 1984. Factors affecting the formation of shell and longitudinal cracks in mold during high-speed continuous-casting of slabs. Transactions of the Iron and Steel Institute of Japan 24 (11), 957–965.

Podvin, B., Sergent, A., 2012. Proper orthogonal decomposition investigation of turbulent Rayleigh-Bénard convection in a rectangular cavity. Physics of Fluids 24 (10), 105106–105106–26.

Pope, S. B., 2000. Turbulent flows. Cambridge University Press.

Real-Ramirez, C. A., Gonzalez-Trejo, J. I., 2011. Analysis of three-dimensional vortexes below the free surface in a continuous casting mold. International Journal of Minerals and Metallurgy and Materials 18 (4), 397–406.

Rockwell, D., 1983. Oscillations of impinging shear layers. AIAA Journal 21 (5), 645–664.

Rockwell, D., Naudascher, E., 1978. Review - self-sustaining oscillations of flow past cavities. ASME Transactions Journal of Fluids Engineering 100, 152–165.

Rockwell, D., Naudascher, E., 1979. Self-sustained oscillations of impinging free shear layers. Annual Review of Fluid Mechanics 11, 67–94.

Rossi, L., Bocquet, S., Ferrari, S., de la Cruz, J. M. G., Lardeau, S., 2009. Control of flow geometry using electromagnetic body forcing. International Journal of Heat and Fluid Flow 30 (3), 505–513.

Rossi, L., Doorly, D., Kustrin, D., 2012a. Lamination and mixing in laminar flows driven by Lorentz body forces. Europhysics Letters 97 (1), 14006.

Rossi, L., Doorly, D., Kustrin, D., 2012b. Lamination and mixing in three fundamental flow sequences driven by electromagnetic body forces. Physical Review E 86 (2), 026313.

Rowley, C. W., Colonius, T., Basu, A. J., 2002. On self-sustained oscillations in two-dimensional compressible flow over rectangular cavities. Journal of Fluid Mechanics 455, 315 – 346.

Rowley, C. W., Williams, D. R., 2006. Dynamics and control of high-reynolds-number flow over open cavities. Annual Review of Fluid Mechanics 38, 251–276.

Saeki, S., Madarame, H., Okamoto, K., 2001. Self-induced sloshing excited by a horizontally injected plane jet. Journal of Fluid Mechanics 448, 81–114.

Semeraro, O., Bellani, G., Lundell, F., 2012. Analysis of time-resolved PIV measurements of a confined turbulent jet using POD and Koopman modes. Experiments in Fluids 53 (5), 1203–1220.

Seyedein, S., Hasan, M., 1997. A three-dimensional simulation of coupled turbulent flow and macroscopic solidification heat transfer for continuous slab casters. International Journal of Heat and Mass Transfer 40 (18), 4405–4423.

Sirovich, L., 1987. Turbulence and the dynamics of coherent structures. I - coherent structures. Quarterly of Applied Mathematics 45 (3), 561–571.

Spong, E., Reizes, J., Leonardi, E., 2005. Efficiency improvements of electromagnetic flow control. International Journal of Heat and Fluid Flow 26 (4), 635–655.

Stasiek, J., Stasiek, A., Jewartowski, M., Collins, M., 2006. Liquid crystal thermography and true-colour digital image processing. Optics and Laser Technology 38 (4-6), 243–256.

Stefani, F., Gundrum, T., Gerbeth, G., 2004. Contactless inductive flow tomography. Physical Review E 70 (5), 056306.

Szekely, J., Yadoya, R. T., 1972. The physical and mathematical modelling of the flow field in the mold region in continuous casting systems: Part i. model studies with aqueous systems. Metallurgical Transactions 3 (10), 2673–2680.

Takeda, Y., 1991. Development of an ultrasound velocity profile monitor. Nuclear Engineering and Design 126 (2), 277–284.

Tam, C. K. W., Block, P. J. W., 1978. On the tones and pressure oscillations induced by flow over rectangular cavities. Journal of Fluid Mechanics 89 (02), 373–399.

Timmel, K., Eckert, S., Gerbeth, G., 2011. Experimental investigation of the flow in a continuous-casting mold under the influence of a transverse, direct current magnetic field. Metallurgical and Materials Transactions B 42 (1), 68–80.

Timmel, K., Eckert, S., Gerbeth, G., Stefani, F., Wondrak, T., 2010. Experimental modeling of the continuous casting process of steel using low melting point metal alloys - the LIMMCAST program. ISIJ International 50 (8), 1134–1141.

Torres-Alonso, E., Morales, R., García-Hernández, S., 2010a. Cyclic turbulent instabilities in a thin slab mold. part II: mathematical model. Metallurgical and Materials Transactions B 41 (3), 675–690.

Torres-Alonso, E., Morales, R., García-Hernández, S., Palafox-Ramos, J., 2010b. Cyclic turbulent instabilities in a thin slab mold. part I: physical model. Metallurgical and Materials Transactions B 41 (3), 583–597.

Torres-Alonso, E., Morales, R. D., Demedices, G. L., 2007. Flow dynamics in thin slab molds driven by sustainable oscillating jets from the feeding SEN. ISIJ International 47 (5).

Uzol, O., Camci, C., 2002. Experimental and computational visualization and frequency measurements of the jet oscillation inside a fluidic oscillator. Journal of Visualization 5 (3), 263–272.

Verdoold, J., Tummers, M. J., Hanjalic, K., 2009. Prime modes of fluid circulation in large-aspect-ratio turbulent Rayleigh-Bénard convection. Physical Review E 80 (3), 037301.

Villermaux, E., Hopfinger, E. J., 1994. Self-sustained oscillations of a confined jet: a case study for the non-linear delayed saturation model. Physica D: Nonlinear Phenomena 72 (3), 230–243.

Wang, X., Tang, L., Zang, X., Yao, M., 2012. Mold transient heat transfer behavior based on measurement and inverse analysis of slab continuous casting. Journal of Materials Processing Technology 212 (9), 1811 – 1818.

Wee, D., Yi, T., Annaswamy, A., Ghoniem, A. F., 2004. Self-sustained oscillations and vortex shedding in backward-facing step flows: Simulation and linear instability analysis. Physics of Fluids 16 (9), 3361–3373.

Weier, T., Cierpka, C., Gerbeth, G., 2008. Coherent structure eduction from PIV data of an electromagnetically forced separated flow. Journal of Fluids and Structures 24 (8), 1339 –1348.

Weier, T., Gerbeth, G., Mutschke, G., Lielausis, O., Lammers, G., 2003. Control of flow separation using electromagnetic forces. Flow, Turbulence and Combustion 71 (1), 5–17.

Wolf, A. V., Brown, M. G., Prentiss, P. G., 1986. CRC Handbook of Chemistry and Physics. CRC press, Inc. USA.

Yokoyama, H., Tsukamoto, Y., Kato, C., Iida, A., 2007. Self-sustained oscillations with acoustic feedback in flows over a backward-facing step with a small upstream step. Physics of Fluids 19 (10), 106104.

Yuan, Q., Thomas, B., Vanka, S. P., 2004. Study of transient flow and particle transport in continuous steel caster molds: Part i. fluid flow. Metallurgical and Materials Transactions B 35 (4), 685–702.

Zhang, H., Fan, B., Chen, Z., 2010. Computations of optimal cylinder flow control in weakly conductive fluids. Computers & Fluids 39 (8), 1261–1266.

Zhang, L., Yang, S., Cai, K., Li, J., Wan, X., Thomas, B. G., 2007. Investigation of fluid flow and steel cleanliness in the continuous casting strand. Metallurgical and Materials Transactions B 38 (1), 63–83.

Zhao, B., Thomas, B. G., Vanka, S. P., O'Malley, R., 2005. Transient fluid flow and superheat transport in continuous casting of steel slabs. Metallurgical and Materials Transactions B 36 (6), 801–823.

List of publications

R. Kalter, M.J. Tummers, S. Kenjereš, B.W. Righolt and C.R. Kleijn (2013). *Oscillations of the fluid flow and the free surface in a cavity with a submerged bifurcated nozzle.* International Journal of Heat and Fluid Flow. 44, 365 - 374

R. Kalter, M.J. Tummers, S. Kenjereš, B.W. Righolt and C.R. Kleijn (2014). *Electromagnetic flow control in a rectangular cavity with a bifurcated nozzle.* International Journal of Heat and Fluid Flow. 47, 113-122

R. Kalter, M.J. Tummers, S. Kenjereš, B.W. Righolt and C.R. Kleijn (2014). *Effects of electromagnetic forcing on self-sustained jet oscillations.* Physics of Fluids. 26, 065101

R. Kalter, M.J. Tummers, J.B. Wefers Bettink, S. Kenjereš, B.W. Righolt and C.R. Kleijn (2014).*Aspect ratio effects on fluid flow fluctuations in rectangular cavities.* Metallurgical and Materials Transactions B. 45 (6), 2186-2193

R. Kalter, M.J. Tummers, S. Kenjereš, B.W. Righolt and C.R. Kleijn (2014). *Experimental modeling of heat transfer in a continuous casting mould model.* Proceedings of the ASME 2014 4th Joint US-European Fluids Engineering Summer Meeting

Acknowledgements

Een promotiewerk doe je nooit alleen, daarom wil ik hier graag de ruimte nemen om een aantal mensen te bedanken die in meer en mindere mate hebben meegeholpen om uiteindelijk dit proefschrift tot stand te laten komen.

Allereerst wil ik mijn promotor, Chris Kleijn bedanken. We hebben in de afgelopen 4 jaar talloze progress meetings gehouden, waarbij je altijd opbouwend kritisch keek naar de vorderingen. Jouw input in dit proces heeft mij altijd geïnspireerd om net dat stapje extra te zetten. Dank daarvoor! Dan wil ik graag Mark Tummers bedanken. Mark, jouw kritische houding ten opzichte van alles wat ik je liet zien in het lab of wat ik je liet lezen heeft zeer bijgedragen aan de kwaliteit van mijn werk! In dit project heb ik ook nauw samengewerkt met Bernhard Righolt, die het numerieke gedeelte van het project op zich heeft genomen. Door deze samenwerking hebben we veel kunnen brainstormen over de te nemen stappen in dit project. Ook onze tripjes naar IJmuiden, Dresden en Västerås heb ik als zeer prettig ervaren. Dank voor deze samenwerking. Ook Saša Kenjereš heeft een grote bijdrage geleverd in dit werk. Saša, jouw aanstekelijke enthousiasme haalt het beste naar voren in elke jonge wetenschapper.

In het lab was er niks gelukt als ik niet kon bouwen op de ervaring en inzicht van Bart. Bart, jij hebt enorm veel geholpen in het ontwerp en de constructie van de verschillende opstellingen, jouw inzicht in het voorkomen van allerlei mogelijke rampscenario's heeft enorm geholpen in de voortgang van dit project. Verder ben ik veel dank verschuldigd aan 'de technici' Erwin, Jaap, Evert, Lodi, Jaap, Jan. Hartelijk dank voor jullie hulp bij het installeren/uitlijnen van lasers, ontwerpen van experimentele opstellingen, gebruiken van camera's, en vervaardigen van allerlei experimentele benodigdheden. Ook een hartelijk dank aan Anita, Fiona, Amanda en Angela voor alle hulp en ondersteuning in de dagelijkse gang van zaken.

Dit project was een STW project met een zeer actieve gebruikerscommissie die zo eens in het half jaar bij elkaar kwam. Dirk, Eelco, Alja, dank voor jullie

enthousiasme en feedback op de geleverde resultaten. Jan-Erik, thank you for taking the time and effort to fly to Holland every time we had this user committee meeting.

Tijdens dit project heb ik een aantal studenten begeleid gedurende hun BSc of MSc project. Voor mij was dit een geweldige leerervaring. Lars, Duco, Jeroen, ik hoop dat jullie onze samenwerking net zo positief hebben ervaren als ik. Beata, even though you were not officially 'my' student, I enjoyed our collaboration in the lab a lot. I still hope we can find some explanation for the 'ghost bubble'.

Furthermore I would like to thank my room mates in the several offices at the Lorentzweg, Leeghwaterstraat and in de Waterzaal, and my lab mates at the Lorentzweg: Michael, Niels, Rajat, Cees, Ali, Luis, Milos, Maikel, Martin. Thanks for a good time and the numerous discussions about our work. Furthermore I would like to thank my fellow PhD students at TP: Laurens, Dries, Michiel, Koen, Anton, Duong, Wenjie, Xiaogang, Hrushikesh, Annekatrien. Ik wil ook graag de MSc en BSc studenten bij TP bedanken voor goede tijden bij koffiepauzes, labuitjes en op het laatst zelfs wieleruitjes. Met de kans dat ik mensen vergeet wil ik toch een paar namen noemen: Alexander, Rick, Rosanne, Sinta, Yoerik, Heleen, Romboud, Wout, Gerrit, Jasper, Matthijs, Mathijs, Jimmy, Corné, Simon, Ruben, Niels, Tjeerd. Bedankt!

Last but not least wil ik graag mijn familie en vrienden bedanken voor hun niet aflatende vertrouwen en steun in de afgelopen jaren. Veel nodige ontspanning heb ik ondervonden tijdens avondjes met vrienden aan de bar, bij koffierondjes, op vakanties en tijdens verscheidene hardloopevenementen.

Pap, mam, Joke, Irma en Nick, bedankt voor jullie steun en luisterend oor ten alle tijde. Aafke, je hebt het laatste deel van mijn project meegemaakt, waarin ik de teugels al wat heb kunnen laten vieren. Ik ben blij dat ik deze tijd met jou heb kunnen delen en kijk uit naar de tijd die voor ons ligt.

About the author

Rudi Kalter, born December 2 1984, Kampen

1997-2003	Almere College Kampen.
2003-2010	Student applied physics, Delft University of Technology MSc. project at the Multiscale physics department with title “Visual investigation of the gas/liquid interface in horizontal pipe flows”.
2010-2014	PhD student, section Transport Phenomena, department of Chemical Engineering, faculty of Applied Sciences Delft University of Technology.